



12-2005

## Comparison of Microscopic Modalities for the 3D Model Reconstruction of Nanodevices

Christopher Robert Kammerud  
*University of Tennessee, Knoxville*

Follow this and additional works at: [https://trace.tennessee.edu/utk\\_gradthes](https://trace.tennessee.edu/utk_gradthes)



Part of the [Electrical and Computer Engineering Commons](#)

---

### Recommended Citation

Kammerud, Christopher Robert, "Comparison of Microscopic Modalities for the 3D Model Reconstruction of Nanodevices. " Master's Thesis, University of Tennessee, 2005.  
[https://trace.tennessee.edu/utk\\_gradthes/4545](https://trace.tennessee.edu/utk_gradthes/4545)

This Thesis is brought to you for free and open access by the Graduate School at TRACE: Tennessee Research and Creative Exchange. It has been accepted for inclusion in Masters Theses by an authorized administrator of TRACE: Tennessee Research and Creative Exchange. For more information, please contact [trace@utk.edu](mailto:trace@utk.edu).

To the Graduate Council:

I am submitting herewith a thesis written by Christopher Robert Kammerud entitled "Comparison of Microscopic Modalities for the 3D Model Reconstruction of Nanodevices." I have examined the final electronic copy of this thesis for form and content and recommend that it be accepted in partial fulfillment of the requirements for the degree of Master of Science, with a major in Electrical Engineering.

Mongi A. Abidi, Major Professor

We have read this thesis and recommend its acceptance:

Besma Abidi, Sean Kong

Accepted for the Council:

Carolyn R. Hodges

Vice Provost and Dean of the Graduate School

(Original signatures are on file with official student records.)

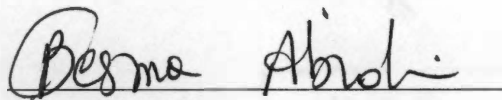
To the Graduate Council:

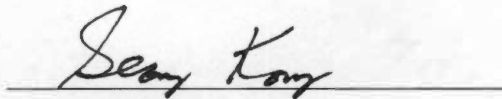
I am submitting herewith a thesis written by Christopher Robert Kammerud entitled "Comparison of Microscopic Modalities for the 3D Model Reconstruction of Nanodevices." I have examined the final paper copy of this thesis for form and content and recommend that it be accepted in partial fulfillment of the requirements for the degree of Master of Science, with a major in Electrical Engineering.



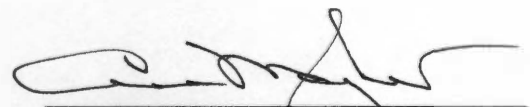
Dr. Mongi A. Abidi, Major Professor

We have read this thesis  
and recommend its acceptance:





Accepted for the Council:



Vice Chancellor and  
Dean of Graduate Studies

Thesis  
2005  
.k26

10/11 - A.M.

LIBRARY OF THE  
UNIVERSITY OF TEXAS AT AUSTIN  
RICHARDSON

2005

*[Faint signature]*

# **Comparison of Microscopic Modalities for the 3D Model Reconstruction of Nanodevices**

**A Thesis**

**Presented for**

**Master of Science**

**Degree**

**The University of Tennessee, Knoxville**

**Christopher Robert Kammerud**

**December 2005**

# Acknowledgements

Wherever we take the time and energy to look, new worlds are waiting for us. My time as a Master's student has opened up places, in my heart and mind, which had previously gone unexplored. Dr. Mongi Abidi brought me to the IRIS lab. He gave me funding and a place from which to start exploring, and for that I'll always be grateful. I have to thank Dr. Besma Abidi for her work as my advisor, giving me points to aim at, and helping make sure that I reached them. With her help and guidance, I discovered what it was like to have my research published. I would also like to thank Greg Jones and John Dunlap, who were in charge of the microscopes I used in my research. They introduced me to a world beyond sight, and gave me the knowledge and tools to walk there.

Of the many new friends I've met at IRIS, there are too many to thank. I've never been in a place with so many people from so many different places, and it was a lucky, amazing thing that I could share my time with them. Thanks in particular to Hari, who was there whenever I needed him, and without hesitation, gave me a home when I had lost mine.

Finally, and most importantly I have to thank my family. To my sister I say thanks for the countless conversations we've had about everything ever, and for agreeing with me, that it really is true, if you want something bad enough, and are willing to work hard enough, you usually can get it. To my mom and dad, there aren't words really to say thanks enough. They have always shown me love and support for whatever practical or foolish hopes I've pursued. They have always stood behind me as the home I can return to when I need to reset my bearings. It is a blessing to know I have such a place, as I graduate and go in search of the strange, new worlds that are still waiting for me.

# Abstract

As manufacturing capabilities push nanotechnology to smaller and smaller scales, novel inspection schemes must be developed to ensure product quality. The objective of our research was to implement, refine, and compare 3D reconstruction algorithms that could aid manufacturers in their ability to visualize and inspect nanodevices. Data was collected from three different microscopes: the atomic force microscope (AFM), the scanning electron microscope (SEM), and the laser scanning confocal microscope (LSCM). For each of these microscopes, a specific algorithm was implemented to generate 3D models from the raw microscope data. Scans from the AFM microscope give range information similar to laser range finders, and the conversion to 3D information was also done in a similar manner. For the SEM inspection, stereo methods were used to build dense elevation maps of the specimen. The LSCM focuses on a very thin section of the specimen so that it can optically slice the specimen into a stack of images along the z-axis. From these stacks, multifocus methods can be used to generate a 3D model.

These algorithms were implemented and 3D models generated for micro-electro-mechanical systems (MEMS), donated by MEMSCAP©, as well as calibration gratings that provide step heights of 18 nm, 100 nm, and 500 nm. Contributions are made in the refinement and comparison of each microscope's results and capabilities, as well as a novel registration method to stitch together 3D models of neighboring regions.

# Contents

<b>1</b>	<b>Introduction .....</b>	<b>1</b>
1.1	Motivation.....	1
1.2	Background.....	2
1.3	Contributions.....	3
<b>2</b>	<b>Literature Review.....</b>	<b>8</b>
2.1	Probe-Based Reconstruction.....	8
2.1.1	Atomic Force Microscope Imaging Model.....	9
2.1.2	Image and Tip Reconstruction.....	9
2.2	Tomography.....	11
2.2.1	Tomography in Electron Microscopes.....	12
2.2.2	X-Ray Nanotomography.....	14
2.3	Interferometry and Diffraction Patterns.....	17
2.4	Stereo Imaging.....	22
2.5	Depth from Focus .....	25
<b>3</b>	<b>Data Acquisition.....</b>	<b>29</b>
3.1	Information On Our Samples.....	29
3.2	The Atomic Force Microscope .....	29
3.3	The Laser Scanning Confocal Microscope .....	36
3.4	The Scanning Electron Microscope.....	39
<b>4</b>	<b>3D Reconstruction.....</b>	<b>43</b>
4.1	Atomic Force Microscope.....	43
4.2	Laser Scanning Confocal Microscope .....	45
4.3	Scanning Electron Microscope .....	49
4.3.1	Rectification.....	52
4.3.2	Sparse Matching.....	54
4.3.3	Dense Elevation Map Generation .....	56
<b>5</b>	<b>Model Registration.....</b>	<b>71</b>
5.1	Orientation Correlation .....	71
5.2	Registration of 3D Range Data .....	72
<b>6</b>	<b>Comparison of Results.....</b>	<b>77</b>
6.1	Ground Truth .....	77
6.1.1	Atomic Force Microscope.....	77
6.1.2	Laser Scanning Confocal Microscope .....	79
6.1.3	Scanning Electron Microscope .....	79
6.2	MEMS Reconstructions .....	82
<b>7</b>	<b>Conclusions.....</b>	<b>87</b>



**LIST OF REFERENCES .....90**  
**VITA .....98**

# List of Figures

<b>Figure 1.1:</b> Process of 3D reconstruction for the AFM.....	4
<b>Figure 1.2:</b> Process of 3D reconstruction for the LSCM .....	5
<b>Figure 1.3:</b> Process of 3D reconstruction for the SEM.....	7
<b>Figure 2.1:</b> Model for AFM imaging. ....	9
<b>Figure 2.2:</b> Downward noise magnified.....	10
<b>Figure 2.3:</b> Illustration of the nature of projections. ....	12
<b>Figure 2.4:</b> Dark field corrected projections. ....	15
<b>Figure 2.5:</b> Reconstructed slices taken from the second layer of tungsten plug vias on a processor .....	16
<b>Figure 2.6:</b> Comparison of SEM image and x-ray acquired image .....	16
<b>Figure 2.7:</b> 3D reconstruction from x-ray microscopy .....	17
<b>Figure 2.8:</b> Basic interferometer setup .....	18
<b>Figure 2.9:</b> Novel conception of phase-shift interferometry.....	19
<b>Figure 2.10:</b> Scanning white-light interferometry setup .....	20
<b>Figure 2.11:</b> Interferometer profile .....	21
<b>Figure 2.12:</b> Geometry of SEM microscope. ....	23
<b>Figure 2.13:</b> Illustration of shearing techniques to aid in alignment of SEM stereo images .....	24
<b>Figure 2.14:</b> Illustration of confocal optical slicing.....	26
<b>Figure 2.15:</b> Plot of variance data (blue) versus image stack location fitted with a curve (red).....	28
<b>Figure 3.1:</b> Design layout of MEMS devices scanned in our research.....	30
<b>Figure 3.2:</b> Optical microscope image of MEMS devices. ....	30
<b>Figure 3.3:</b> SEM images of calibration gratings. ....	31
<b>Figure 3.4:</b> Image of Asylum Molecular Force Probe 3D AFM.....	32
<b>Figure 3.5:</b> Results of AFM scan. ....	33
<b>Figure 3.6:</b> Results of median filtering AFM scan in Figure 3.5. ....	34
<b>Figure 3.7:</b> Series of AFM 3D models demonstrating the effect of resolution .....	35
<b>Figure 3.8:</b> Leica TCS SP2 LSCM.....	36
<b>Figure 3.9:</b> Selected images from a stack of 92 optical slices taken by the confocal microscope. ....	37
<b>Figure 3.10:</b> Maximum intensity values for a single pixel, constructed from confocal optical slices of a harmonic motor. ....	37
<b>Figure 3.11:</b> Maximum intensity image of a wobble motor, constructed from confocal optical slices .....	38
<b>Figure 3.12:</b> Image of Leo 1525 SEM microscope .....	39

<b>Figure 3.13:</b> SEM image of MEMS chip with charging effects in bright white.....	40
<b>Figure 3.14:</b> SEM image of MEMS chip without charging effects .....	40
<b>Figure 3.15:</b> SEM images taken at different tilt angles showing different illumination effects, low contrast, and salt-and-pepper noise. ....	41
<b>Figure 3.16:</b> Median filtered and contrast stretched SEM images at different tilt angles, still showing different illumination effects. ....	41
<b>Figure 3.17:</b> Stereo pair from SEM with noise filtered, contrast stretched, and illumination adjusted to be approximately uniform between the pair. ....	42
<b>Figure 4.1:</b> AFM range data converted to VRML file and visualized in Rapidform®....	44
<b>Figure 4.2:</b> AFM range data converted to VRML file with faces applied and visualized in Rapidform®.. ....	44
<b>Figure 4.3:</b> AFM range data converted to VRML file and visualized in Rapidform®. ....	45
<b>Figure 4.4:</b> De-noised AFM data. ....	46
<b>Figure 4.5:</b> AFM range data converted to VRML file and visualized in Rapidform®. ....	46
<b>Figure 4.6:</b> Confocal range image created where each pixel's height is based on the stack location where that pixel's intensity was highest. ....	47
<b>Figure 4.7:</b> 3D model created by converting the confocal range image to VRML and visualizing in RapidForm®.....	48
<b>Figure 4.8:</b> Plot of parabola fitting to raw intensity vs. stack location data.....	49
<b>Figure 4.9:</b> 3D model created curve-fitting method of determining the height. Measurements are in microns. ....	50
<b>Figure 4.10:</b> Representation of SEM coordinate space adapted from (Piazzesi, 1972)...	51
<b>Figure 4.11:</b> Corner detection result on SEM image .....	53
<b>Figure 4.12:</b> SEM stereo images with horizontal lines drawn over to illustrate epipolar alignment.....	55
<b>Figure 4.13:</b> Enlarged strips from Figure 4.12a and 4.12b .....	55
<b>Figure 4.14:</b> Rectified stereo images and corresponding edge images .....	57
<b>Figure 4.15:</b> Sparsely matched points from SEM stereo .....	58
<b>Figure 4.16:</b> 3D point cloud model from matched points shown in Figure 4.15 .....	59
<b>Figure 4.17:</b> Grid lines layed over left, (a) and right, (b) stereo images.....	59
<b>Figure 4.18:</b> Illustration of the grid matching algorithm .....	60
<b>Figure 4.19:</b> Energy minimization result .....	61
<b>Figure 4.20:</b> Interpolating between grid points.....	61
<b>Figure 4.21:</b> 3D models from SEM stereo using energy minimization matching without grid refinement.....	62
<b>Figure 4.22:</b> Matching on two stereo images with sparse grid .....	63
<b>Figure 4.23:</b> Illustration of grid refinement .....	64
<b>Figure 4.24:</b> Process of grid refinement and the resulting disparity map are shown.....	65
<b>Figure 4.25:</b> 3D model with SEM stereo using energy minimization matching methods. ....	66
<b>Figure 4.26:</b> Searching for matching points between two images. ....	66
<b>Figure 4.27:</b> Rectified stereo images and corresponding edge images .....	68
<b>Figure 4.28:</b> Generation of dense elevation map from SEM stereo .....	69
<b>Figure 4.29:</b> Rapidform® visualization of disparity image in Figure 4.27(e). ....	70

<b>Figure 5.1: AFM registration of range images.....</b>	<b>73</b>
<b>Figure 5.2: 3D model of registered images.....</b>	<b>73</b>
<b>Figure 5.3: Mosaic of 8 confocal stacks .....</b>	<b>74</b>
<b>Figure 5.4: 3D model generated from range image shown in Figure 5.3(i). .....</b>	<b>75</b>
<b>Figure 5.5: Stereo pairs from overlapping areas. ....</b>	<b>75</b>
<b>Figure 5.6: Registration results for stereo pairs shown in Figure 5.5 .....</b>	<b>76</b>
<b>Figure 6.1: Collected AFM data for TGZ3 .....</b>	<b>78</b>
<b>Figure 6.2: Graph showing original untilted AFM height profile for TGZ3 compared with tilted profile.....</b>	<b>78</b>
<b>Figure 6.3: Collected AFM data for TGZ02.....</b>	<b>79</b>
<b>Figure 6.4: Graph showing original untilted AFM height profile for TGZ02 compared with tilted profile.....</b>	<b>80</b>
<b>Figure 6.5: Collected AFM data for TGZ01 .....</b>	<b>80</b>
<b>Figure 6.6: Graph showing original untilted AFM height profile for TGZ01 compared with tilted profile.....</b>	<b>80</b>
<b>Figure 6.7: Collected LCSM data for TGZ03 at 10x.....</b>	<b>81</b>
<b>Figure 6.8: Comparison of AFM and LCSM height profiles for TGZ03 .....</b>	<b>81</b>
<b>Figure 6.9: SEM stereo images of TGZ02 at 20,000x.....</b>	<b>82</b>
<b>Figure 6.10: Matching and disparity map created for TGZ02. ....</b>	<b>83</b>
<b>Figure 6.11: Heights recorded in SEM 3D reconstruction of TGZ02 along sample profile lines.....</b>	<b>84</b>
<b>Figure 6.12: Comparison of LCSM and SEM reconstruction of harmonic motor area... </b>	<b>85</b>
<b>Figure 6.13: Comparison of LCSM and SEM reconstruction of wire contact point .....</b>	<b>86</b>
<b>Figure 7.1: Chart of possible sensor fusion combinations using the LCSEM at ORNL. ...</b>	<b>89</b>

# 1 Introduction

In our work we use three different microscopy technologies: atomic force microscope (AFM), scanning electron microscope (SEM), and a laser scanning confocal microscope (LSCM) to generate 3D models of nanodevices. The individual microscopes each has individual advantages and disadvantages, and each requires a different method for extracting 3D information from the scans conducted. This thesis focuses on implementing and refining algorithms to reconstruct 3D models of micro-electro-mechanical systems, assessing the results achievable from each.

## 1.1 Motivation

Nanotechnology brings benefits to several areas of science including: medicine, where substances such as nano hydroxyapatite (HA) are used in bone repair and regeneration, materials, where stain-resistant pants and shirts are a commercial success, and in microelectronic devices, or MEMS. Imaging successfully at the nano-scale is key to the advancement of nanotechnology as a whole. The ability to produce high quality images and 3D reconstructions of objects leads to better defect detection and also understanding of the quantum effects that occur between such small distances. The accurate measurement of surface features serves as important criteria of product quality. The advancement of MEMS as a commercial product is often compared to the similar development of the VLSI market. In order for MEMS devices to be widely used and trusted, as VLSI devices are, MEMS metrology has to advance to an acceptable level of accuracy and robustness.

Our research is focused on gauging the effectiveness of three possible methods of 3D reconstruction and inspection. The AFM, SEM, and LSCM, all allow a user to generate 3D information of MEMS devices. Our work has been to implement, refine, and assess the method of reconstruction and accuracy of each microscope. As well, we wanted to compare the microscopes against each other, determining strengths and weaknesses.

## 1.2 Background

3D reconstruction at the nanoscale requires specialized devices, and considerations not seen when acquiring 3D data at larger scales. The AFM, LSCM, and SEM are such specialized devices that were developed to let scientists see into a new and smaller world. Each of these systems, though, has certain physical properties that can influence the way data is collected. At such small scales, an AFM image will show artifacts if the features being examined are smaller than the tip itself. LSCM microscopes use lasers for imaging, and their wavelengths only allow accurate measurements down to the hundreds of nanometers. SEM images are created using a concentrated beam of electrons, and on certain specimens, charging effects caused by a build up of electrons can appear as white blooming areas. These data collection issues must be considered when acquiring images at such small scales. Once the data is collected, however, 3D reconstruction using standard computer vision methods can proceed with little to no alterations.

Our project's main goal was to examine nanodevices with the AFM, LSCM, and SEM, implementing, refining, and assessing the 3D reconstruction capability and accuracy of each microscope in conjunction with its accompanying algorithm. In our search of the literature several reviews were found of different imaging technologies and algorithms used to characterize these nanodevices or materials. Villarubia (1997) covered several different algorithms for the enhancement of AFM images (Villarubia, 1997). El Rifai et al (2003) briefly covered the technology of several of the main instruments used in nano-imaging (El Rifai, Aumond, & Youcef-Toumi 2003). Bonnet (2004) gave a very broad and accurate look at current trends in imaging methods, while not attempting to review the state of the art in any certain area (Bonnet, 2004).

Several papers have been written comparing the results of different microscope systems. Raspanti et al., (2005) compared stereo SEM reconstruction to AFM reconstruction, by registering an AFM dataset and stereo micrograph and calculating the cross-correlation coefficient between them (Raspanti et al., 2005). Composite LSCM and SEM images were created by Lopez-Cepero et al. (2005). The height map from the LSCM was registered with an SEM image of the same area (Lopez-Cepero et al., 2005). Fewer papers have been published on combining different modalities into a single reconstruction. Velazquez-Muriel et al. (2001) used AFM surface measurements as a priori information to bound the tomographic reconstruction from a TEM (Velazquez-Muriel et al., 2001).

Seeger (2004) fused 3D information from AFM and SEM images to reconstruct a 3D model with the height accuracy of an AFM scan, but without the broadening of features often seen in an AFM scan (Seeger, 2004). The AFM image was created using a dull tip, and the SEM 3D information was obtained using a novel simulation procedure, similar to shape from shading, but with more sophisticated reflectance models than traditional models. The surface shape description produced cannot be used for measuring absolute height differences between points on the surface, as opposed to stereo methods such as the ones we used in our research.

The SEM imaging simulation model was used to create a pseudo-SEM image from the AFM scan's height information. Seeger registered the AFM pseudo-SEM image with the appropriate sub-section of the SEM image. The dull AFM scan and SEM surface calculations were combined into a single objective function. Bayesian probability was used to find the optimal surface of a specimen given the AFM and SEM observations. Several hours were required to complete the optimized reconstruction. The time involved would most likely preclude the method from being used widely in inspection for manufacturing. Results of Seeger's fusion were compared against surface reconstructions from an AFM with a sharp tip. Ground truth specimens and simulated samples were used for comparison purposes.

In our work we focused on comparing the accuracies achievable for each microscope. We focused on stereo methods for the SEM because these could give us accurate height measurements across the surface. We hope that the work presented in this thesis will be the first step towards further research into fusion methods between the SEM and AFM, as well as a starting point for attempting to push the SEM to produce models with an accuracy even approaching the nanometer level that the AFM can achieve.

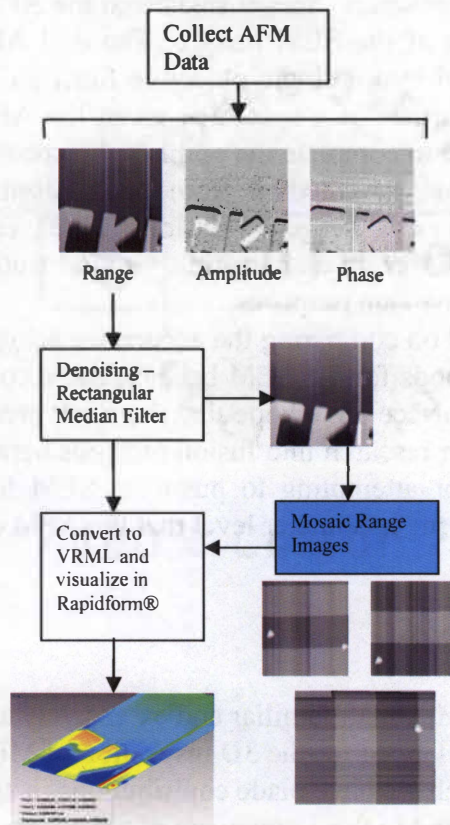
## 1.3 Contributions

The AFM, LSCM, and SEM, are all familiar and extensively used microscopes, but their potential is only now being tapped for the 3D inspection of MEMS and other nanodevices. In our research we have made contributions in applying technologies such as SEM stereo on MEMS, and in the comparison of the advantages and disadvantages of reconstructing 3D models of nanodevices with the different microscopes.

The AFM, with its direct 3D measurements, is the most widely used of the three in 3D reconstruction of MEMS devices. Obtaining 3D information from the AFM is relatively straightforward, and so our focus was on denoising the data using different sizes of median filters, and in registering 3D models of overlapping regions. Figure 1.1 shows the AFM 3D reconstruction process from beginning to end. Contributions are colored in blue.

The LSCM is more often used for biological imaging, but recently the system has been used for reconstructing 3D models of micro- or nanodevices (Schultz, 2004). The vertical resolution of an LSCM reconstruction is limited by the discrete step distance between optical slices. We have refined the LSCM reconstruction process so that the vertical resolution goes beyond this discrete, physical limitation. Our refinement was based on Niederoest et al.'s (2002) algorithm for general multifocus systems (Niederoest, Niederoest, & Scucky, 2002). Figure 1.2 shows the 3D reconstruction process for the LSCM.

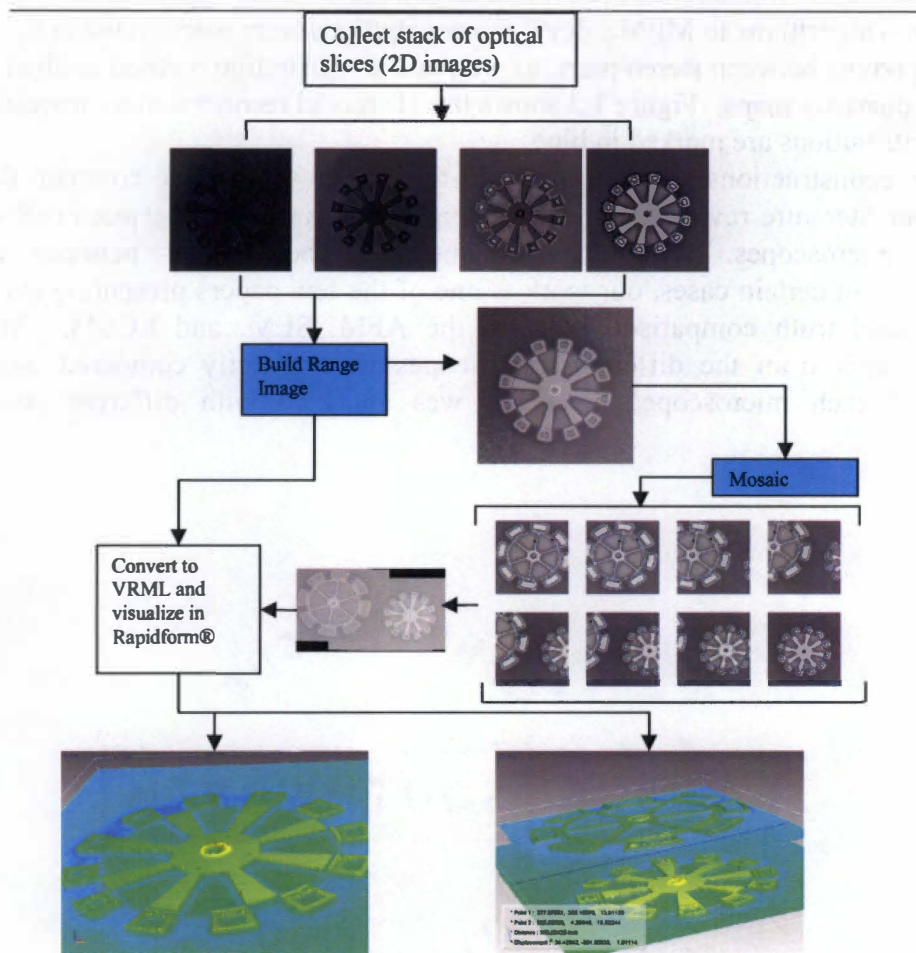
Generally, the SEM is used less than the other two microscopes for 3D inspection of MEMS. Usually only high-resolution 2D images are acquired for inspection purposes, and if 3D information is needed, a focused ion beam is used to cut cross-sections into the material. Commercial systems exist for acquiring 3D information from stereo SEM images, but they are most extensively used for the study of fracture surfaces, and research



**Figure 1.1:** Process of 3D reconstruction for the AFM. Contributions are in blue

---

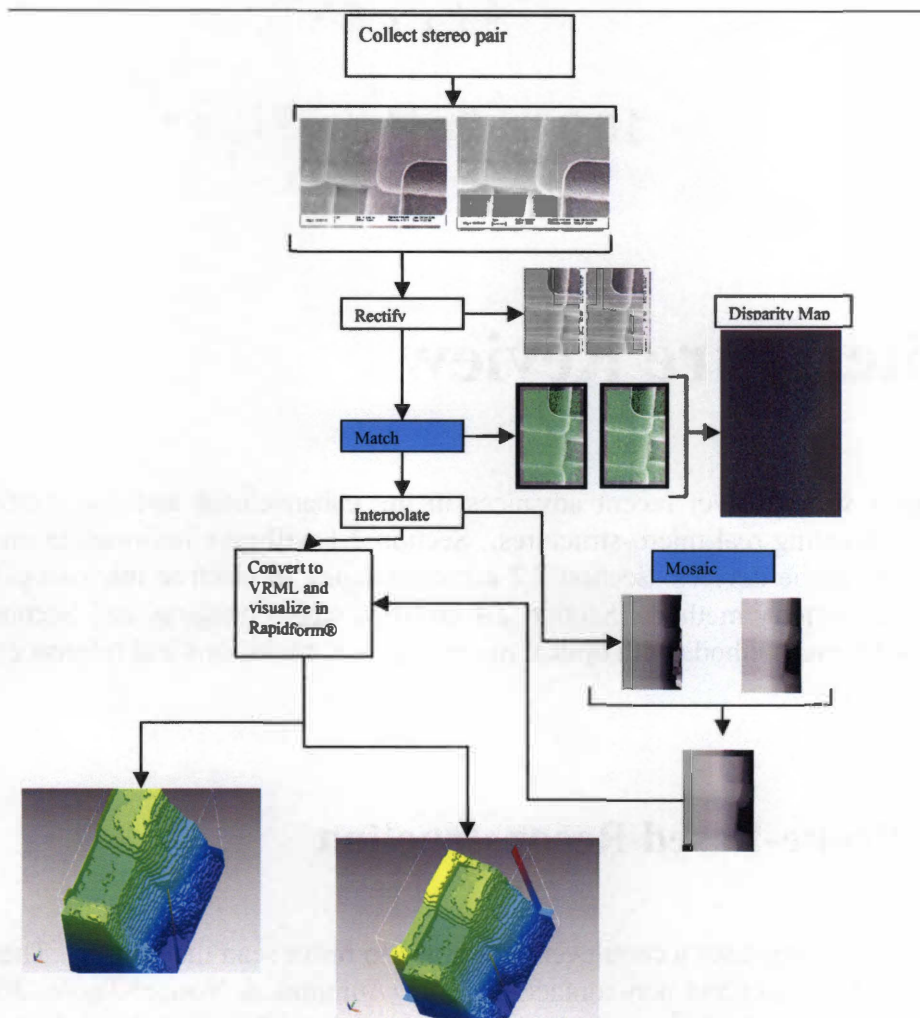




**Figure 1.2:** Process of 3D reconstruction for the LSCM. Contributions marked in blue.

into MEMS reconstruction has been minor in comparison. In applying these standard SEM stereo algorithms to MEMS devices, contributions were made in the area of matching points between stereo pairs, as well as the registration method applied to the resulting disparity maps. Figure 1.3 shows the 3D model reconstruction process for the SEM; contributions are marked in blue.

After reconstructions are done from all three microscopes, we compare the results. Within our literature review, few direct comparisons were seen between real data from different microscopes. While comparisons have been done between individual microscopes in certain cases, our work is one of the few papers presenting results of in-depth ground truth comparison between the AFM, SEM, and LCSM. 3D MEMS reconstructions from the different microscopes were directly compared against each other, and each microscope's accuracy was analyzed with different ground truth specimens.



**Figure 1.3: Process of 3D reconstruction for the SEM.**  
Contributions are marked in blue.

## 2 Literature Review

This chapter will go over recent advances in the enhancement and the creation of 3D models representing real micro-structures. Section 2.1 will give information on the AFM and scanning probe devices, Section 2.2 on tomography in electron microscopes, Section 2.3 on interferometry methods, Section 2.4 on SEM stereo imaging, and Section 2.5 will discuss multifocus methods with optical microscopes. Conclusions and references follow at the end of the paper.

### 2.1 Probe-Based Reconstruction

An AFM microscope uses a cantilever type probe to raster scan the sample. There are two types of AFM, contact and non-contact (El Rifai, Aumond, & Youcef-Toumi 2003). In contact mode, a cantilever is moved over the sample's surface and the tip's deflection is measured. The deflection amounts across the scan reveal the sample's topography. Contact mode can harm soft samples, and a non-contact AFM was developed in response. The cantilever in non-contact, or dynamic mode, is vibrated near its resonant frequency. A third mode of AFM, tapping mode, attempts to match the robustness and higher resolutions achievable with contact mode, but without damaging the sample by dragging the tip across the surface. In this mode the tip vibrates while being lowered to the surface such that it will on occasion strike the surface and lower the oscillation of the probe. Tapping mode is usually classified under non-contact, even though it would more accurately be named intermittent contact (El Rifai, Aumond, & Youcef-Toumi, 2003).

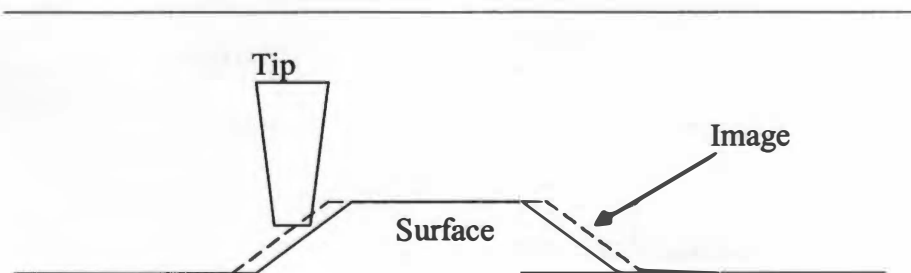
There exist two main causes of distortions present in AFM images: nonlinearity in the scanners and the finite size of the tip used to scan the surface. The first problem can be addressed using closed-loop linearity correction or strain gauges (Villarrubia, 1997). The second problem can be reduced using image reconstruction algorithms. Section 2.1.2 reviews such algorithms, preceded by a brief overview of the AFM imaging model given in Section 2.1.1.

### 2.1.1 Atomic Force Microscope Imaging Model

This section gives an overview of the AFM imaging method and illustrates how the finite tip produces distortions in recorded images. Figure 2.1 demonstrates, in surface profile, the tip's "contact" with the surface. The word contact is used here, with knowledge that depending on the type of AFM imaging mode used, "contact" could refer to actual physical contact between the tip and sample, or some minimum distance reached between the tip and object. At the point of contact, the location of the tip apex determines the height recorded at that scan location. Since the tip is finite, the contact point may not be the tip apex, and the height recorded will be in error (Villarrubia 1997). This is typically seen as a broadening, or blurring, of surface features (Castle, Zhdan, & Singjai 1998).

### 2.1.2 Image and Tip Reconstruction

An early method known as the tangential contact method, or Legendre transformation, relied on numerical derivatives to reduce artifacts found in AFM images (Chicon, Ortuno, & Abellan, 1987). Another category of reconstruction techniques make an assumption about the shape of surface features, that they are spherical or parabolic. These methods also assume that surfaces not overlapping at the point of contact must have a tangent at that point (Gainutdinov & Arutyunov, 2001). Keller and Franke (1993) proposed the envelope reconstruction method (Keller & Franke, 1993). Envelope reconstruction first builds up a set of curves describing the tip shapes and positions during scanning of the sample, and then proceeds with an envelope search of this curves set. The envelope calculated represents the reconstructed surface. The envelope reconstruction method is equivalent to morphological reconstruction methods, which currently are the most widely used methods for AFM image reconstruction.



**Figure 2.1:** Model for AFM imaging.

Morphological reconstruction methods transform the AFM imaging model into the domain of set algebra. These methods work on any shape that can be represented as a series of peaks. The broadening effect seen with the finite tip can be interpreted as image dilation with the probing tip acting as the structuring element. Villarrubia goes in-depth into the mathematical derivation of image dilation from the finite tip (Villarrubia, 1997). The image  $I$ , is formed by the dilation of the sample  $S$ , and probe  $P$  as seen in Equation (1).

$$I = S \oplus P \quad (1)$$

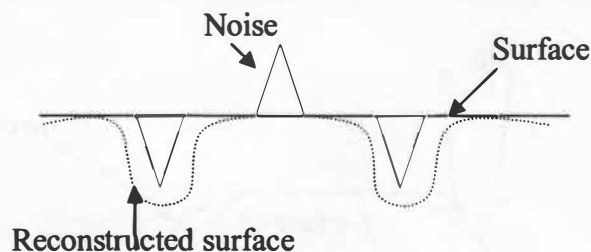
The reconstruction of the surface or sample can be obtained by erosion as shown in Equation (2).

$$S_r = I \ominus P \quad (2)$$

Current morphological algorithms have limited effectiveness in the presence of downward noise. Standard erosion techniques choose the minimum envelope so that upward noise has little effect, while downward noise is magnified as shown in Figure 2.2 (Villarrubia, 1997).

Castle et al. (1998) proposed an enhancement to standard morphological reconstruction. Their algorithm adapts to the presence of downward noise. A flat surface function acts as a closing filter where downward noise is encountered. The flat surface function has a maximum size equal to the radius of the probing tip's curvature.

If a downward feature of the AFM image is smaller than the apex of the tip it can be assumed to be downward noise and the closing filter is applied (Castle, Zhdan, & Singjai, 1998).



**Figure 2.2:** Downward noise magnified.

---

Blind restoration algorithms have been developed that reconstruct surface information with little prior knowledge of the tip or surface geometry. Villarrubia made one of the first proposals of blind restoration in (Villarrubia, 1994). The observation is made that it is only a convention that the tip be seen as the probe and the specimen as the surface being scanned. Another understanding would be of the specimen as a probe and the tip as the surface being scanned. It is possible to say that the features seen in the image are inverted and broadened replicas of the tip. The radius of the tip's apex cannot be larger than the sharpest feature in the surface image. Subsets of the image sufficiently far away from each other can be viewed as independent images, and each one places an outer-bound on the radius of the tip. The true tip shape lies within the envelope at each point equal to the tightest of all these bounds (Villarrubia, 1997). Williams (1996) arrived at the same result as Villarrubia (Williams et al. 1996).

Dongmo (1996) produced a similar method for the blind estimation for the tip (Dongmo, Troyon, Vautrot, Delain, Bonnett, 1996). Their algorithm describes a tip with only a small number of parameters. For example, assuming the probe is a simple parabolic shape it can be described by the equation  $s = r_1x$ , with  $r_1$  representing the unknown radius of the tip. The dilated image obtained using this tip is referred to as  $i_1$ .

If the experimental image were eroded with a tip with  $r \neq r_1$  and then dilated with the tip as the structuring element an image  $i \neq i_1$  is obtained. The difference between  $i_1$  and  $i$  can be calculated using a difference function.

$$d = \sum_x \sum_y |i_1(x, y) - i(x, y)| \quad (3)$$

Repeating the opening procedure for values of  $r$  less than and greater than  $r_1$  and calculating the difference allows the upper limit of the tip "radius" to be fixed.

## 2.2 Tomography

Tomography methods involve illuminating an object from different directions, and collecting transmission or reflected data in order to build cross-section images. The technique was developed to maturity in the field of medicine before being used with microscopy technologies. Primarily tomography techniques are used to reconstruct an image from its projections. In medicine, tomography allowed doctors to view internal organs in three-dimensions. The technology has since been taken and applied to non-medical fields, one particular area being electron microscopy (Kak & Slaney, 1988).

## 2.2.1 Tomography in Electron Microscopes

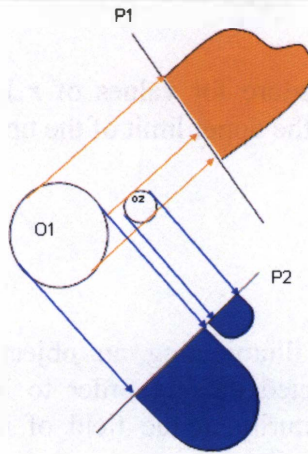
Mathematically a projection at a given angle is found by calculating the integral of the image in the direction specified by the angle. Figure 2.3 demonstrates the concept of multiple projections at different angles. Projection onto the plane  $P_1$  produces a shape with an extruding semicircle because in that direction the areas of the objects,  $O_1$  and  $O_2$ , accumulate. Projection onto the plane  $P_2$  presents the accumulated areas of the objects individually since in that direction the projection lines do not pass through both objects simultaneously.

Radon (1917) developed the principal method for reconstructing a function from its projections (Radon, 1917). The Radon transform,  $R$ , is defined as the mapping of  $f(x,y)$ , describing some object  $D$ , by a line integral (projection) through  $f$  along all possible lines  $L$  with unit length  $ds$ , illustrated in (4).

$$Rf = \int_L f(x, y) ds \quad (4)$$

Transmission electron microscopy passes an electron beam through a thin slice of the sample. Electromagnetic lenses are used to focus and magnify the beam.

In this operation the TEM is similar to a conventional light microscope, with a beam of electrons used where a light beam was originally used (El Rifai, Aumond, & Youcef-



**Figure 2.3:** Illustration of the nature of projections. Objects,  $O_1$  and  $O_2$ , are projected onto two different planes,  $P_1$  and  $P_2$ . The projections on each plane are found by calculating the integral of the object in the direction specified by the angle of projection (Kak & Slaney, 1988).



Toumi, 2003). The transmitted electron beam can be passed through the object at different angles with a different projection recorded for each angle of the beam.

Reconstruction could be done by collecting data from several projections, and then performing an inverse transformation as Radon described. Generally speaking, the majority of tomographic reconstruction algorithms are derivations or approximations of this inverse transform (Midgley & Wey, 2003). Since in practice, projections will be discrete samples of the entire projection space, the reconstruction problem becomes one of finding the 'best' reconstruction of an object given a discrete number of projections. This problem has led to several algorithms and attempts to find that 'best' reconstruction.

One of the keys of reconstruction from the Radon transform is its relationship to Fourier space. The central slice theorem states that a projection at a given angle is a central section through the Fourier transform of that object. The Fourier transform of an object,  $F(u, v)$ , and the Fourier transform of a projection,  $S$  at  $\theta = 0$ , can be related as in (Kak & Slaney, 1988), and shown here in (5).

$$F(u, 0) = S_{\theta=0}(u) \quad (5)$$

A series of projections will each match a specific segment of the object's Fourier transform. Transforming the projections into Fourier space allowed reconstruction to be accomplished by an inverse Fourier transform. Reconstruction directly from the inverse Fourier transform is known as direct Fourier reconstruction (Kak & Slaney, 1988). Practically, however, Fourier space reconstruction is not as simple as performing the inverse transform. Since the projections are at discrete angles, the Fourier reconstruction exhibits the same weakness as the radon transform, i.e. gaps in the data. With regards to the Fourier technique, discrete projections will lead to missing segments in the Fourier space. Interpolation methods are needed to fill in the gaps and allow an accurate reconstruction of the entire object (Midgley & Wey, 2003). Interpolation Fourier methods, though well defined mathematically, are computationally intensive and difficult to implement practically.

Real space back-projection algorithms are faster, and easier to implement than Fourier methods (Midgley & Wey, 2003). Direct back-projection algorithms reconstruct the object from back-projected 'rays', where a projection is defined as the inverse of a 'ray'. Reconstructions from direct back-projection demonstrate a blurred appearance. Mathematically this can be seen as a higher sampling rate near the center of the Fourier spectra, as compared the higher frequencies. This sampling imbalance can be overcome and corrected by the use of a weighting filter (Crowther, DeRosier, & Klug, 1970). This method, known as weighted back-projection, is now the most popular of the reconstruction algorithms (Midgley & Wey, 2003).

Despite its popularity, several algorithms have been developed in recent years that claim to improve on the weight back-projection methods. Reconstruction by any type of back-projection will be imperfect because of limited sampling (Midgley & Wey, 2003). Iterative reconstruction techniques, such as POCS (projection onto convex sets), have been developed in order to correct this sampling deficiency (Carazo, 1992). Entropy techniques have also been used with success. These attempts maximize the entropy from the

projections, and choose the simplest reconstruction possible from the available projections (Skoglund & Ofverstedt, 1996).

Marabini et al. (1997) compare weighted back projection methods with a new 3D reconstruction algorithm designated ART with blobs (Marabini, Rietzel, Schroeder, Herman, & Carazo, 1997). The key to this algebraic reconstruction technique is the use of functions that instead of dividing the object reconstruction space into cubic voxels use more fluid and organic shapes. Their smoothness in the spatial and frequency domain aids in increasing the accuracy of the reconstructions. The implementation of weighted back-projection used for comparison is the variation using a filter function presented in (Radermacher, 1992). Marabini et al. (1997) conclude that ART with blobs outperforms weighted back-projection in a statistically significant manner as applied to point-to-point accuracy as well as the accuracy for which bright spots are reconstructed. In a subsequent paper, Marabini et al. (1998) concluded that ART with blobs is superior to weighted back-projection when recovering features along the vertical direction (Marabini, Herman, & Carazo, 1998).

In addition the aforementioned current techniques, work has been progressing on developing faster and more accurate reconstruction techniques involving direct applications of Radon transforms. Lanzavecchia et al. (1999) presented an algorithm that recovers the 3D radon transform. It's concluded that this new algorithm outperforms WBP in terms of accuracy when the number of projections is small and runs about 10 times faster when dealing with projections numbering from 1000-5000 (Lanzavecchia, Bellon, & Radermacher, 1999).

## 2.2.2 X-Ray Nanotomography

Tunneling and probe microscopy function best when acquiring surface information (Jianwei, Ishikawa., Johnson, Anderson, Lai, & Hodgson, 2002). Transmission electron microscopes can probe the internal structures, but those structures' thickness must be less than 50 nm. X-rays have a deeper penetration depth than electrons and therefore, could better probe thicker samples. There are drawbacks that have been associated with x-ray microscopy, mainly the higher difficulty of focusing x-rays compared to a beam of electrons. The smallest focal spot is 30 nm for soft x-rays and 150 nm for hard x-rays. X-ray crystallography can be used to improve on this resolution. The resolution using x-ray crystallography is related to the quality of the diffraction from a sample. This method can only be used on structures with periodic repeats. Another method is needed to image samples at higher resolutions without limiting possible samples to those with periodic repeats.

Schroer et al. (2003) present a method for nanotomography that conducts hard x-ray microscopy with refractive lenses (Schroer et al., 2003). The authors conducted an experiment in which they built a hard x-ray microscope using parabolic refractive x-ray lenses. These lenses can record distortion free, magnified projection images. The resolution of these images is around 300 nm. The sample used to characterize their system was a fragment of a microprocessor with well defined nano-structure. The microprocessor was placed on a rotation stage and several tomographic images were taken at equidistant

steps between  $0^\circ$  and  $180^\circ$ . Figure 2.4 show a dark-field corrected projection recorded by the microscope at  $0^\circ$  and  $90^\circ$ .

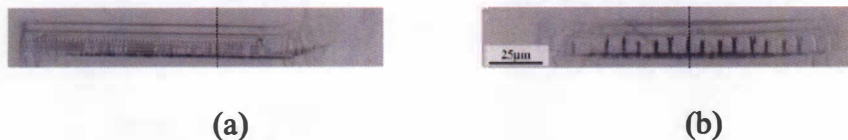
The tomographic reconstruction of these images was done using the algorithm for standard filtered back-projection in Kak & Slaney (1988). Figure 2.5 (a)-(c) shows a reconstructed slice taken from the second layer of tungsten plug vias on the processor and subsequent enlargements (Schroer et al., 2003).

Jianwei et al. (2002) combine coherent x-ray diffraction with the oversampling phasing method. Their method is summarized in the paragraph below.

The first step is to strike the specimen with coherent x-rays. This will result in x-ray photons scattering and forming a diffraction pattern in the far-field. The diffraction pattern is sampled at a rate higher than the Nyquist frequency. With this data the phase information can be obtained from the diffraction pattern using an iterative algorithm. The experiments conducted before this paper had achieved a resolution of 70 nm for 2D imaging. The authors of this paper use coherent x-rays with a wavelength of 2 angstroms to achieve a resolution of 8 nm. A sample was prepared by electron beam lithography for testing their method. It contained two single layer patterns, one on top of the other, separated by 1  $\mu\text{m}$ . The sample was dual-layered in this manner to show the ability of x-ray microscopy to discern internal information. Figure 2.6 below shows their result.

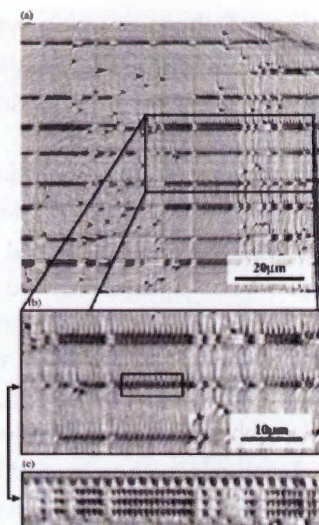
The SEM image, Fig. 2.6a, shows only top layer in any detail. The bottom layer shows up in the SEM image as blurry white spots. The x-ray microscopy image in Fig. 2.6b shows details from both layers successfully. A 45 minute exposure time, though, means that the x-ray method takes significantly longer to produce useful images than a standard SEM.

In order to obtain a 3D reconstruction, 2D diffraction patterns are obtained of the specimen at different rotations about the Z axis. The experiment described within the paper has the specimen rotated from  $-75^\circ$  to  $75^\circ$  in 5 increments. The exposure time for each pattern was 20 minutes. Combining the 2D diffraction patterns a 3D diffraction pattern can be created. The resolution of this pattern is 50 nm. Figure 2.7 below shows their results, with the first two images the reconstructed 1st and 2nd layer respectively.



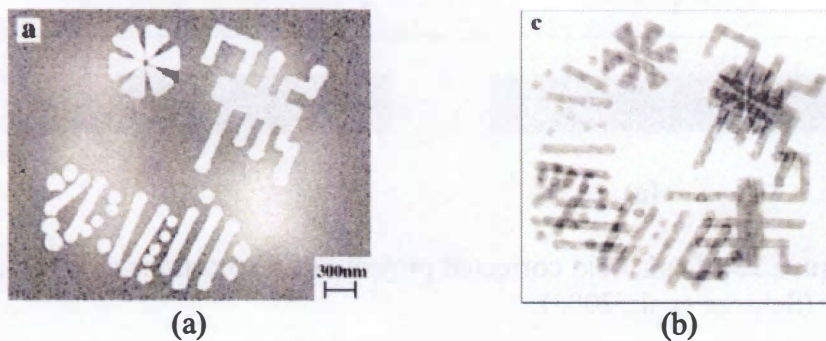
**Figure 2.4:** Dark field corrected projections. Projections at (a)  $0^\circ$ , (b)  $90^\circ$  (Schroer et al., 2003).

---



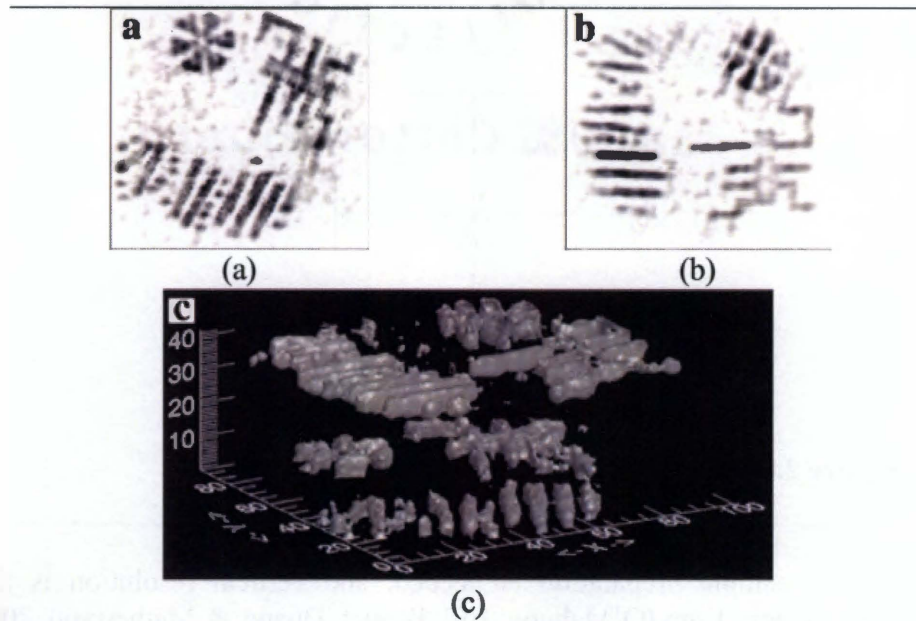
**Figure 2.5:** Reconstructed slices taken from the second layer of tungsten plug vias on a processor. (a) Tomographic slice through 2<sup>nd</sup> layer tungsten plug vias on AMD K6 processor, (b) enlarged rectangular region in (a), (c) vertical section through processor along line of plug vias marked by arrows (Schroer et al., 2003).

---



**Figure 2.6:** Comparison of SEM image and x-ray acquired image. (a) SEM image, (b) x-ray acquired image (Jianwei et al. 2002).

---

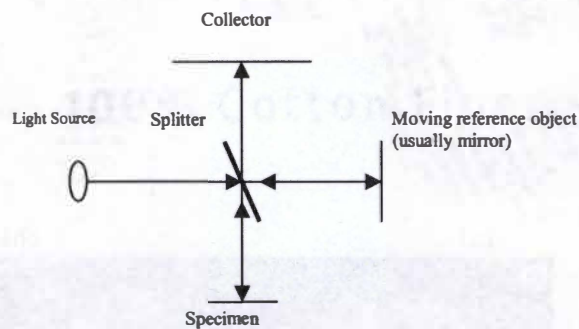


**Figure 2.7:** 3D reconstruction from x-ray microscopy. (a) 1<sup>st</sup> layer extracted (b) 2<sup>nd</sup> layer extracted (c) 3D image (Jianwei et al. 2002).

## 2.3 Interferometry and Diffraction Patterns

An intense amount of research in recent years has been directed at interferometry methods for the measurement of MEMS devices (Wang & Reading, 2003). This group of methods obtains metrological data of a specimen's surface from an interference pattern created between a reference light beam and the light reflected from the specimen (Wolfling, Banitt, Ben-Yosef, & Arieli, 2004). Figure 2.8 shows an example setup based on a Michelson interferometer.

Interferometer methods offer several advantages over conventional measurement methods such as scanning electron (SEM) or atomic force microscopy (AFM) (O'Mahony, Hill, Brunet, Duane, & Mathewson, 2003). When using an SEM, non-conductive specimens need to be coated with a conductive material such as gold to prevent charging effects. This coating adds extra stress to a MEMS device, and free-standing apparatuses such as a cantilever tip will have their performance affected. The need for coating also makes the SEM unsuitable for a product testing environment. AFM microscopes can reach greater resolution than a SEM, or any optical interferometer method, but analysis is much slower (on the order of 20 min/device) and the limited scan range (in our lab's case 90  $\mu\text{m}$  x 90  $\mu\text{m}$  x 10  $\mu\text{m}$ ) makes it difficult to investigate large devices. In contrast, interferometry measurements can be made quickly for large scan ranges, on the order of seconds rather



**Figure 2.8:** Basic interferometer setup.

---

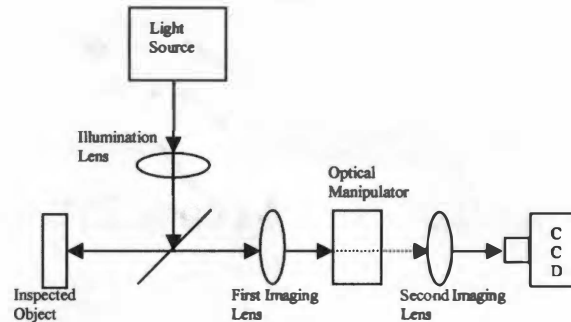
than minutes, no sample preparation is needed, and vertical resolution is more than acceptable, often below 1 nm (O'Mahony, Hill, Brunet, Duane, & Mathewson, 2003).

Scanning white light and phase-shift interferometry are two common techniques with similar implementations. Wolfling et al. (2004) present a novel implementation of phase-shift interferometry (Wolfling, Banitt, Ben-Yosef, & Arieli, 2004). In phase-shift methods, different interference patterns are created as a piezoelectric transducer moves a reference mirror to vary the phase of the reference beam. The interference patterns produced are functions of the relative phase between the wavefront reflected from the object surface, and the known wavefront reflected from the mirror. Equation (6) shows the function for the  $k$ th interference pattern measured at time  $t$ .

$$I_k(x, y) = A(x, y) + B(x, y) * \cos[\phi_k(t) + \phi(x, y)] \quad (6)$$

The point being looked at is designated by  $(x, y)$ .  $A(x, y)$  and  $B(x, y)$  refer, respectively, to the background amplitude and amplitude at the point  $(x, y)$ . The object's phase to be measured is  $\phi(x, y)$ , and is proportional to the object's surface height.  $\phi_k(t)$  is the phase induced by the mirror. There are three unknowns in (6),  $A$ ,  $B$ , and  $\phi$ . By taking measurements at three different mirror locations, these three unknowns can be solved for by using the three different equations. By taking more measurements the phase accuracy can be increased.

The method proposed by Wolfling et al. (2004) does not use a mirror in producing a reference wavefront, in fact it has no moving parts at all (Wolfling, Banitt, Ben-Yosef, & Arieli, 2004). The wavefront reflected from the object is Fourier-transformed by an imaging lens, and then is altered by an optical manipulator. The manipulator multiplies the Fourier transformed signal by functions such as amplitude modification or phase delay. This mimics the interference generated by the mirror setup shown in Figure 2.8. A second



**Figure 2.9:** Novel conception of phase-shift interferometry (Wolfling, Banitt, Ben-Yosef, Arieli, 2004).

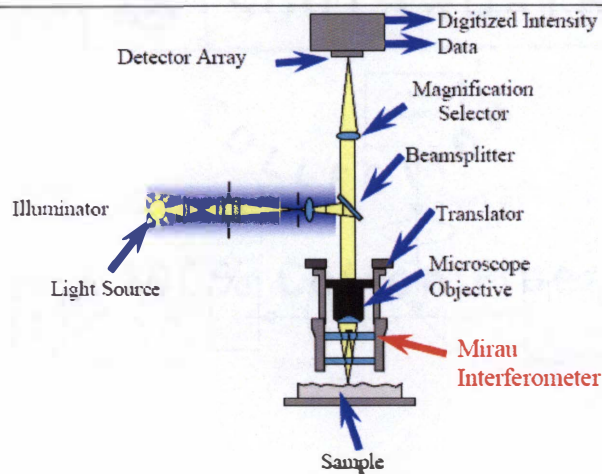
---

imaging lens performs the inverse Fourier transform. The reconstructed signal's intensity is collected by a CCD. Figure 2.9 shows the diagram of their system. A measurement of a certified step-height was reconstructed on average within 0.4 nm of the certified height.

For the characterizations of MEMS devices under stress, such as from air damping at atmospheric pressure or the material's mean residual stress, the resonances and/or shifts of their vibration frequency can be compared with respect to the values seen in a vacuum. Techniques have been developed using stroboscopic illumination, combined with interferometry, to optically measure the vibration spectra (Petitgrand, Yahiaoui, Danaie, Bosseboeuf, & Giles, 2001). In these techniques, phase-shifting techniques are often used in combination with a stroboscopic light that allows time-resolved visualization of the material's vibrations. These methods can provide sub-micron lateral and nanometer vertical resolution of the vibrations spectra.

Scanning white light interferometry technology shares similarities with phase-shift interferometry. Both techniques use the differences, or interference between a reference and sample beam. In phase-shift interferometry, the source light has only a single frequency and the phase is varied to solve for the surface profile. White light interferometry uses the full spectrum of frequencies found in white light. The setup is shown in Figure 2.10 (Hill, O'Mahony, Berney, Hughes, Hynes, & Lane, 2001).

When the sample and reference beams meet in the interferometer, a pattern of bright and dark lines results from the optical path difference between the two beams. The method of deriving a 2D height profile from white light interferometry is the same as in phase-shift interferometry, but when using white light the equations are solved at the different frequencies extracted from white light, rather than one frequency solved at different phases.



**Figure 2.10:** Scanning white-light interferometry setup (Wyant, 2002).

Hill et al. (2001) scan the MEMS object along an axis approximately perpendicular to the interferometer illuminated surface and a digital camera is used to store the intensity for each pixel in the field of view. In this way an array of interferograms is collected for each pixel. The intensity can be found for a single phase as written in (7).

$$I = \frac{1}{2}(1 + \cos(\phi)) \quad (7)$$

The interferometric phase is  $\phi$ , and is related to the optical path difference  $L$ , between the reference and object beams, i.e. the height information of the object, (8).

$$\phi = Lk + \phi_0 \quad (8)$$

Where:

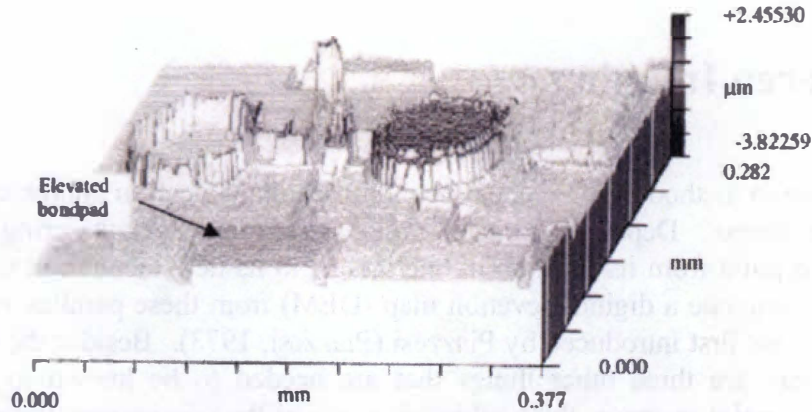
$$k = 2\pi / \lambda \quad (9)$$

and,  $\phi_0$  = phase of reference beam.

In scanning white-light interferometry (SWLI) the entire range of frequencies contained in white-light is processed using the Fourier transform to extract the phase for individual frequencies, thereby creating a system of equations which can be solved to determine  $L$ .

Figure 2.11 shows a white light interferometry profile.





**Figure 2.11:** Interferometer profile (Hill et al. 2001).

In addition to white-light and phase-shift methods, there exists a set of methods referred to as speckle interferometry. Butters & Leenderz (1971) were the first to demonstrate the technique of Electronic Speckle Pattern Interferometry (ESPI) (Butters & Leendertz, 1971). A surface with light scattering properties, exhibits a speckled appearance when illuminated by a laser light. This “speckle effect” is due to random interference, and superposition of the surface speckle pattern image with another coherent speckle pattern can be used to measure surface tomography (Butters & Leendertz, 1971). Speckle interferometry is often used with shearing techniques. Fomitchov & Krishnaswamy (1997) combine the two methods to compensate for each method’s respective disadvantages (Fomitchov & Krishnaswamy, 1997).

Lodi et al. (2002) show results given by feedback interferometry (Lodi, Merlo, Norgia, Spinola, Vigna, & Zerbini, 2002). Feedback interferometry methods require neither external optics (besides a collimator and/or focusing lens), nor an accurate alignment and wavefront matching. Instead measurements are made based on the amplitude and frequency modulation of the laser oscillation resulting when a small fraction,  $W_j$ , of the power,  $W_o$ , emitted by the source is reflected by the target and back into the laser itself. The output current from the monitor photodiode at the rear of the laser is shown in (10).

$$I = I_o + I_{\max} [(4\pi / \lambda)(s(t) + s_o)] \quad (10)$$

Where,  $\lambda$  is the laser wavelength,  $s(t)$  is distance from the target along the laser beam’s direction, and  $s_o$  is the target distance at rest. The target displacement relative to  $s_o$  can be found by detecting the zero-crossings of the signal  $I(t) - I_o$ . If there are  $M$  zero-crossings, the peak-to-peak amplitude of the target’s vibration can be found using (11).

$$S = M(\lambda / 2)(1 / \cos(\alpha)) \quad (11)$$

## 2.4 Stereo Imaging

The most common method of 3D reconstruction in scanning electron microscopes (SEM's) is depth from stereo. Depth is extracted from stereo pairs by measuring the parallax movement of a point from its location in one image, to its new location in a tilted image. Most methods generate a digital elevation map (DEM) from these parallax measurements by using equations first introduced by Piazzesi (Piazzesi, 1973). Besides the displacement of a point, there are three other things that are needed to be known to find the 3D coordinates of a point in space: the working distance of the microscope, the magnification setting, and the tilt angle. A representation of the SEM coordinate space is adapted from Piazzesi (1973) and shown in Figure 2.12 (Piazzesi, 1973).

The point,  $P$ , is a point on a specimen in 3D space. The 2D image seen by the SEM user would have  $P$  projected onto the  $z=0$  plane. The coordinates of  $P$ , in polar coordinates are given in (12)-(14).

$$\xi = a \quad (12)$$

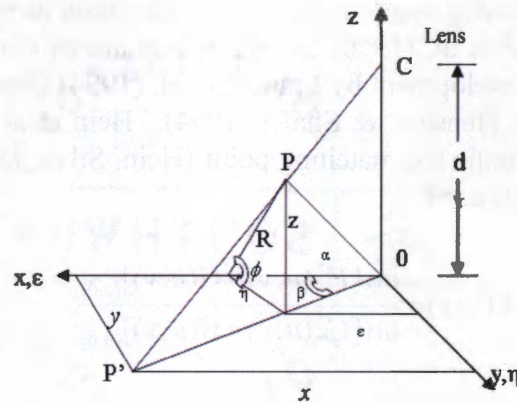
$$\eta = R \cos \phi \quad (13)$$

$$z = R \sin \phi \quad (14)$$

The coordinates of  $P'$ , projected onto the  $z=0$  plane with planar coordinates,  $(x,y)$  are found using (15)-(16).

$$x = \frac{a}{1 - \left(\frac{R}{d}\right) \sin \phi} \quad (15)$$

$$y = \frac{R \cos \phi}{1 - \left(\frac{R}{d}\right) \sin \phi} \quad (16)$$



**Figure 2.12:** Geometry of SEM microscope.

The paper develops equations to determine how a point,  $P$ , would be projected differently under different tilt angles. The height,  $z$ , would determine the amount of movement seen when projected onto the  $z=0$  plane. The working distance for a point would be different based on the tilting, but if considered as equal, a not uncommon assumption, and in situations where the working distance,  $d$ , of the microscope is sufficiently larger than the object being examined the height can be found of one point as seen in (17).

$$z \approx \frac{1}{M} \frac{Y_1 - Y_2}{2 \sin(\Delta\phi)} \quad (17)$$

Where  $Y_1$  and  $Y_2$  are the coordinates of the point before and after tilting, and  $M$  is the magnification factor.

This basic idea has been taken and expanded upon in the last thirty years. El Ghazali (1984) and Gleichmann et al. (1994) presented calibration techniques to enhance the accuracy of stereo imaging under SEM's (El Ghazali, 1984; Gleichmann, Koehler, Hemmleb, & Albertz, 1994).

Most research in this discipline has focused on methods for finding matching points between the two tilted images. Matching points must be found in order to calculate the disparity, or distance traveled, by one point from image to image. Several different papers tackle this problem in varying ways, but matching algorithms generally fall into two categories, area-based matching and feature matching.

In area-based matching a template is taken from the untilted image and shifted pixel by pixel within a window, search area, of the tilted image. In order to determine at which point the match is best, and therefore the matching point, there are generally two types of

measures that are taken. These are calculations of the grey-level difference or correlation between the template and current section of the search area.

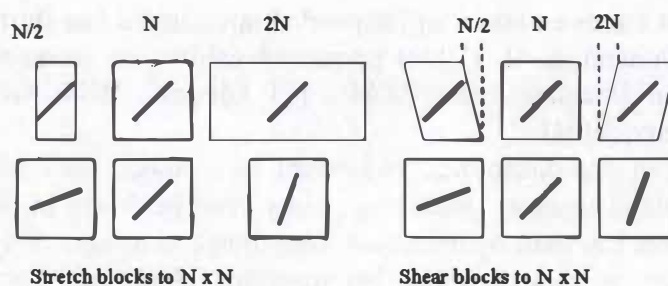
Other area-based matching methods use cross-correlation as their basis for determining the match point. Stampfl et al. (1996) use the maximum of correlation to determine the best match and note its development by Frankot et al. (1994) (Stampfl, Scherer, Gruber, & Kolednik, 1996; Frankot, Hensley, & Shafer, 1994). Hein et al. (1999) used normalized cross-correlation to determine the matching point (Hein, Silva, Nazar, & Ammann, 1999). Eq. (18) shows the formula used.

$$N(x, y) = \frac{\text{inv}[F^*(u, v) \bullet G(u, v)]_{(0,0)}}{\text{inv}[G^*(u, v) \bullet G(u, v)]_{(0,0)}} \quad (18)$$

Lacey et al. (1998) use stretch correlation as an enhancement to the basic correlation techniques (Lacey, Thacker, Crossley, & Yates, 1998). This method models the surface rotations, caused when rotating the specimen, by stretching or shearing the right image blocks. This warping increases the stability of the correlation process and therefore can produce more accurate disparity calculations. An example of this method's stretching or shearing is shown in Figure 2.13 below.

Feature based matches typically find edges or other distinguishable points which exhibit large differences with their surrounding environment. Interest operators such as edge detectors are used to determine where features lie. Hemmleb and Schubert (1997) describe using feature-based detection to reconstruct a trapezoidal object (Hemmleb & Schubert, 1997). A Canny edge detector was used and the corresponding edges were matched to find the disparity.

Minoshima et al. (2000) use both grey-level and correlation based methods. The measure SSDA (sequential similarity detection algorithm) computes the sum of the grey-level difference between the pixels of the template and current search area (Minoshima, Suezaki, & Komai, 2000).



**Figure 2.13:** Illustration of shearing techniques to aid in alignment of SEM stereo images (Lacey, Thacker, Crossley, & Yates, 1998).

The equation is given in (19).

$$R_s = \sum_{ij} |T_{ij} - S_{ij}| \quad (19)$$

$T_{ij}$  and  $S_{ij}$  represent the grey-level values at point  $(i,j)$  in the template and searched areas respectively. The point where  $R_s$  takes a minimum is considered the matching point.

Minoshima et al. (2000) also implement the MCC (mutual correlation coefficient) method for finding matching points (Minoshima, Suezaki, & Komai, 2000). In this method a correlation is computed between the two areas and the point at which a maximum is found can be considered the matching point. The formula for MCC is shown in (20).

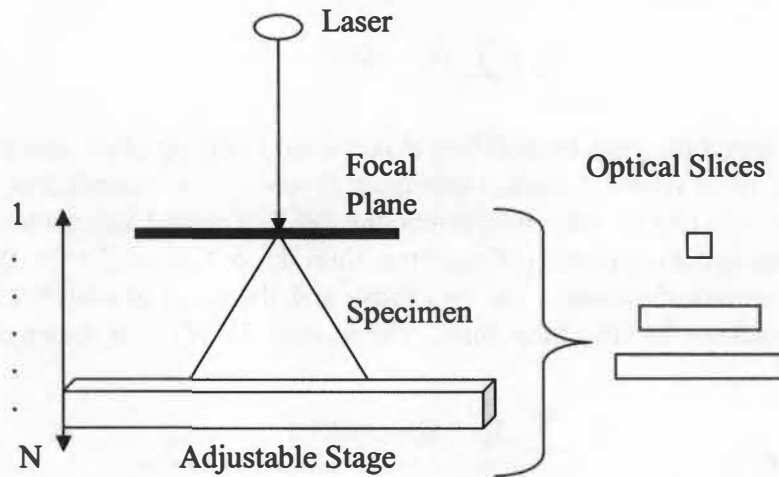
$$R_c = \frac{\sum_{ij} T_{ij} * S_{ij} - N \bar{T} \bar{S}}{\sqrt{(\sum_{ij} T_{ij}^2 - N * \bar{T}^2) * (\sum_{ij} S_{ij}^2 - N * \bar{S}^2)}} \quad (20)$$

Minoshima et al. (2000) use genetic algorithms to refine their search process and produce results more accurate than standard correlation methods (Minoshima, Suezaki, & Komai, 2000). The drawback is it takes several times longer to complete than a two-step coarse-to-fine search using correlation. The genetic algorithm process though is faster than a one-step entire search algorithm.

## 2.5 Depth from Focus

Algorithms use focus to find depth by taking advantage of a microscopic system's focus limits. Systems with the ability to achieve the lowest depth of focus can achieve the most accurate 3D reconstructions. Multifocus methods extract depth by acquiring multiple images at different focal planes, with the reconstruction done by evaluating in which image an area of the scene appears most in focus. By knowing at what heights the focus was set over an image series, depth can be assigned to pixels based on which image they are sharpest in. The following sections discuss methods for extracting this depth information.

Confocal microscopy is especially useful in extracting depth from focus. The design of the microscope is such that the plane of focus through a specimen is very narrow along the axial axis, and therefore, allows for accurate depth information (Yatchmenoff & Compton, 1990). Figure 2.14 demonstrates how an object is optically sliced. The microscope's small aperture blocks most out-of-focus light. Generally, the stage translates an object vertically through the thin focal plane and a series of images is taken that describe the object. To find the height of a pixel, the image series is searched to find the image where the pixel's intensity is a maximum.



**Figure 2.14:** Illustration of confocal optical slicing.

Several different methods exist in the field for extracting the depth information and building a complete 3D model from it. Pudney et al (1994) examine methods for the detection of surfaces in confocal microscopy (Pudney, Kovesi, & Stretch, 1994). The ability to detect feature types aids in the 3D reconstruction of the optical slices. In their method, feature detectors compute local energy by convolving an image with oriented, quadrature pairs of 3D filters.

Roederlink (1994) uses the fast Fourier transform to perform convolution and iteratively works to restore more accurate confocal images (Roederlink, 1994). Another method utilizes the maximum likelihood method to better optically section images. Stefanou & Hansen (1994) apply two image restoration methods to slices from a confocal microscope, the Expectation Maximization (EM) algorithm utilizing ML methods, and the JVC algorithm (Stefanou & Hansen, 1994). An advantage of the ML methods is they optimize the images under the constraints of Poisson noise, which is the type of noise most often seen in microscopic images at high magnification.

Several methods of deconvolution are used as a means of increasing the confocal's axial resolution. These methods increase the accuracy by boosting the information at lower light levels, and more accurately determining which parts of the image truly represent the current focal plane (Mcnally, Karpova, Cooper, & Conchello, 1999). Though confocal microscopes are designed to block out-of-focus light using the pinhole aperture, it is inevitable that some parts of the image will be from out-of-focus planes due to the imperfections of the lens. Deconvolution methods based on the PSF of a confocal microscope can be used to improve the accuracy of the images obtained (Shaw, 1995). When imaging MEMS devices, the need for deconvolution is less since as opposed to

living cells, MEMS devices can withstand high intensity lasers for extended periods of time. This leads to decreased noise and blurring effects that are common in low-intensity fluorescence imaging.

Kempen et al. (1996) compare two restoration methods for confocal microscopy, iterative constrained Tikhonov-Miller (ICTM) and expectation-maximization algorithm for computing the maximum likelihood estimator (EM-MLE) (van Kempen, vander Voort., & van Vliet, 1996). Both methods reduced diffraction distortions, but in their experiments the EM-MLE algorithm produced better results than the standard ICTM method.

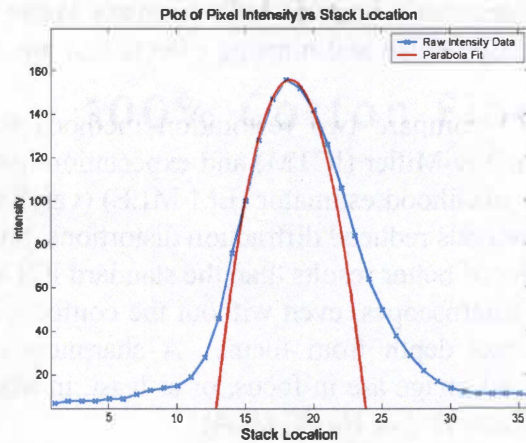
Conventional optical microscopes, even without the confocal's ability to block out-of-focus light, can still extract depth from focus. A sharpness or contrast function can determine which parts of an image are in focus, or at least, in which image of a series the subject is most in focus (Zamofing & Hugli, 2004).

In a recent review of sharpness functions, Santos et al. (1997) classified sharpness functions into five categories: (1) image differentiation; (2) depth of peaks and valleys; (3) image contrast; (4) histogram and (5) correlation measurements (Santos et al., 1997). All five categories work on one basic assumption, that in a focused image grey-levels are more widely distributed, with a greater variance, or absolute difference between the brightest and darkest pixels, as compared to a blurred image where the grey-levels of neighboring pixels pool together and an average of their grey levels is seen in that region.

Image differentiation algorithms assume that in unfocused images, there are only small differences between light and dark areas, since in blurring a single pixel's value is spread among several neighboring pixels. The Tenegrad function, described by Krotkov (1987), used the Sobel vertical and horizontal edge detectors to determine the strength of the image gradient (Krotkov, 1987). Pech-Pacheco, Cristobal, Martinez, & Valdivia (2000) present modified Tenegrad and Laplacian methods as focus criterions. The image differentiation methods are modified by calculating the variance of gradient magnitudes (Pech-Pacheco, Cristobal, Martinez, & Valdivia, 2000). Nayar and Nakagawa (1994) present a sum-modified Laplacian (SML) method. They compute a sum of modified Laplacian values in a small window around the point of interest and take the result as a focus measure, the maximum pertaining to the most highly focused region (Nayar & Nakagawa, 1994).

The 'depth of peaks and valleys' methods also work on the assumption that a focused image has a wider range of grey-levels than a blurred image. These functions compute the number of pixels above or below a specified threshold. Santos et al. (1997) cites Groen, Young, & Ligthart (1985) as an example (Groen, Young, & Ligthart, 1985). Recent literature has not focused as greatly on these measures.

Variance measures are typically used in determining image contrast, with high variance corresponding to high contrast and an in-focus region. Niederoest, Niederoest, Scucka (2002) use local variance as a focus criterion, but post-process the results to more accurately fix a point's depth in space (Niederoest, Niederoest, & Scucka 2002). After a point's local variance measure has been calculated in each image of a series, a graph of these different variances is produced such as in Figure 2.15. Niederoest et al. fit a curve through the points, and use the location of the fitted curve's



**Figure 2.15:** Plot of variance data (blue) versus image stack location fitted with a curve (red).

---

maximum, to interpolate a height in between in the discrete focus levels, also seen in Figure 2.15.

Histogram methods assume that blurred images have a lower number of discrete grey levels than an in-focus image. Algorithms determining the difference between the max and min grey level have been developed, as well as algorithms using entropy. Kristan and Pernus proposed a frequency domain entropy method (Kristan & Pernus, 2004). The assumption in this method is that a sharp image contains a more uniform distribution of frequencies, as compared to a blurred image with a higher concentration of low frequencies. By definition, a uniform sampling will have higher entropy than one with concentrations in a single region of the spectrum.

Working in the frequency domain, Widjaja developed a wavelet based focus criterion for autofocusing applications (Widjaja, 2000). Using the wavelet transform ability to detect edges, images were analyzed for edge content, and a focus found where the maximum edge content was present. A comparison was made to autocorrelation results for autofocussing as described in Jutamulia et al. (1994), and the wavelet focus criterion showed improved performance (Jutamulia, Asakura, Bahuguna, & De Guzman, 1994).



## 3 Data Acquisition

This chapter details the samples used for data collection and the manner of that data collection with the AFM, LCSM, and SEM. Section 3.1 gives information on the samples we imaged; Section 3.2 introduces the AFM, section 3.3 the LCSM, and section 3.4 the SEM.

### 3.1 Information On Our Samples

In our research we collected data from two types of samples, a polyMUMPS chip from MEMSCAP and a set of calibration gratings for ground truth analysis. The polyMUMPS device has on it an array of MEMS devices: wobble and harmonic motors, resonators, and hestuator arrays. Figure 3.1 shows the layout provided to us by MEMSCAP, and Figure 3.2 shows an optical microscope image of the MEMS devices.

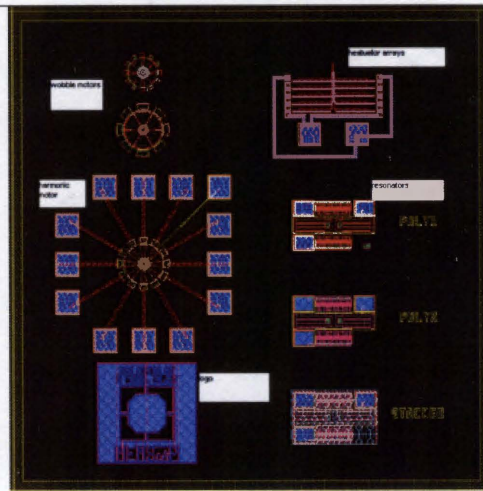
We used the TGZ calibration grating series from MikroMasch, TGZ01, TGZ02, and TGZ03 (MikroMasch, 2005). On each silicon chip a series of step heights are engraved into the silicon surface. Figure 3.3 shows an image of the series as acquired by an SEM. Table 3.1 shows the specifications for the height and standard deviation for the gratings.

Table 3.1 lists the height specification and error associated for each grating.

### 3.2 The Atomic Force Microscope

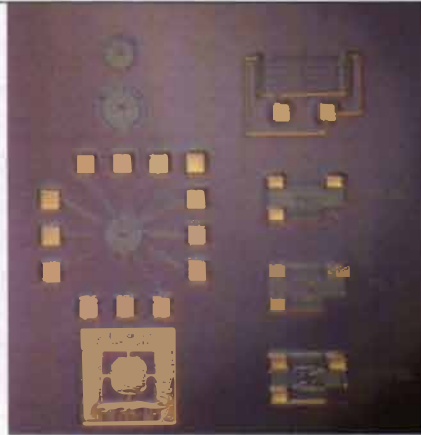
The Asylum Molecular Force Probe 3D, (MFP-3D™), was used to collect data from MEMS devices (Asylum, 2004). Figure 3.4 shows an image of the system.

All three axes of stage movement are sensed to maintain a high accuracy and minimize noise. The system operates in closed loop and monitors the position of each axis. Hysteresis and creep are common problems with piezo scanners. Hysteresis refers to the difference in readings from the increasing and decreasing forces. Creep refers to how an output changes with time.



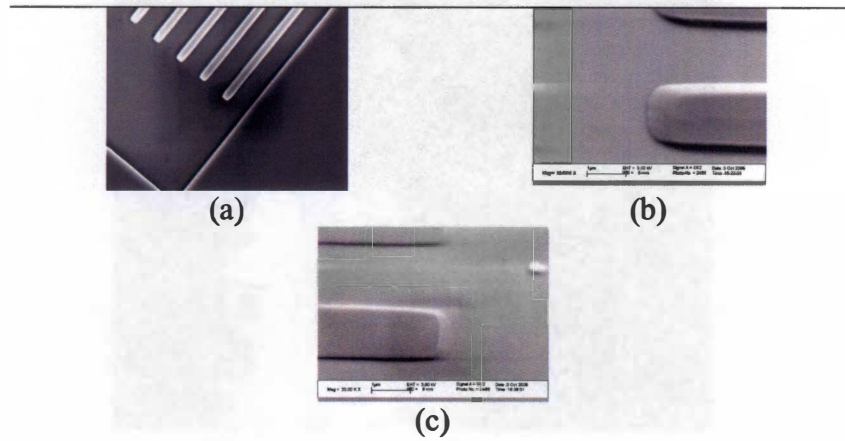
**Figure 3.1:** Design layout of MEMS devices scanned in our research.

---



**Figure 3.2:** Optical microscope image of MEMS devices.

---



**Figure 3.3:** SEM images of calibration gratings. Step heights for each sample are certified at (a) 500 nm, (b) 100 nm, and (c) 18 nm.

**Table 3.1:** Calibration gratings

Model	Pitch	Step height
TGZ01	~ 3.0 $\mu\text{m}$	18.8 nm $\pm$ 0.6 nm
TGZ02	~ 3.0 $\mu\text{m}$	100.9 nm $\pm$ 1.2 nm
TGZ03	~ 3.0 $\mu\text{m}$	514.8 nm $\pm$ 5.0 nm



**Figure 3.4:** Image of Asylum Molecular Force Probe 3D AFM.

---

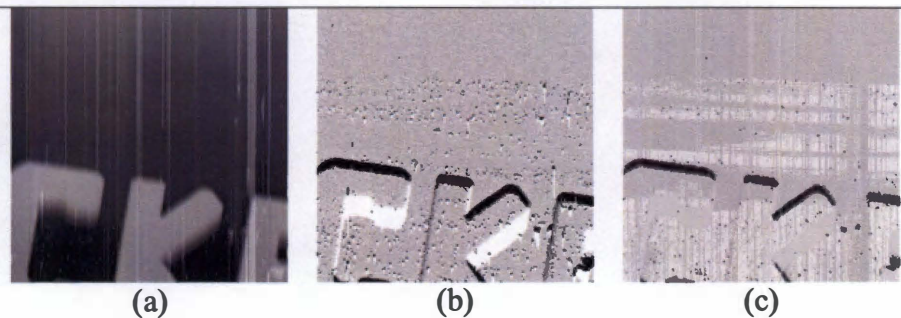
The NPS system corrects for the hysteresis and creep problems associated with piezo scanners. Noise levels are at  $< 0.2$  nm in the Z direction, and  $< 0.4$  nm along the X and Y axes. Table 3.2 contains detailed specifications for the system.

There are two main settings for each scan, the scan size, and the sampling rate. The scan size varies from (minimum) to  $100 \mu\text{m}^2$ ; the sampling rate varies from (minimum) to  $5000 \times 5000$ . A  $256 \times 256$  scan of a  $20 \mu\text{m}^2$  area, takes 5 minutes. Rather than a dense sampling of a large area, this project focused on small scans sampled at  $256 \times 256$ . Figure 3.5 shows the height, phase, and amplitude images from an AFM scan of letters on a MEMS device. Scan size is  $90 \mu\text{m}^2$ , with  $256 \times 256$  sampling.

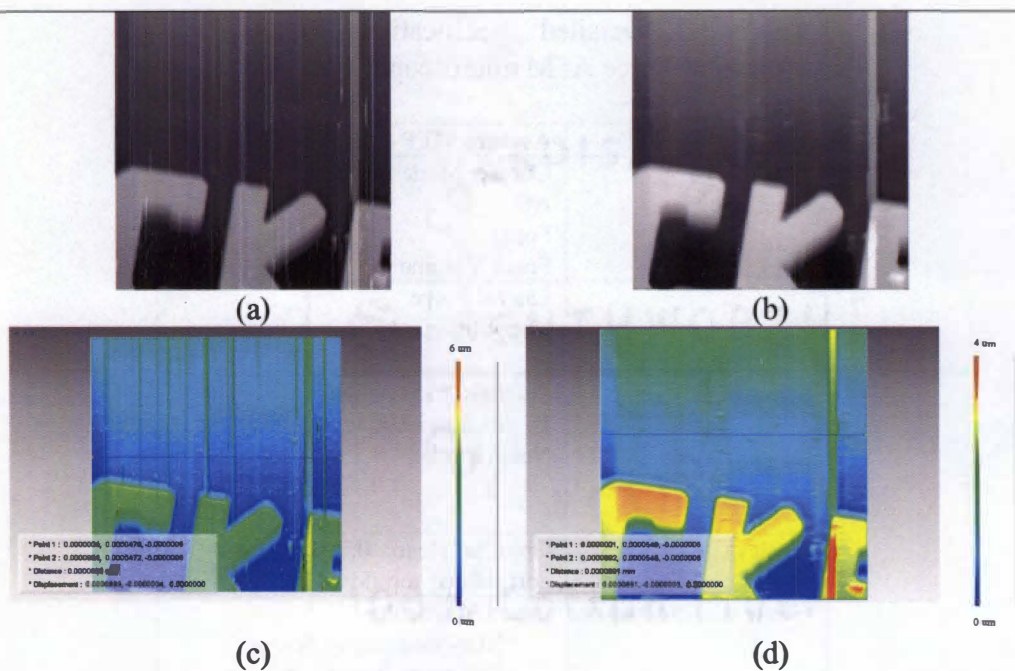
The speed of the probe when scanning large areas ( $> 50 \mu\text{m}^2$ ) at low sampling is high and can cause noise in the data. Occasional vibrations in the building may also create noisy 'streaks' as seen in the AFM data shown in Figure 3.5. Median filtering is an efficient remedy for this type of spiky noise. When dealing with long lines of noise such as in Figure 3.5, the median filter can be altered from its standard square format (e.g.  $5 \times 5$ ) to a rectangular shape, such as  $2 \times 5$ . Figure 3.6 shows results of median filtering the height image in Figure 3.5(a), as well as the raw and filtered 3D models produced from the height images.

Decreasing the scan size, while holding constant the sampling rate, naturally increases the resolution of the AFM's probe. Figure 3.7 shows a series of 3D models collected from the AFM for an area of  $15 \mu\text{m}^2$ ,  $5 \mu\text{m}^2$ , and  $1 \mu\text{m}^2$  respectively with the same sampling rate.

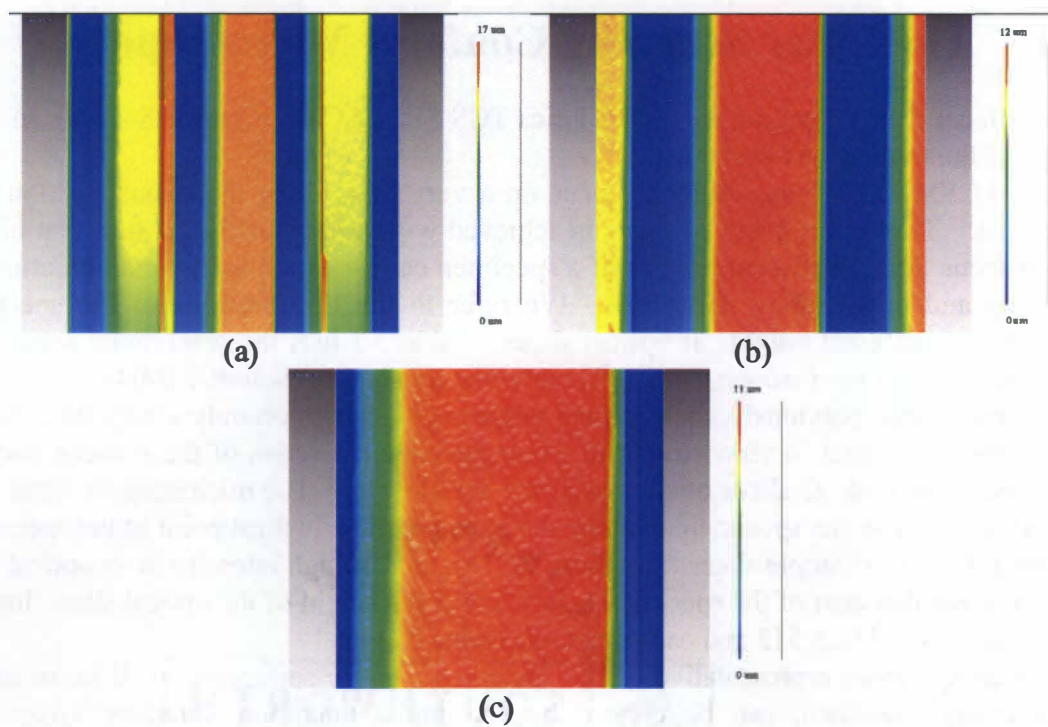
<b>Table 3.2: Detailed specifications for Asylum Molecular Force AFM microscope.</b>	
	<b>Asylum MFP-3D</b>
<b>Modes of Operation</b>	Contact Mode AC Force Force Volume Lateral Force Nanolithography/nanomanipulation
<b>Scanning stage</b>	Piezoelectric scanner 16 $\mu\text{m}$ Z and 100 $\mu\text{m}$ XY-Range, Noise levels: < 0.2 nm in Z < 0.4 nm in XY
<b>Optics</b>	OptoPort Head: 0.3 N.A. optical port, allows top-down viewing
<b>Controller/Software</b>	Based in Igor Pro : Non-linear curve fitting : Extensive Image Analysis : Automatic spectral fitting and Cantilever calibration : Easy creation of publication ready graphs, layouts, images : Can acquire 5000x5000 pixel images



**Figure 3.5: Results of AFM scan. (a) Height/range image, (b) amplitude image showing the variation of driving current's amplitude, and (c) phase image showing the variation of driving current's phase.**



**Figure 3.6:** Results of median filtering AFM scan in Figure 3.5. (a) Raw height image, (b) Median filter of size 2x10 applied, (c) 3D model created from raw data in (a), and (d) 3D model of filtered data in (b). Original data 256 x 256, pixel size 0.3  $\mu\text{m}$  / pixel.



**Figure 3.7:** Series of AFM 3D models demonstrating the effect of resolution. The dimensions and physical resolution of each image are (a)  $15 \mu\text{m}^2$  and  $58 \text{ nm/pixel}$ , (b)  $5 \mu\text{m}^2$  and  $19 \text{ nm/pixel}$ , and (c)  $1 \mu\text{m}^2$  and  $4 \text{ nm/pixel}$ .

### 3.3 The Laser Scanning Confocal Microscope

For confocal data collection, we used a Leica TCS SP2 LSCM. Figure 3.8 shows an image of the microscope system.

An LSCM has the capability to focus on a very thin, along the z-axis, section of a specimen. This small depth of focus is achieved with a very small aperture that blocks out-of-focus light. Different heights of a specimen can be examined by manipulating the stage up and down along the z-axis. We refer to the thin sections of the specimen examined at different heights as optical slices. Table 3.3 lists the resolutions achievable with the confocal microscope using different objective lenses (Schultz, 2004).

As mentioned previously, the confocal microscope focuses on only a very thin slice of a specimen. In order to reconstruct the whole specimen, a series of these slices must be collected. We took 92 slices of an area of the MEMS chip. The microscope's focus was moved from below the specimen up along the z-axis past the highest point of the specimen. Figure 3.9 shows example slices from these 92. An area of high intensity in an optical slice indicates that that area of the specimen is in focus at the height of the optical slice. Images in Figure 3.9 are 512 x 512 and each pixel represents 0.6  $\mu\text{m}$ .

An image more representative of the specimen's entire surface, as well as an image more easily examined, can be created by forming a maximum intensity image. A maximum intensity image is formed by traveling up through the stack for each pixel and then extracting each pixel's maximum intensity. Figure 3.10 shows a plot of one pixel's intensities through the stack of 92 slices.

This can be done for each pixel and an example result is shown in Figure 3.11.



**Figure 3.8:** Leica TCS SP2 LSCM.

---

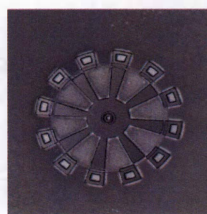


**Table 3.3:** Resolution along Z and XY axes for confocal microscope using different objective lenses.

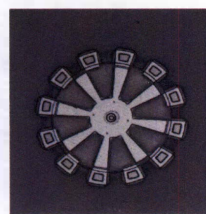
Objective lens	Z res ( $\mu\text{m}$ )	XY res ( $\mu\text{m}$ )
10x Dry	4.661980	0.701638
20x Dry	0.751145	0.300702
40x Oil emersion	0.342945	0.175410
63x Dipping	0.626292	0.233879
63x Water emersion	0.290384	0.175410
63x Oil emersion	0.292125	0.161917
100x Oil emersion	0.239276	0.150351



(a)

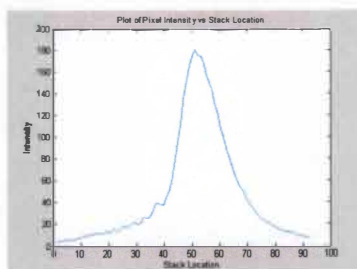


(b)

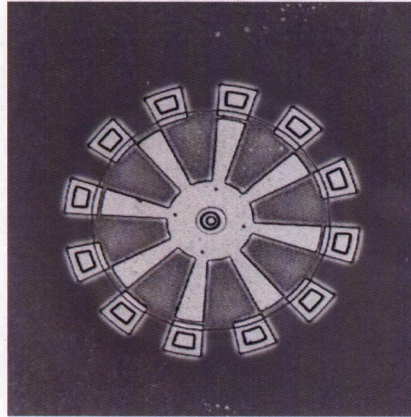


(c)

**Figure 3.9:** Selected images from a stack of 92 optical slices taken by the confocal microscope. (a) Slice 22, (b) Slice 42, (c) Slice 52.



**Figure 3.10:** Maximum intensity values for a single pixel, constructed from confocal optical slices of a harmonic motor.



**Figure 3.11:** Maximum intensity image of a wobble motor, constructed from confocal optical slices. Image is 512 x 512 with each pixel representing 0.6  $\mu\text{m}$ .

---

### 3.4 The Scanning Electron Microscope

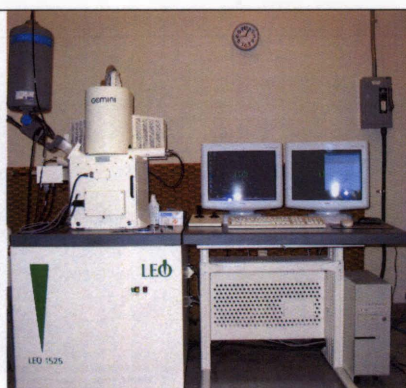
Figure 3.12 shows the SEM used for MEMS data collection. Charging is an issue when acquiring data from the SEM. Charging occurs when electrons projected by the SEM collect on the surface of a specimen producing bright, blooming areas on the image. This effect will not occur on specimens that conduct electricity, since electrons will spread away from the contact point. Surprising charging occurred on the MEMS chips. Figure 3.13 shows images gathered from the SEM that demonstrate the charging effects.

The samples that we acquired from MEMSCAP have a photoresist coating which could have caused the charging. We followed the instructions given by MEMSCAP, and soaked the MEMS devices in a solution of acetone, and then rinsed with isopropyl alcohol and de-ionized water. Figure 3.14 shows an SEM image of the cleaned MEMS device, with no charging effects.

In order to aid in the 3D reconstruction of the MEMS specimen we performed some pre-processing of the raw microscopy data. Often the SEM stereo pair images exhibit salt-and-pepper type noise and can produce images of low contrast and non-uniform illumination as seen in Figure 3.15.

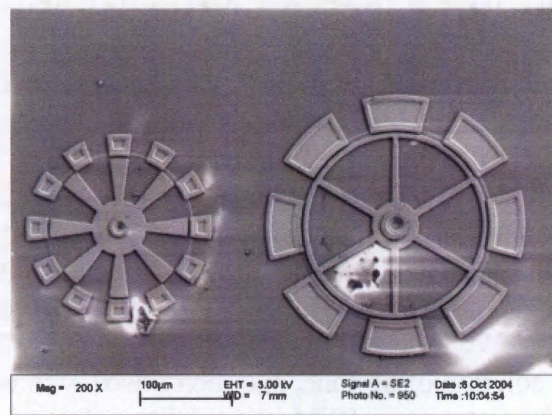
Filtering by a 3x3 median filter is used to remove noise. The contrast is then stretched for each image, but that still leaves an illumination difference between the tilted images as can be seen in Figure 3.16.

The difference in illumination can be approximated as a uniform change in intensity. To correct for this, the difference between the first and second image is calculated, averaged, and then added to the second image. Results are shown in Figure 3.17.



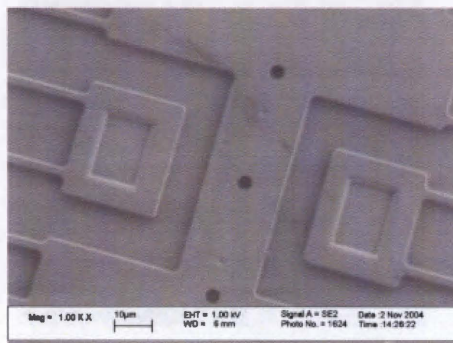
**Figure 3.12:** Image of Leo 1525 SEM microscope.

---



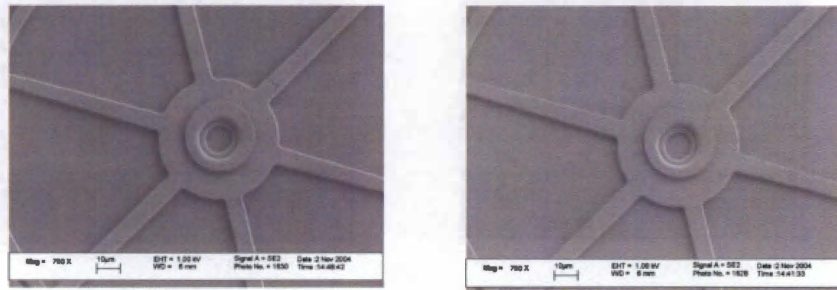
**Figure 3.13:** SEM image of MEMS chip with charging effects in bright white.

---



**Figure 3.14:** SEM image of MEMS chip without charging effects.

---

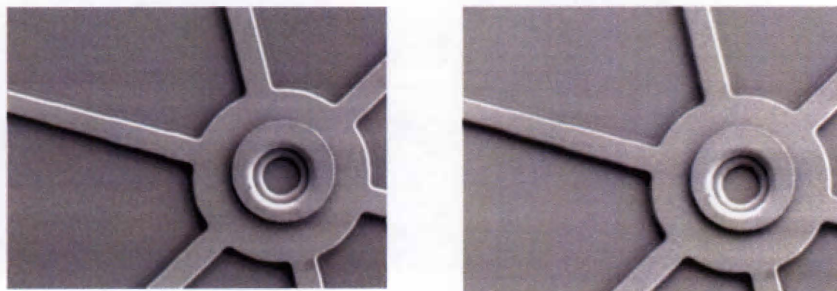


(a)

(b)

**Figure 3.15:** SEM images taken at different tilt angles showing different illumination effects, low contrast, and salt-and-pepper noise.

---

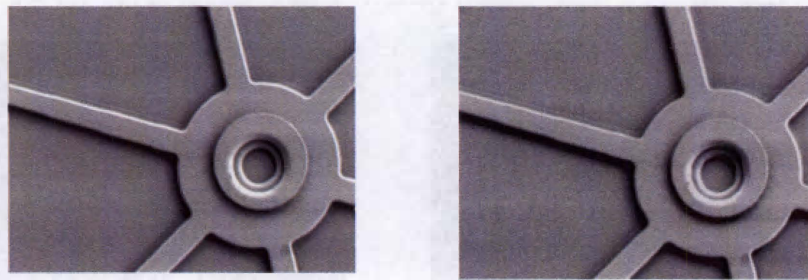


(a)

(b)

**Figure 3.16:** Median filtered and contrast stretched SEM images at different tilt angles, still showing different illumination effects.

---



(a)

(b)

**Figure 3.17:** Stereo pair from SEM with noise filtered, contrast stretched, and illumination adjusted to be approximately uniform between the pair.

---

## 4 3D Reconstruction

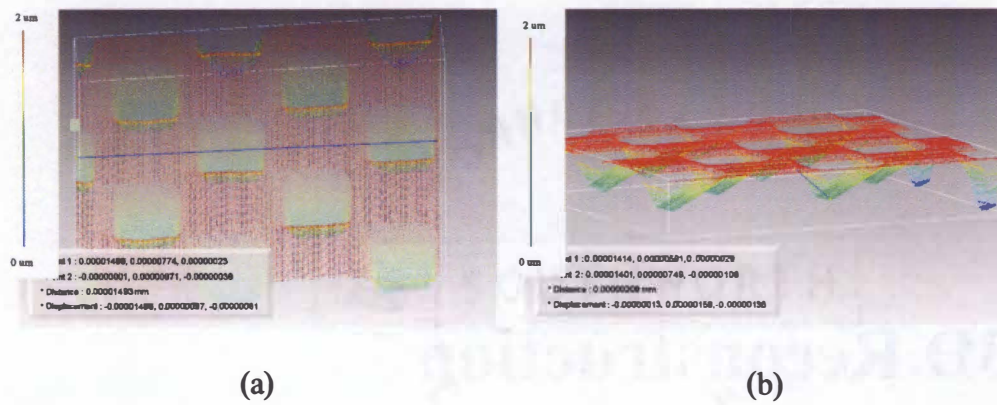
In this chapter the implementation and refinement of 3D reconstruction algorithms will be looked at for each of the individual microscopes. Section 4.1 will discuss denoising and visualizing the AFM range data. Section 4.2 will discuss the multifocus method used for 3D reconstruction of LCSM data, and section 4.3 will discuss the depth from stereo method used for SEM reconstruction.

### 4.1 Atomic Force Microscope

An AFM microscope is a range finding device. The raw data from the AFM microscope is a matrix of height values sampled across a surface, with the size of the matrix equal to the number of data points taken. This matrix can be converted into a virtual reality modeling language (VRML) file, where each matrix location is assigned an X and Y coordinate and the height data stored in the matrix at that location is assigned as the point's location along the Z axis. The VRML file of the points can be visualized in Rapidform® (software package), as seen in Figure 4.1. In Figure 4.1 a model of an AFM calibration grid is shown. The original size of the scan was 15  $\mu\text{m}$  x 15  $\mu\text{m}$ , sampled with 256x256 pixels, each pixel representing 58 nm.

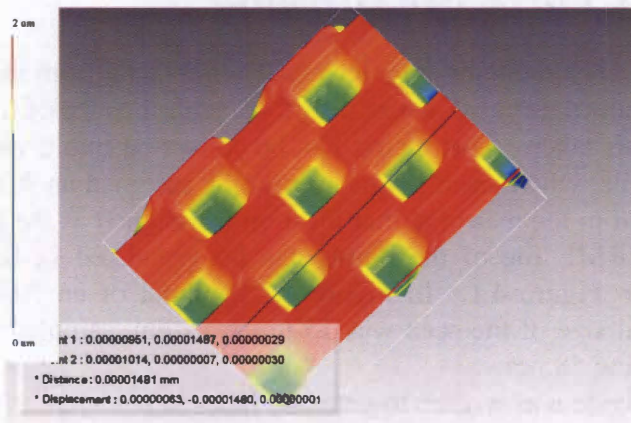
In the next step code was written to generate faces to connect the points of the mesh so that a mesh of triangles covered the surface of the 3D model. Figure 4.2 shows the calibration grid from Figure 4.1 with a surface generated to connect the points.

We also scanned the MEMS device provided by MEMSCAP. Figure 4.3 shows a model generated from a 90  $\mu\text{m}$  x 90  $\mu\text{m}$  scan of an area of the MEMS chip containing the word "STACKED".



**Figure 4.1:** AFM range data converted to VRML file and visualized in Rapidform®. (a) and (b) are two different views of the same specimen. Measurements are in meters.

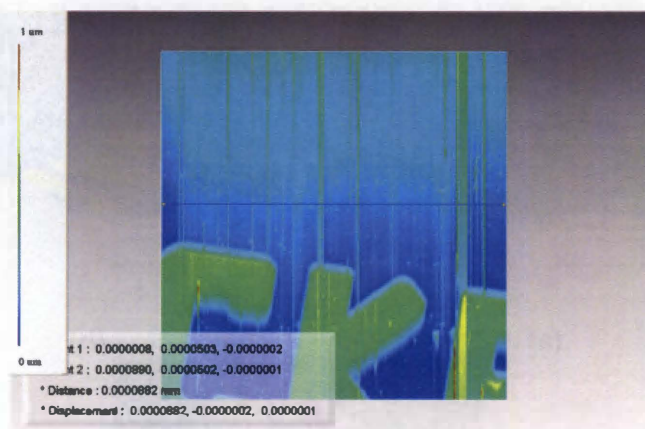
---



**Figure 4.2:** AFM range data converted to VRML file with faces applied and visualized in Rapidform®. Measurements are in meters.

---





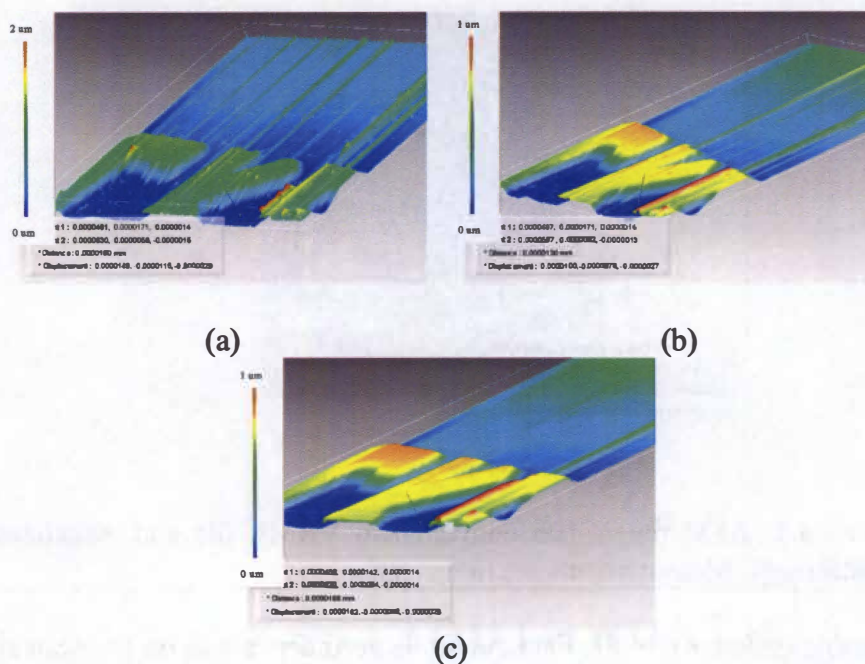
**Figure 4.3:** AFM range data converted to VRML file and visualized in Rapidform®. Measurements are in meters.

A noticeable difference in the data quality is seen depending on the scan size, and the number of data points taken. Figure 4.3 shows the amount of noise in a 3D model constructed from a scan of 90  $\mu\text{m}$  x 90  $\mu\text{m}$  performed by the AFM. Median filters were used to remove the noise. It was found that an atypical size of median filter, 10 x 2 worked well for the vertical-line type noise seen in the data. Figure 4.4 shows a comparison of a zoomed in portion of Figure 4.3, versus the same section de-noised using a 3x3 and 10 x 2 median filter.

Figure 4.5 shows a scan of a sub-set of the area shown in Figure 4.3. This scan's dimensions were 20  $\mu\text{m}$  x 20  $\mu\text{m}$ , still sampled at 256 x 256. No filtering is applied to the data. The images in Figure 4.5 show a decrease in the streakiness and vertical line type noise, which is consistent with the slower scanning speed used. The spikes seen in Figure 4.5 are more due to the hammer strike vibrations from near-by construction than noise inherent in the AFM system.

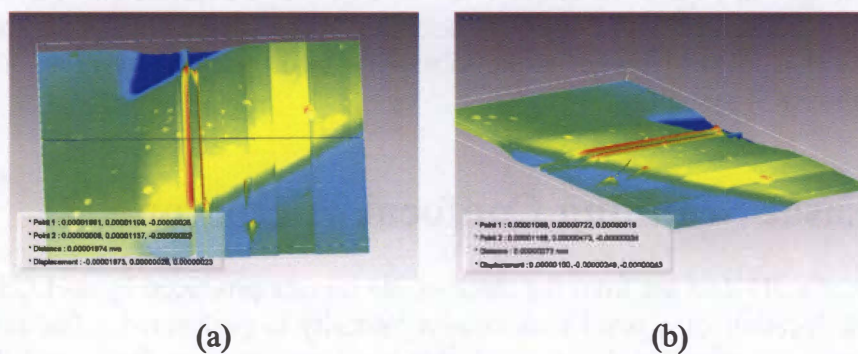
## 4.2 Laser Scanning Confocal Microscope

To reconstruct a 3D data set from the stack of 2D images produced by an LCSM, a search for the stack location of a pixel's maximum intensity is performed. The stack location found indicates the stage height at which that pixel was most in focus, and therefore the depth information for the pixel location. The scaled height can be found by taking into account the step by which the stage adjusts between slices. At its default setting, the Leica confocal microscope takes slices at steps of 0.3663  $\mu\text{m}$ .



**Figure 4.4:** De-noised AFM data. (a) 90 um x 90 um scan, (b) 90um x 90 um scan filtered with 3 x 3 median filter, (c) 90um x 90 um scan filtered with 10 x 2 median filter. Measurements are in meters.

---



**Figure 4.5:** AFM range data converted to VRML file and visualized in Rapidform®. Measurements in meters.

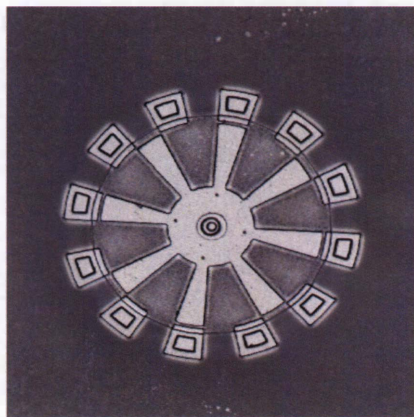
---

The algorithm then can be described as such:

- 1) Determine the pixel size of one slice image in  $x$  and  $y$  direction,  $s_x$  and  $s_y$ , respectively. Create matrix of this size to store height information for each point  $(x,y)$ .
- 2) Loop through each pixel location  $(x,y)$ .
- 3) At each  $(x,y)$ , look through stack for which slice has maximum intensity at point  $(x,y)$ .
- 4) Multiply slice number, found in step 3, by step height to get correctly scaled height. Store scaled height in matrix created in step 1.

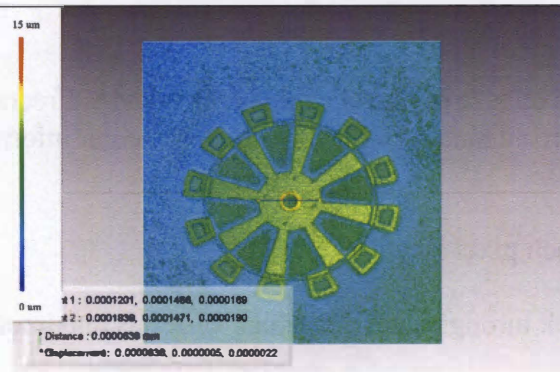
The matrix generated and filled with height values can be viewed as a range image. Figure 4.6 shows an example range image.

As with the AFM, the height calculated for each pixel along with its location, is converted into a VRML file for visualization using RapidForm®. Figure 4.7 shows the 3D model created from converting the range image in Figure 4.6 to VRML. All measurements are in meters.

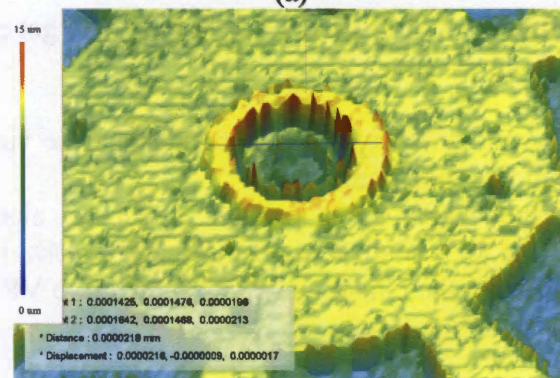


**Figure 4.6:** Confocal range image created where each pixel's height is based on the stack location where that pixel's intensity was highest.

---



(a)



(b)

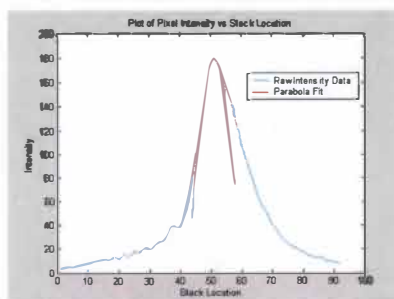
**Figure 4.7:** 3D model created by converting the confocal range image to VRML and visualizing in RapidForm®. Measurements are in meters.

Niederost et al. note that the process of assigning heights based on the positioning of the stage leads to a discretization of the assigned heights to specific levels (Niederost, Niederost, & Scucky, 2002). In an attempt to produce accuracy of a microscope lower than the step height, a quadratic curve is fitted to the intensities at stack locations surrounding the maximum intensity. The location of the maximum of this fitted curve falls in between the optical slices. Figure 4.8 shows the plot of intensities versus stack location with a parabola fitted to points surrounding, and including the maximum of the original curve.

Figure 4.9 shows a model created by fitting curves to the intensity values and extracting a new maximum. It is obvious when comparing Figure 4.9(a) and Figure 4.9(b) that the fitting process produces a much smoother model. Experiments on ground truth specimens in Chapter 6 show that the accuracy is improved as well.

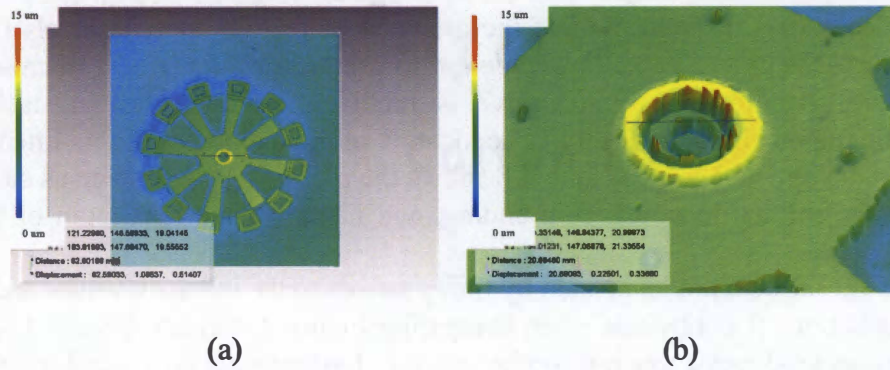
### 4.3 Scanning Electron Microscope

In scanning electron microscopes (SEM's) the most common method of 3D reconstruction is depth from stereo. Depth from stereo is found by measuring the parallax movement a point makes from its location in one image, to its location in the tilted image. Most methods generate a digital elevation map (DEM) from these parallax measurements by using equations first introduced by Piazzesi in (Piazzesi, 1973). Besides the displacement of a point, there are three other things that are needed to be known to find the 3D coordinates of the point in space: (a) the working distance of the microscope, (b) the magnification setting, and (c) the tilt angle.



**Figure 4.8:** Plot of parabola fitting to raw intensity vs. stack location data.

---



**Figure 4.9:** 3D model created curve-fitting method of determining the height. Measurements are in microns.

A representation of the SEM coordinate space is shown in Figure 4.10. The point,  $P$ , is a point on a specimen in 3D space. The image seen would have  $P$  projected onto the  $z=0$  plane. The coordinates of  $P$ , in polar coordinates, are given by equations (21)-(23).

$$\xi = a \quad (21)$$

$$\eta = R \cos \phi \quad (22)$$

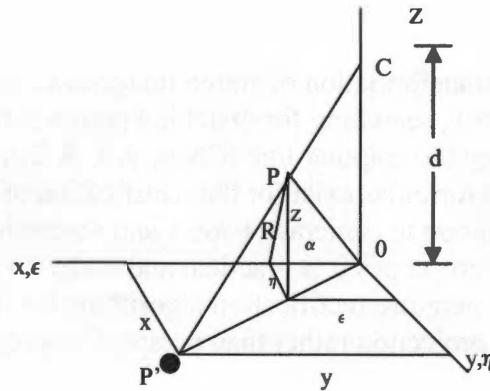
$$z = R \sin \phi \quad (23)$$

The coordinates of  $P'$ , projected onto plane  $z=0$  with planar coordinates,  $(x,y)$  are found using equations (24)-(25).

$$x = \frac{a}{1 - \left(\frac{R}{d}\right) \sin \phi} \quad (24)$$

$$y = \frac{R \cos \phi}{1 - \left(\frac{R}{d}\right) \sin \phi} \quad (25)$$

Piazzesi developed equations to determine how a point,  $P$ , would be projected differently under different tilt angles. The height,  $z$ , determines the amount of movement seen when projected onto plane  $z=0$ .



**Figure 4.10:** Representation of SEM coordinate space adapted from (Piazzesi, 1972).

The working distance for a point would be different based on the tilting, but if considered as equal, not an uncommon assumption, and in situations where the working distance,  $d$ , of the microscope is sufficiently larger than the object being examined, the height can be found as:

$$z \approx \frac{1}{M} \frac{Y_1 - Y_2}{2 \sin(\Delta\phi)} \quad (26)$$

Where  $Y_1$  and  $Y_2$  are the y-axis coordinates of the point before and after tilting, and  $M$  is the magnification factor.

In (Hemmler & Schubert, 1997), equation (27) is used based on the assumption that the SEM imaging process can be modeled as a parallel projection:

$$z = \frac{\frac{x_i - x_{i+1}}{\sin \beta} - x_i * \tan \frac{\beta}{2}}{M_x} \quad (27)$$

In equation (27),  $x_i$  and  $x_{i+1}$ , correspond to  $Y_1$  and  $Y_2$ , they represent the matched points between tilted SEM images.  $\beta$  is the tilt angle between SEM images.  $M_x$  is the scaling factor of the SEM images, i.e., the physical size in meters of each pixel.

### 4.3.1 Rectification

Rectification refers to the transformation of stereo image pairs so that their epipolar lines are aligned, and subsequently, searching for matching points is reduced from a 2-D search to a 1-D search along the epipolar line (Chen, Wu, & Tsui, 2003).

Several algorithms and formulas exist for the rectification of stereo pairs using perspective projection common to cameras. Papers and research has shown that when using scanning electron microscopes it is practical and understood that parallel projection is an appropriate model. Therefore rectification algorithms for the SEM need to work on the assumption of parallel projection rather than perspective projection (Hemmler & Schubert, 1997).

#### 4.3.1.1 Corner Detection and Matching

Corner detection was used for rectification because generally corners contain a rich amount of gradient information, and therefore give a matching algorithm the highest likelihood of finding a correct match.

The Harris corner detector detects corners and points of interest within an image. The matrix  $A$  is formed using the image gradient,  $(F_x, F_y)$  as shown. Sums of image gradients are taken over a neighborhood  $Q$  surrounding an image point  $p$ .

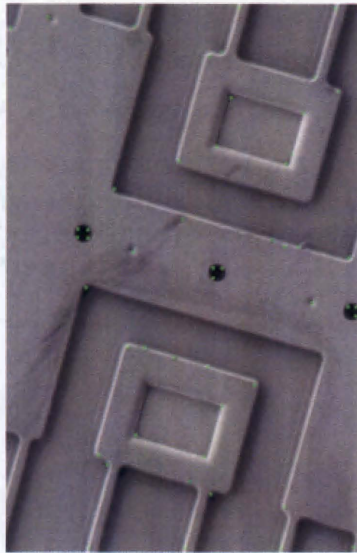
$$A = \begin{pmatrix} \sum F_x^2 & \sum F_x F_y \\ \sum F_x F_y & \sum F_y^2 \end{pmatrix}$$

The corner detection algorithm proceeds as follows:

- (1) Compute image gradient along x and y-axis ( $F_x, F_y$ )
- (2) For each image point  $p$ 
  - a. Form the matrix  $A$  for a neighborhood  $Q$
  - b. Find  $\lambda$ , the smallest eigenvalue
  - c. If  $\lambda > \sigma$ , save point  $p$  in list,  $c$ , of detected corners ( $\sigma$  is a user-defined threshold)
- (3) Sort list  $c$  in decreasing order
- (4) Scan list from top to bottom, locating first point  $p$  belonging to current neighborhood  $Q$ . Remove subsequent points occurring further down the list and also belonging to neighborhood  $Q$ .

A sample result using the Harris corner detector is shown in Figure 4.11. Corner detection is performed on each stereo image. Taking the location of corners in one image as features to be matched, matching is done by locating corners detected in the other image that are within a certain distance threshold, generally less than 6 pixels distant





**Figure 4.11:** Corner detection result on SEM image. Corners are marked as green points.

along both the x and y axis, and then doing a small cross-correlation template search around the corner to refine the corner to corner match.

#### 4.3.1.2 Epipolar Line Calculation and Image Transformation

Morgan et al. 2004 used equation (28) to represent the epipolar line in parallel projection, with homologue points  $(x,y)$  and  $(x',y')$  (Morgan, Kim, Jeong, & Habib, 2004).

$$G_1x + G_2y + G_3x' + G_4y' = 1 \quad (28)$$

The parameters  $G_1$ - $G_4$  can be solved with four matching points found through the corner matching described in the previous section. After these parameters are found the images can be transformed so the epipolar lines lie on image columns. The description of this algorithm is given Morgan et al. 2004. The transformations performed on each image's coordinates  $(x,y)$  and  $(x',y')$  are shown in equations (29)-(30).

$$\begin{bmatrix} x_n \\ y_n \end{bmatrix} = \frac{1}{S} \begin{bmatrix} \cos(\theta) & \sin(\theta) \\ -\sin(\theta) & \cos(\theta) \end{bmatrix} \begin{bmatrix} x \\ y \end{bmatrix} + \begin{bmatrix} 0 \\ -\frac{\Delta y}{2} \end{bmatrix} \quad (29)$$

$$\begin{bmatrix} x'_n \\ y'_n \end{bmatrix} = S \begin{bmatrix} \cos(\theta') & \sin(\theta') \\ -\sin(\theta') & \cos(\theta') \end{bmatrix} \begin{bmatrix} x' \\ y' \end{bmatrix} + \begin{bmatrix} 0 \\ \frac{\Delta y}{2} \end{bmatrix} \quad (30)$$

Where,  $(x_n, y_n)$  and  $(x'_n, y'_n)$  are the transformed coordinates of  $(x, y)$  and  $(x', y')$  respectively. The transformation parameters can be solved for by eliminating the y-parallax, equating  $y'_n$  and  $y_n$ , and solving equations (31)-(34).

$$\theta = \arctan\left(-\frac{G_1}{G_2}\right) \quad (31)$$

$$\theta' = \arctan\left(-\frac{G_3}{G_4}\right) \quad (32)$$

$$S = \sqrt{-\frac{G_3 \sin(\theta)}{G_1 \sin(\theta')}} \quad (33)$$

$$\Delta y = -\frac{S \cdot \cos(\theta')}{G_4} \quad (34)$$

The algorithm for rectification and epipolar alignment is as follows:

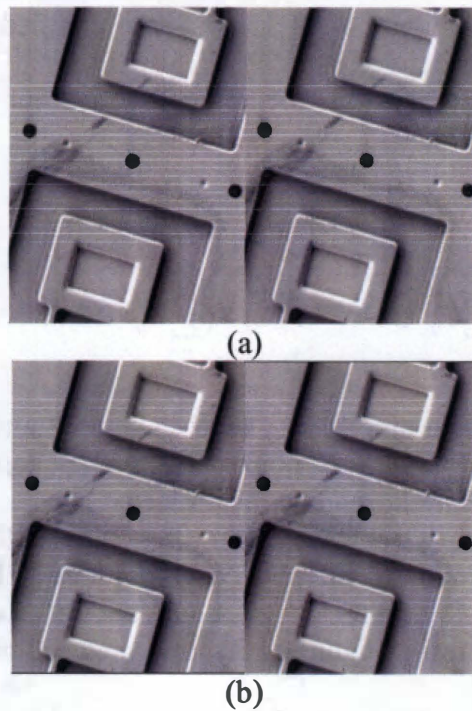
1. Detect corners and interesting points
2. Match corners and points found in 1
3. Solve for G by solving a system of equations of the form shown in equation (28)
4. Using G, solve for the parameters in equations (31)-(34)
5. Transform image coordinate points according to equations (29)-(30).

A sample result is shown in Figure 4.12. Figure 4.12a shows the horizontal lines drawn across the original unrectified stereo pair, and the result of the rectification is shown in 4.12b.

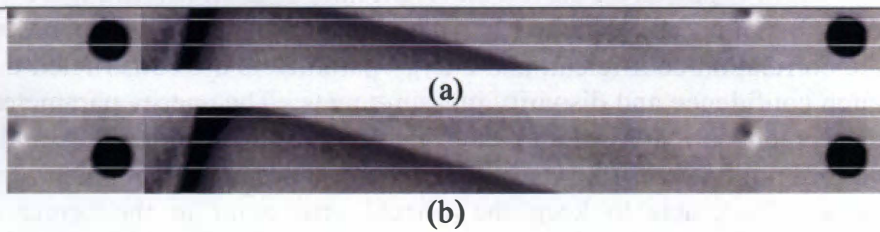
Enlarged strips taken from Figure 4.12 and shown in Figure 4.13 better illustrate the improvement between the unrectified and rectified images.

### 4.3.2 Sparse Matching

After two images are rectified, matching is done along the edges of both images. A point  $i_j$  from Image 1 is chosen such that  $i_j$  belongs to a detected edge in Image 1.



**Figure 4.12:** SEM stereo images with horizontal lines drawn over to illustrate epipolar alignment. (a) Unrectified images, (b) rectified images.



**Figure 4.13:** Enlarged strips from Figure 4.12a and 4.12b. (a) Strip from Figure 4.12a. Notice the displacement of the horizontal line through the circular element. (b) Strip from Fig. 4.12b. Notice now that the horizontal line intersects the circular element at the same point in each image of the pair.

---

The homologue point,  $i_2$ , is searched for in Image 2 along the epipolar line that passes through both  $i_1$  and  $i_2$ . Figure 4.14 shows two rectified stereo images and their corresponding edge images derived using the Canny filter.

The matching criterion used is the mutual correlation coefficient as shown in Equation (35).

$$R_c = \frac{\sum_{ij} T_{ij} * S_{ij} - N \bar{T} * \bar{S}}{\sqrt{(\sum_{ij} T_{ij}^2 - N * \bar{T}^2) * (\sum_{ij} S_{ij}^2 - N * \bar{S}^2)}} \quad (35)$$

Where  $T_{ij}$  and  $S_{ij}$  are a single pixel's grey level value in the template and current search area respectively,  $N$  is the number of points in the template, and  $T$  and  $S$  represent the mean of the template and current search area respectively.

A tentative  $i_2$  is found by searching along the epipolar line for the highest  $R_c$ , and determining that this maximum  $R_c$  lies above a certain threshold, usually between 0.8 and the maximum value of 1. Once a tentative  $i_2$  point is found, a reverse matching algorithm checks if  $i_2$  matches back to  $i_1$ . Figure 4.15 shows matched points between Image 1 and Image 2 colored in green.

A VRML file was created from the 3D point cloud and visualized in Rapidform® as shown in Figure 4.16.

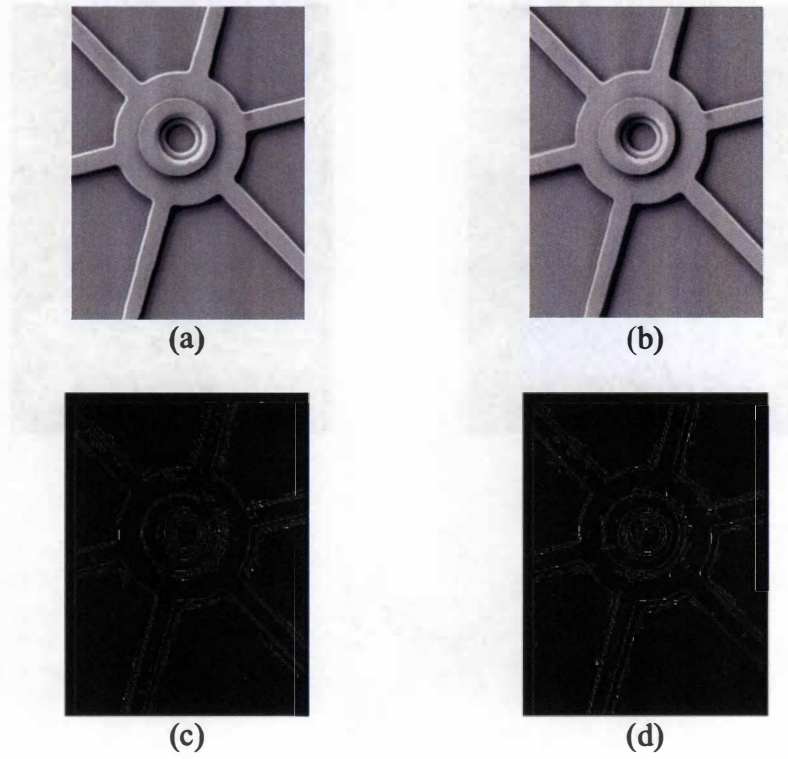
### 4.3.3 Dense Elevation Map Generation

Standard cross-correlation matching and energy minimization methods were used to generate a 3D model from SEM stereo. An energy minimization algorithm was chosen as a method for generating a dense disparity map that gave depth even at textureless points. First, a grid is placed on the left and right images as shown in Figure 4.17.

Second, grid points are matched between images using template based matching based on the correlation coefficient, and energy parameters are constructed that take into account match confidence and disparity measurements. The energy parameters constrain the grid's movement so that a smooth, and realistic surface is created. A pulling energy,  $E_{ext}$ , pulls a grid point away from its original position based on the match results, and an internal energy,  $E_{int}$ , acts to keep the current grid point in the center of the two surrounding grid points. An illustration is shown in Figure 4.18. Point  $X'$  is being matched at point  $X''$ .

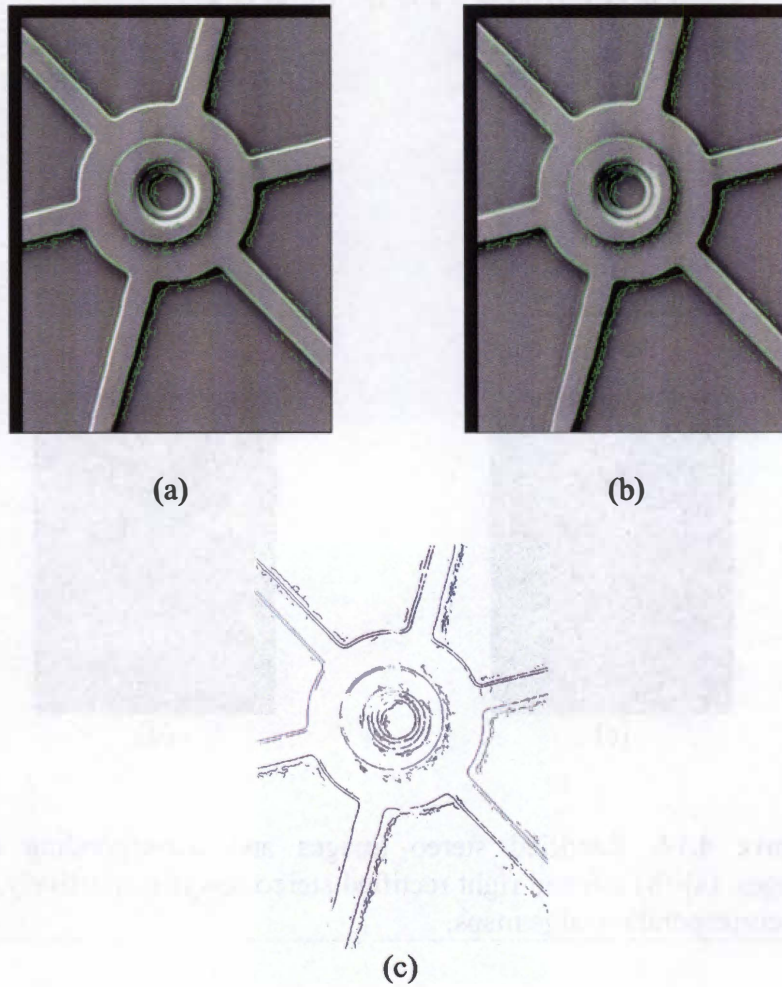
The cost function used to determine the best match is expressed by equation (36)

$$E = \alpha \times E_{ext} - \beta \times E_{int} \quad (36)$$



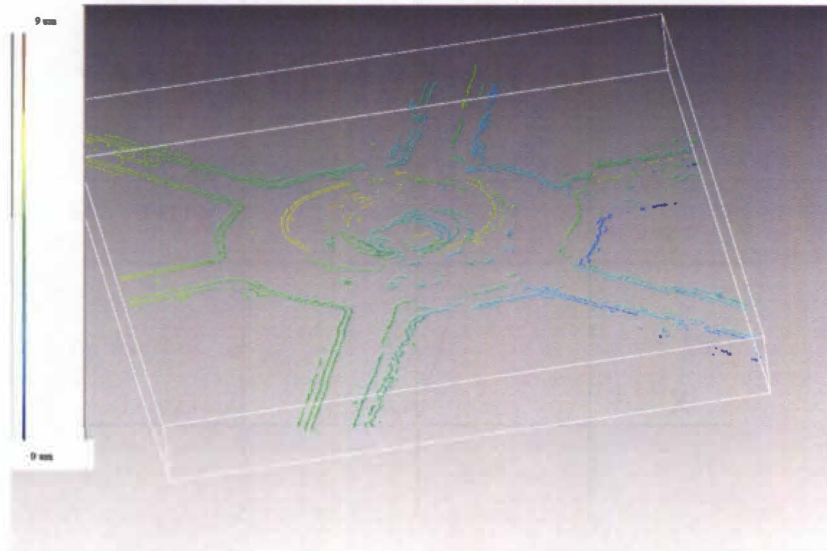
**Figure 4.14:** Rectified stereo images and corresponding edge images. (a)-(b) left and right rectified stereo image respectively, (c)-(d) corresponding edge maps.

---



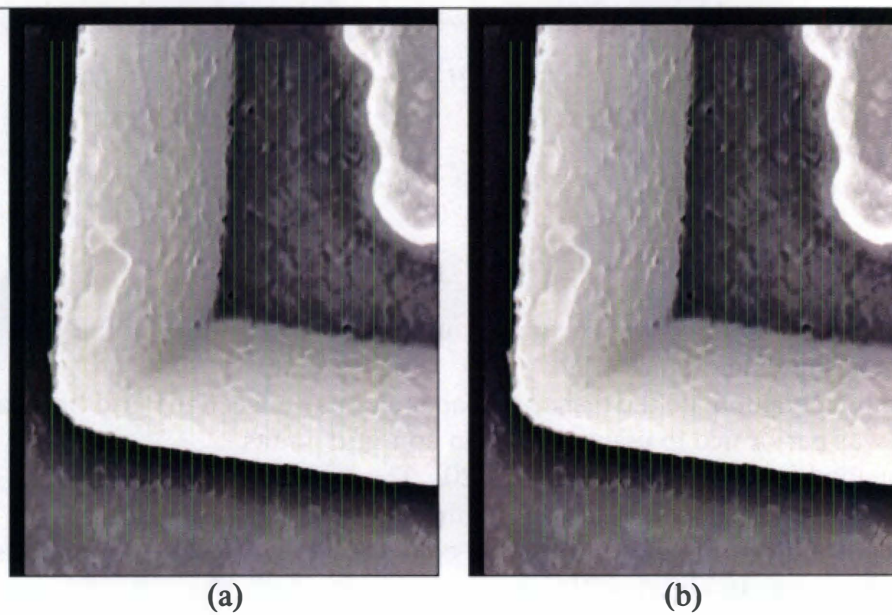
**Figure 4.15:** Sparsely matched points from SEM stereo. (a) and (b) matched points of left and right image respectively, (c) disparity map created.

---



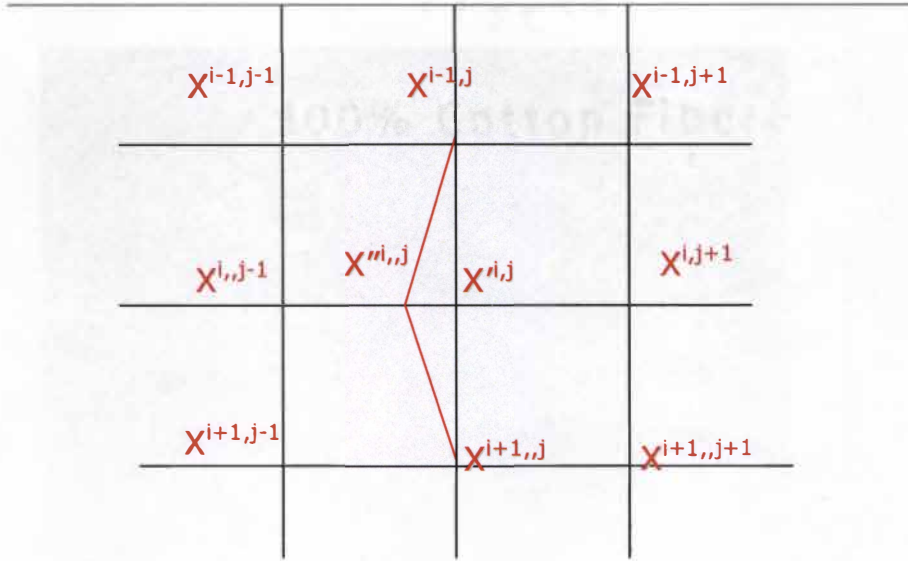
**Figure 4.16:** 3D point cloud model from matched points shown in Figure 4.15.

---



**Figure 4.17:** Grid lines layed over left, (a) and right, (b) stereo images.

---



**Figure 4.18:** Illustration of the grid matching algorithm.

Where,

$$E_{ext} = \frac{\sum_{i=1..k, j=1..l} (I_L(i, j) - \bar{I}_L(i, j)) \times (I_R(i, j) - \bar{I}_R(i, j))}{\sqrt{\sum_{i=1..k, j=1..l} (I_L(i, j) - \bar{I}_L(i, j))^2 \times \sum_{k=1..k, j=1..l} (I_R(i, j) - \bar{I}_R(i, j))^2}} \quad (37)$$

$$E_{int} = \frac{2 \times |X''_{i,j} - X'_{i,j}|}{(X_{i,j+1} - X_{i,j-1})} \quad (38)$$

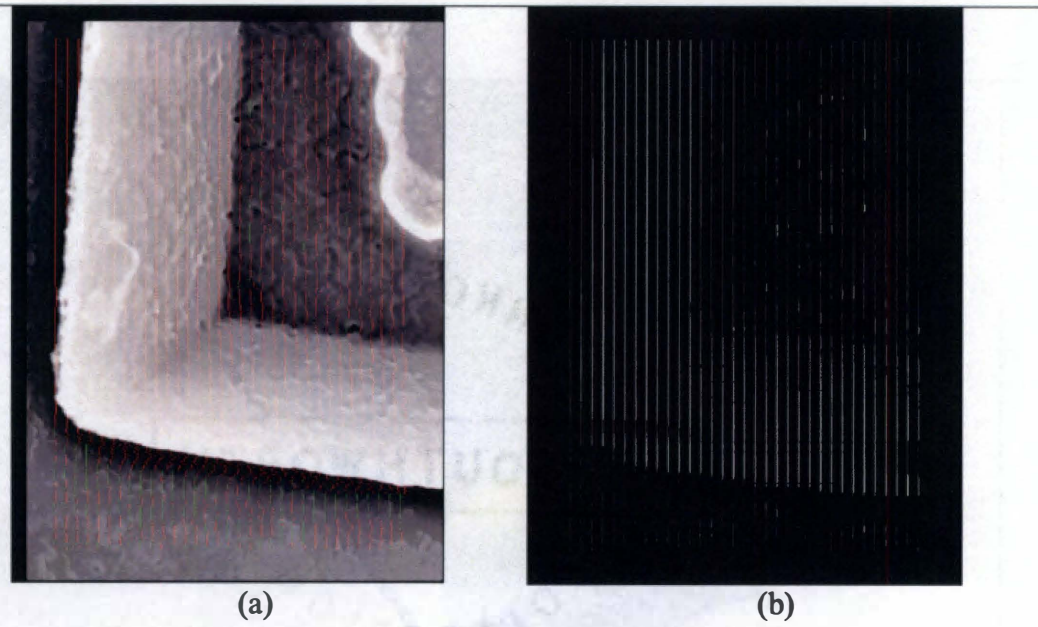
This algorithm applied to the images in Figure 4.17 produces the grid result and disparity map shown in Figure 4.19.

To completely populate the disparity map at points between the grid lines, an averaging was performed to assign values to non-grid points.

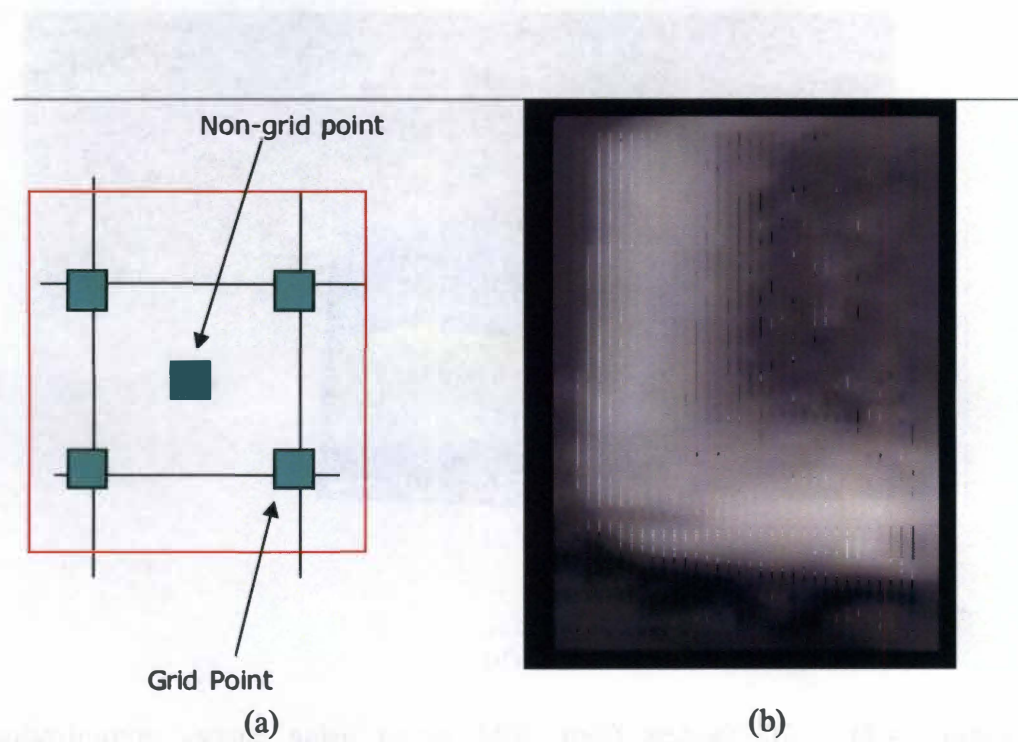
This method is illustrated in Figure 4.20. The non-grid point is set to the average of the surrounding grid points that fall within the designated window size.

The depth map in Figure 4.20(b) was converted to a VRML file, and visualized in Rapidform® as seen in Figure 4.21.

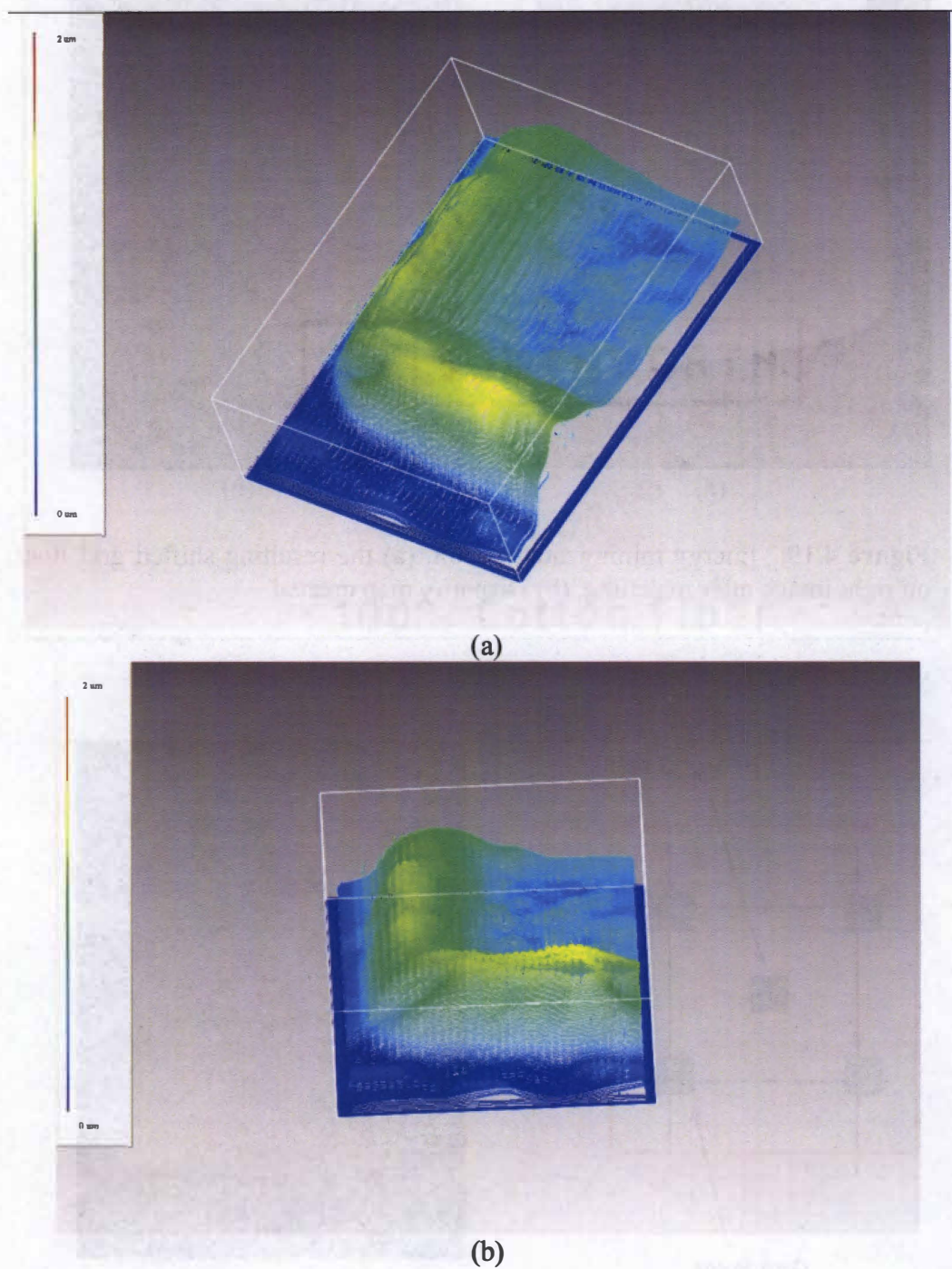




**Figure 4.19:** Energy minimization result. (a) the resulting shifted grid lines on right image after matching, (b) Disparity map created.



**Figure 4.20:** Interpolating between grid points. (a) interpolation scheme, (b) Resulting depth map.



**Figure 4.21:** 3D models from SEM stereo using energy minimization matching without grid refinement. (a) and (b) show two different views of the same model.

### 4.3.3.1 Grid Refinement

As an improvement to the energy minimization algorithm discussed in the previous section, a coarse to fine matching procedure was implemented. In the first step a grid with spacing between points of 16 pixels is used for matching. Figure 4.22 shows two stereo images with a sparse point grid before and after matching.

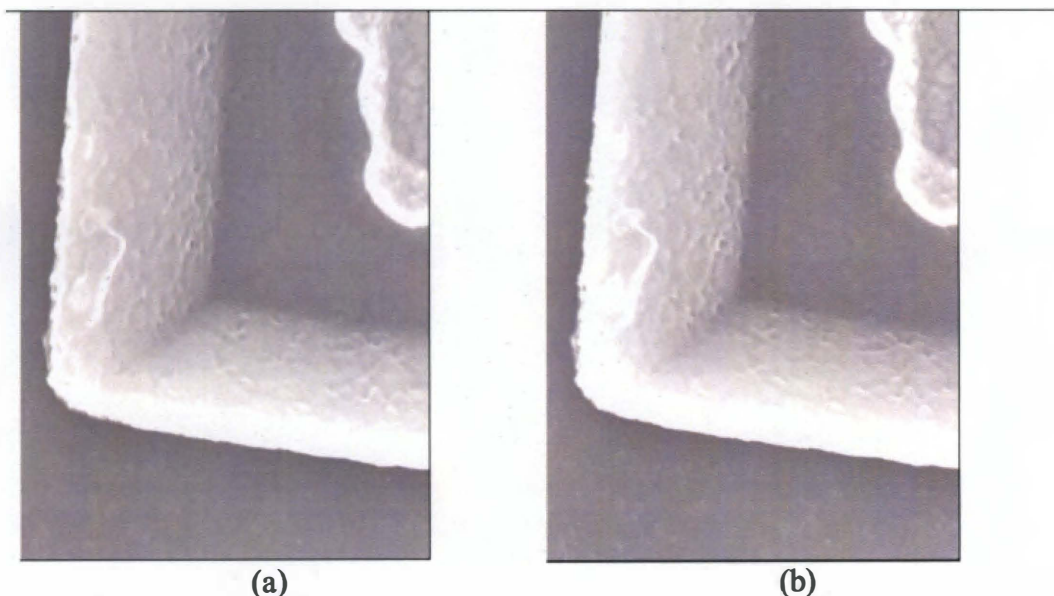
In subsequent steps the grid spacing is halved and grid points are added in the center of the previously matched points. In Figure 4.23's example, three grid points (a,b,c) have been matched, and are shifted left from their initial starting points. When the grid is refined, new points are added at the center point between the shifted locations.

These new points are then matched, and another set of grid points is placed in the center of those. This process goes on until the spacing is one pixel or until a user specified stopping point is reached. Figure 4.24 illustrates the process of grid refinement.

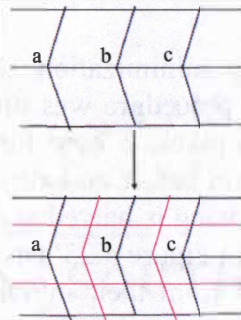
Figure 4.25 shows the result visualized in Rapidform®.

### 4.3.3.2 Cross-Correlation Area Based Matching

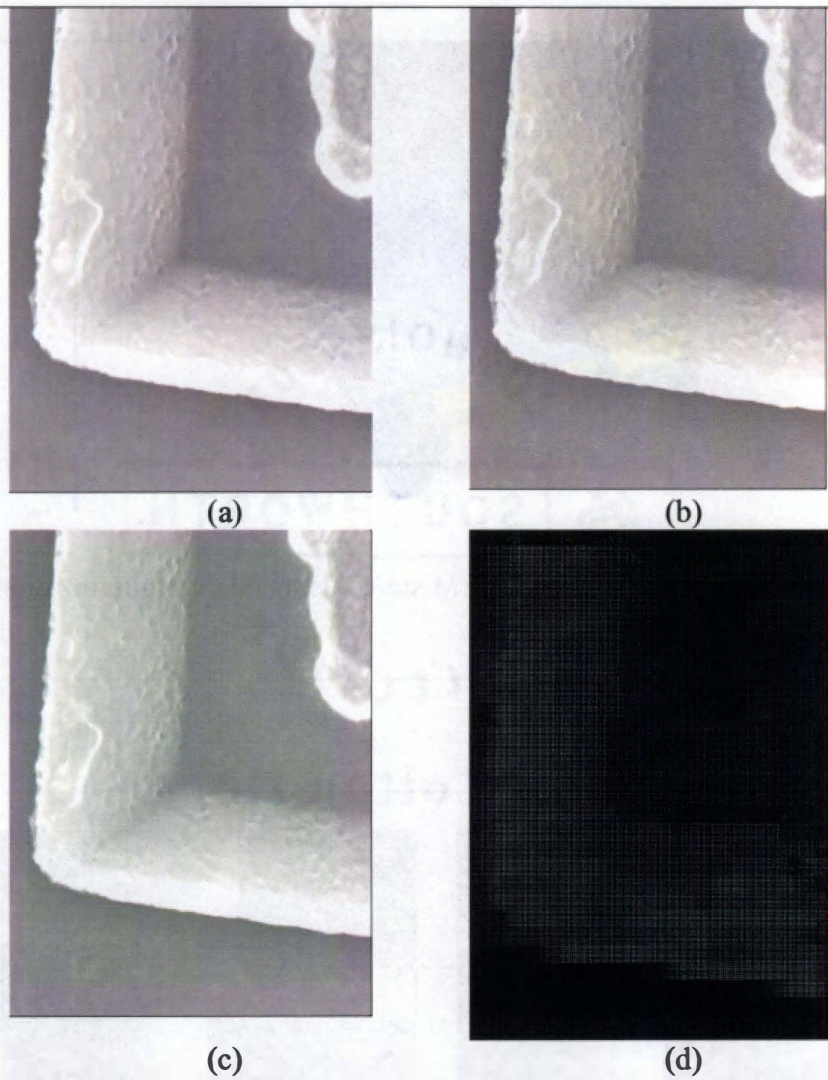
In area-based matching, a template around a point  $P$ , is moved over each point of a larger window area,  $W$ , in the second image. A criterion such as the normalized cross-correlation coefficient is computed between the template and each subsection of the search area,  $W$ , centered at a point  $P'$ . The maximum criterion value corresponds to a match between point  $P$  and  $P'$ . Figure 4.26 illustrates this search method. Since the stereo images in this project have been rectified, the search window is only moved horizontally along the epipolar line.



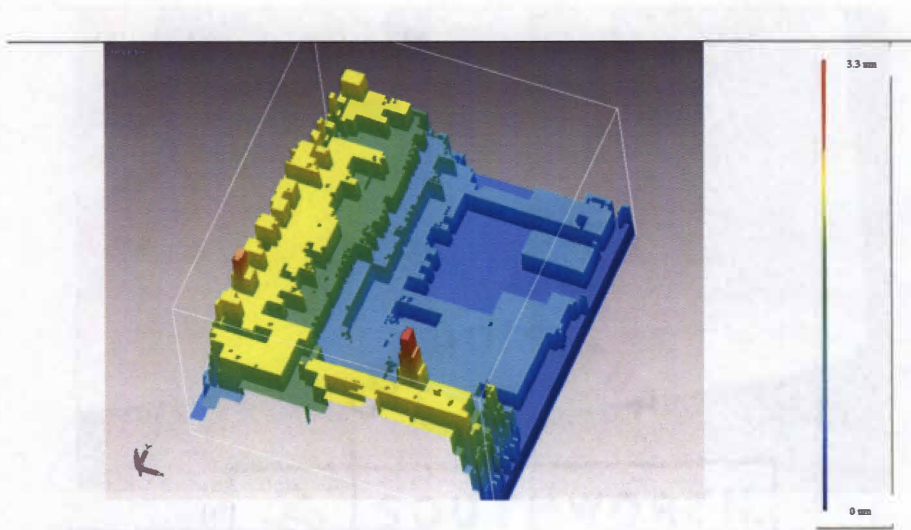
**Figure 4.22:** Matching on two stereo images with sparse grid. (a) left image with green grid points, (b) right image with matched points now red.



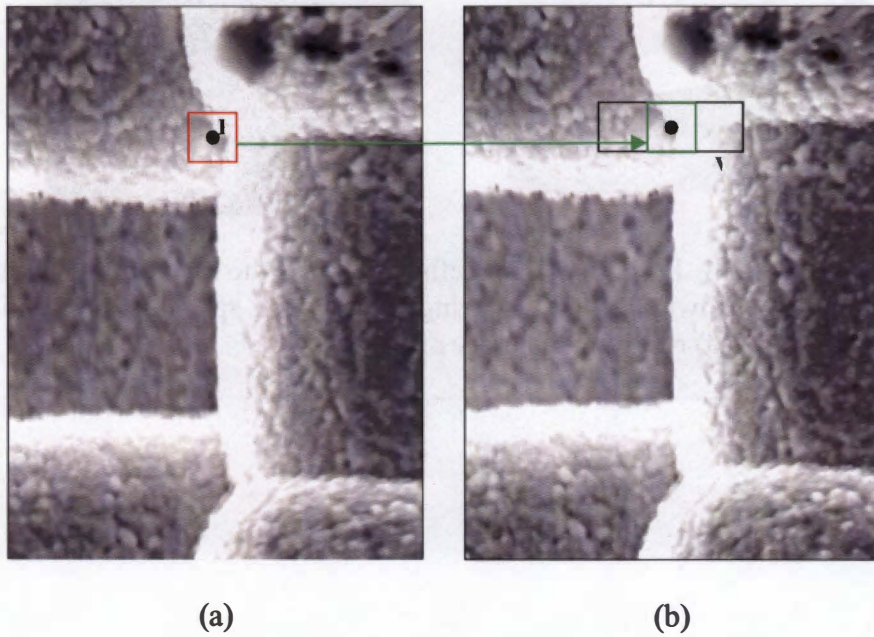
**Figure 4.23:** Illustration of grid refinement. New grid lines indicated by pink lines.



**Figure 4.24:** Process of grid refinement and the resulting disparity map are shown. (a) grid spacing 8, (b) grid spacing 4, (c) grid spacing 2, (d) resulting disparity map.



**Figure 4.25:** 3D model with SEM stereo using energy minimization matching methods.



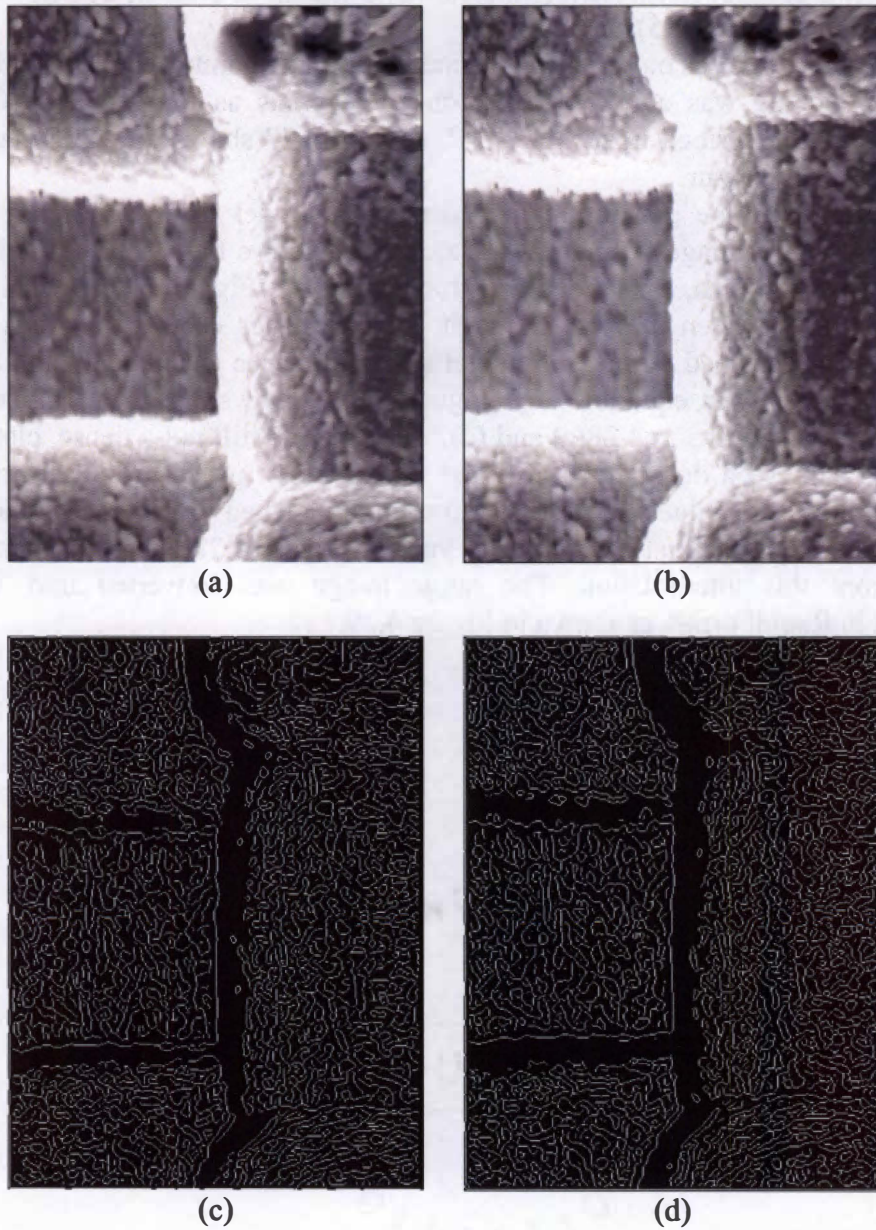
**Figure 4.26:** Searching for matching points between two images. The red square template window in (a), is searched for in the black rectangle in (b), by computing the mutual correlation coefficient between the green square in (b) and the red square in (a).

Minoshima et al. (2000) present a method of template matching using the mutual correlation coefficient (MCC) between two locations, as the measure of how good a match the two locations represent (Minoshima, Suezaki, & Komai, 2000). This measure was defined in equation (35).

We used the MCC as our criterion to find homologue points between SEM stereo pair images. Matching was attempted only on edge points as found by the Canny edge detector, and as described in section 4.3.2. Figure 4.27 shows the edge maps obtained from an SEM stereo pair.

In Figure 4.28, the generation of a dense 3D model from SEM stereo is shown through a series of images. Figure 4.28(a) and (b) shows the stereo pair from which a sub-area, shaded green, will be reconstructed in 3D. Figure 4.28(c) and (d) shows matched points between the left and right stereo images colored in green. Using the disparity of the matched points, the height at each pixel is calculated using the formula from Hemmleb's paper, equation (27). Figure 4.28(e) shows the elevation map generated from the matched points in 4.28(c) and (d). This map is still not a dense, closed surface. In order to achieve a dense disparity map, interpolation needs to be performed on the unmatched areas. A value was assigned to each unmatched pixel equal to the median of the closest three points that had disparity values. Figure 4.28(f) shows the range image created from this interpolation. The range image was converted into VRML and visualized in RapidForm® as shown in Figure 4.29.

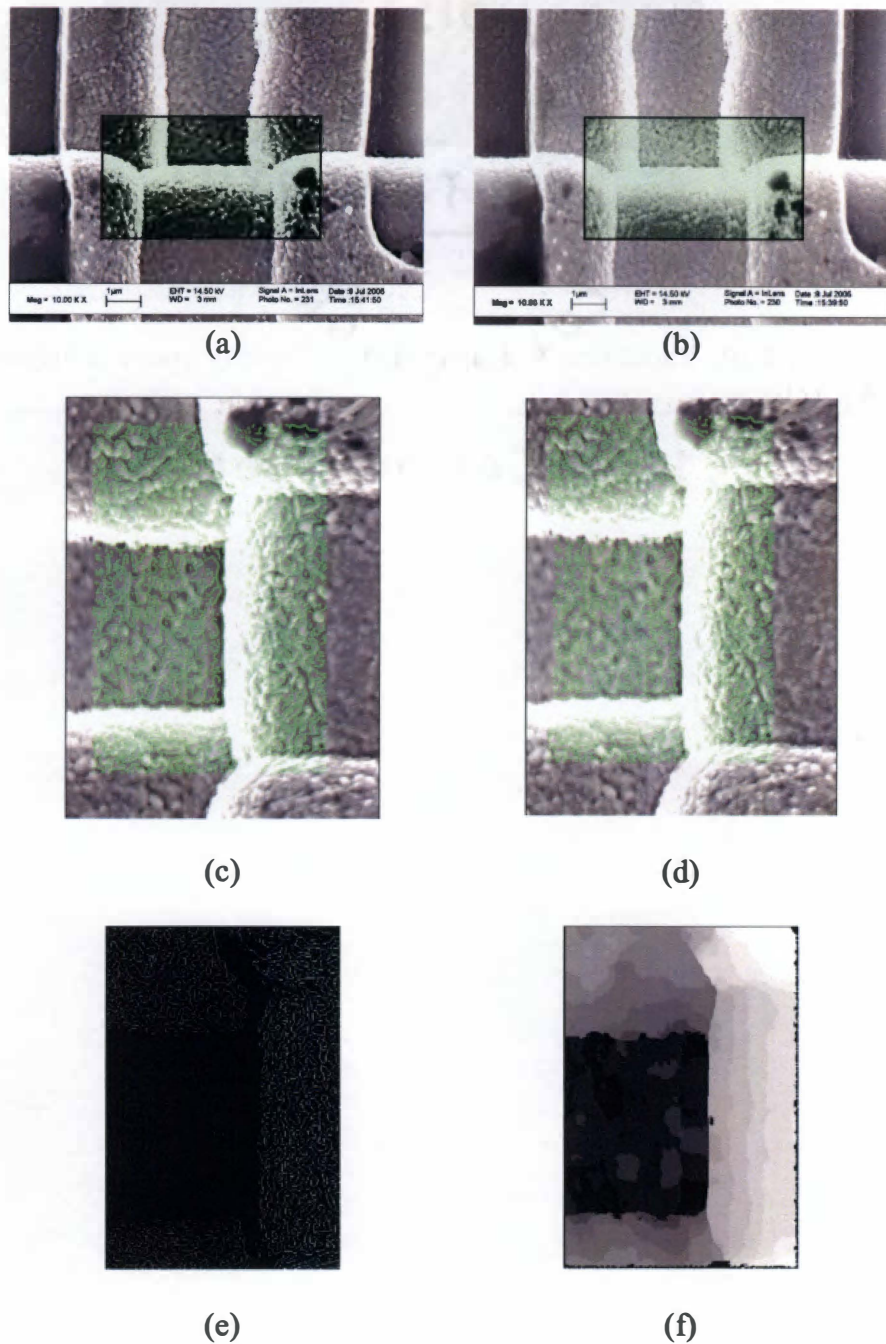




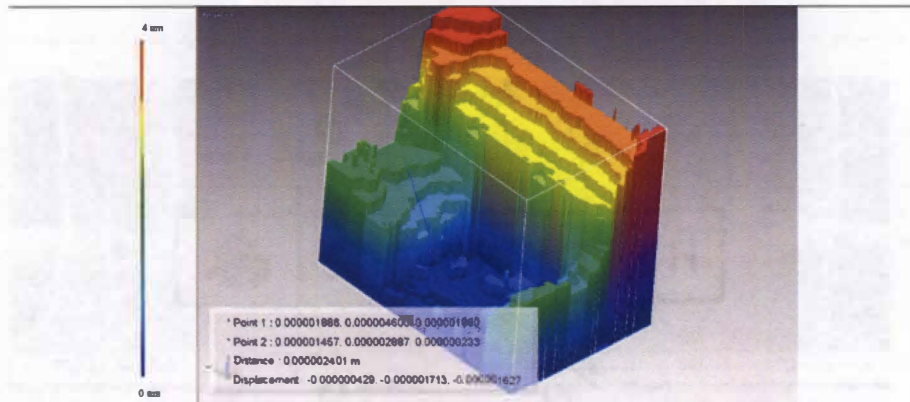
**Figure 4.27:** Rectified stereo images and corresponding edge images. (a)-(b) left and right rectified stereo image respectively, (c)-(d) corresponding edge maps.

---





**Figure 4.28:** Generation of dense elevation map from SEM stereo. (a) and (b) SEM stereo pair with tilts of  $0.5^\circ$  and  $3^\circ$  respectively,, (c) and (d) matches on left and right stereo image respectively, (e) sparse disparity map, (f) dense disparity map from interpolation.



**Figure 4.29:** Rapidform® visualization of disparity image in Figure 4.27(e).

## 5 Model Registration

In the past, sacrificing field-of-view for higher magnification was an unavoidable trade-off in microscopy. Mosaicing algorithms have overcome this problem, allowing microscopists to stitch several high-magnification views into a single image that not only gives local detail, but also the larger context in which that local detail occurs. Similarly in our 3D reconstructions, we would like to build large 3D models that cover a wide area of the specimen, but at the same time have the accuracy only possible at high magnifications. Two methods for this would be, registering reconstructed models in 3D space, or registering the disparity/range images in 2D. Since these models are 2½D, it was decided to do the registration in 2D using the range images.

### 5.1 Orientation Correlation

Orientation correlation registers images that have a translation shift, without any rotation (Fitch, Kadyrov, Christmas, & Kittler, 2002). In our data acquisition scenario, the specimens are moved with the stage, only in the x or y direction, and is never rotated. Fitch et al. show orientation correlation to be fast, exhaustive, statistically robust, and illumination invariant. To perform orientation correlation, the orientation images must be derived from the two images on which registration is to be done, and these images matched by maximizing the correlation between them. An orientation image,  $f_d$ , of an image,  $f$ , can be formed according to equation (39).

$$f_d(x, y) = \text{sgn}(\partial f(x, y) / \partial x + i \partial f(x, y) / \partial y) \quad (39)$$

The orientation images are matched using correlation. Given the FFT of  $f_d(x, y)$ ,  $F_d(k, l)$ , and the FFT of  $g_d(x, y)$ ,  $G_d(k, l)$ , the registration of  $f_d$  and  $g_d$  is found by locating the maximum of equation (40).

$$\Re\{IFFT(F_D(k,l)G^*_D(k,l))\} \quad (40)$$

This algorithm was applied to data from each of the three microscopes: the AFM, LCSM, and SEM, results are given in the following sections.

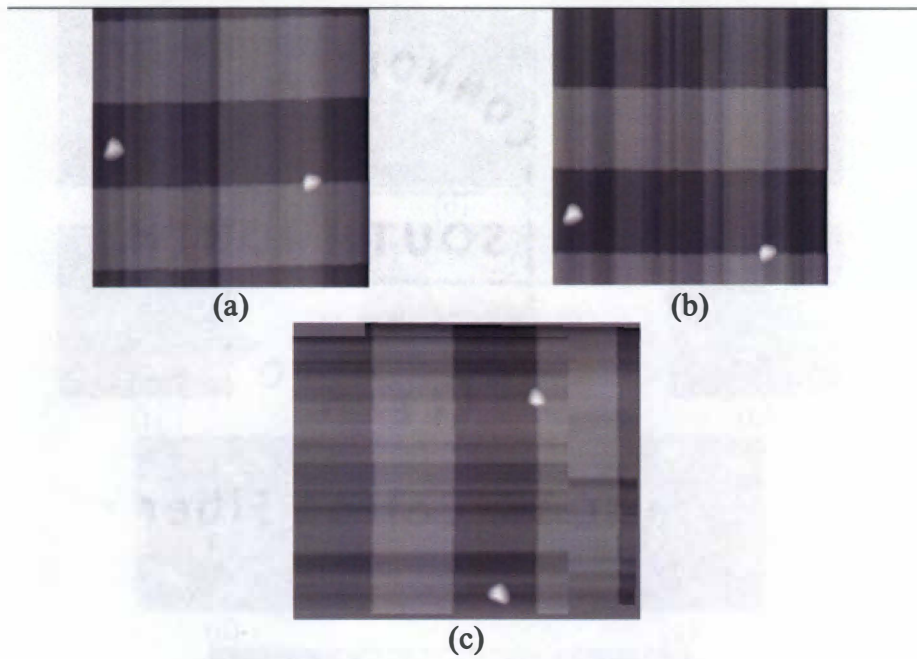
## 5.2 Registration of 3D Range Data

AFM data was acquired for the purpose of registration by changing the center point of the AFM scan. After one scan, the X-Y offset for the probe head is changed and the scanning commences over another area. AFM data of the TGZ01 series was registered using the orientation correlation algorithm described in Section 5.1. Figure 5.1 shows the results. The registered result was visualized in Rapidform and is shown in Figure 5.2.

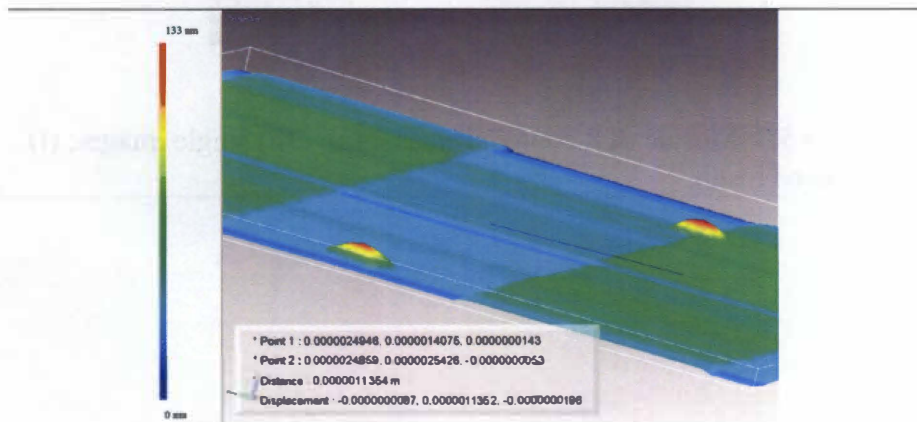
To acquire LCSM data for registration, a series of image stacks were acquired for overlapping areas. A range image was generated for each of these image stacks. Figure 5.3(a)-(h) shows the series of range images and the registration result in (i).

Figure 5.4 shows the 3D model generated from Figure 5.3(i) and visualized in Rapidform®.

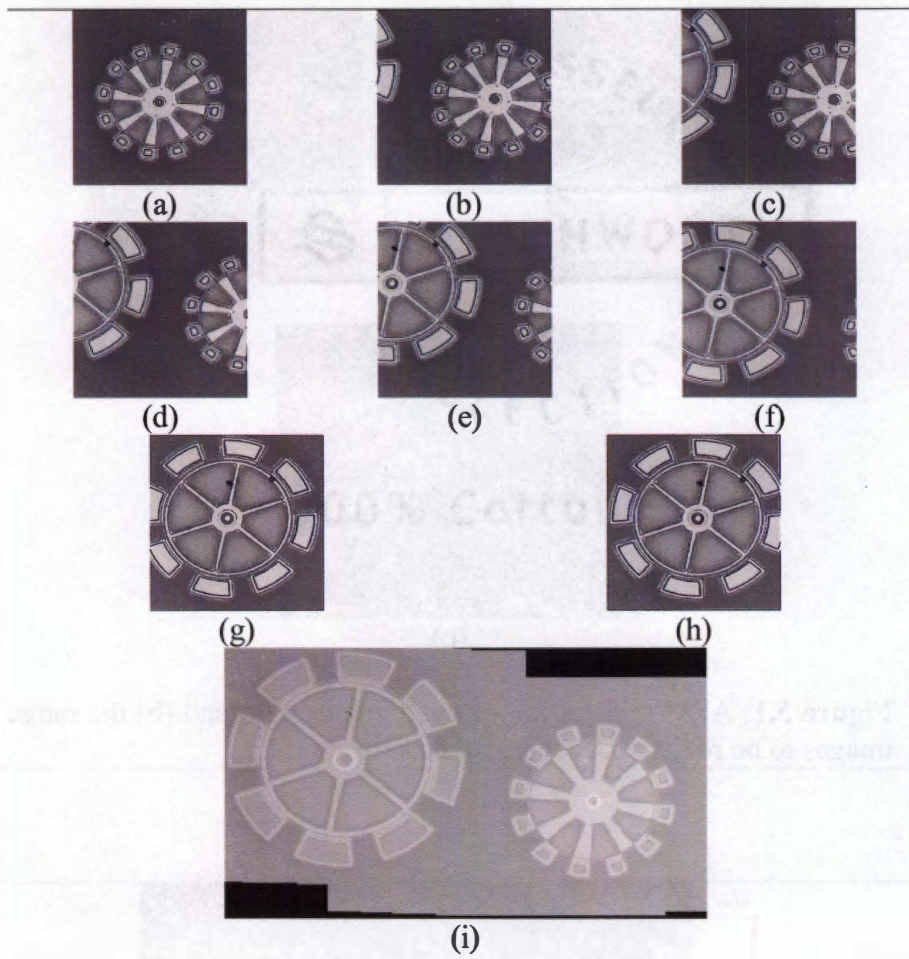
For model registration with the SEM, two stereo pairs from neighboring regions were acquired. Figure 5.5 shows two sets of stereo pairs. Figure 5.6 (a) and (b) show the reconstructed range images from the sets of stereo pairs in Figure 5.5(a-b) and Figure 5.5(c-d) respectively. These images show a difference in intensity due to the different center points of the stereo pairs; all heights in a single stereo reconstruction are relative to the center point and therefore two scans of similar areas with different center points will differ in the absolute heights calculated. Before registration, we subtracted from Figure 5.6(b) a constant value equal to the height difference of a single point between the two range images. Figure 5.6(c) shows the registration result obtained by orientation correlation. The mosaic in Figure 5.6(c) still shows a difference in intensity between the registered areas. This difference in the range images is most likely due to the different tilt angles used in the separate stereo pairs, and future work will investigate this effect. Figure 5.6(d) shows the 3D model in Rapidform®.



**Figure 5.1:** AFM registration of range images. (a) and (b) the range images to be registered, (c) registration result.

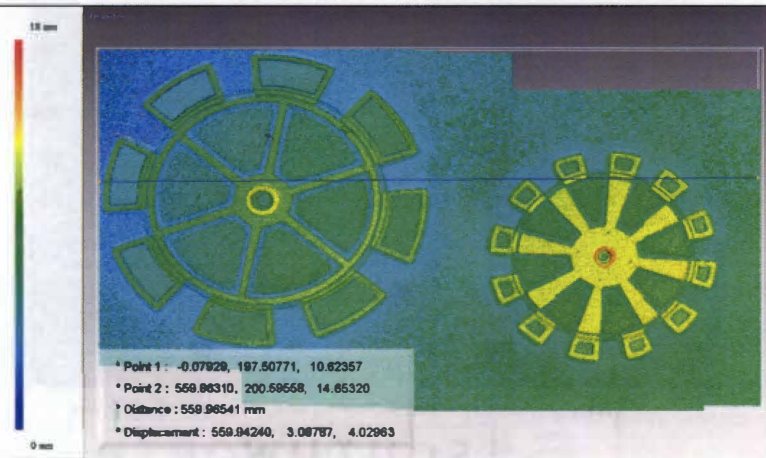


**Figure 5.2:** 3D model of registered images.

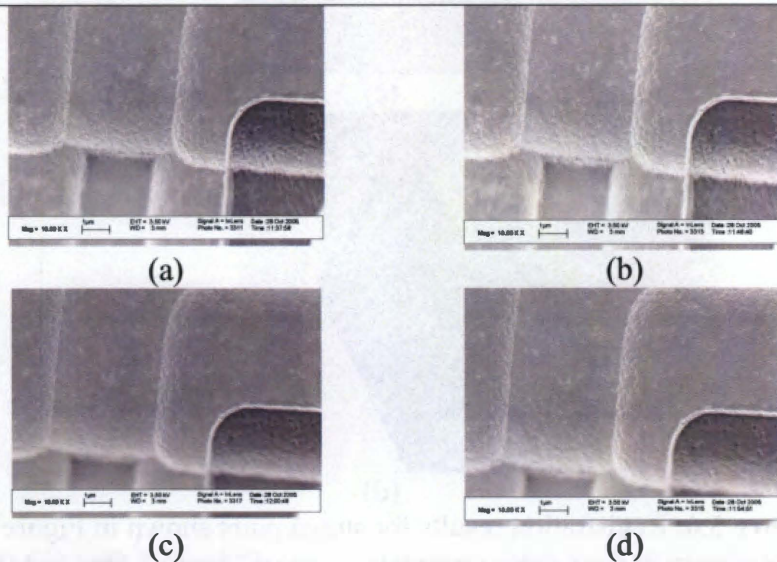


**Figure 5.3:** Mosaic of 8 confocal stacks. (a) – (h) single images, (i) mosaiced result.

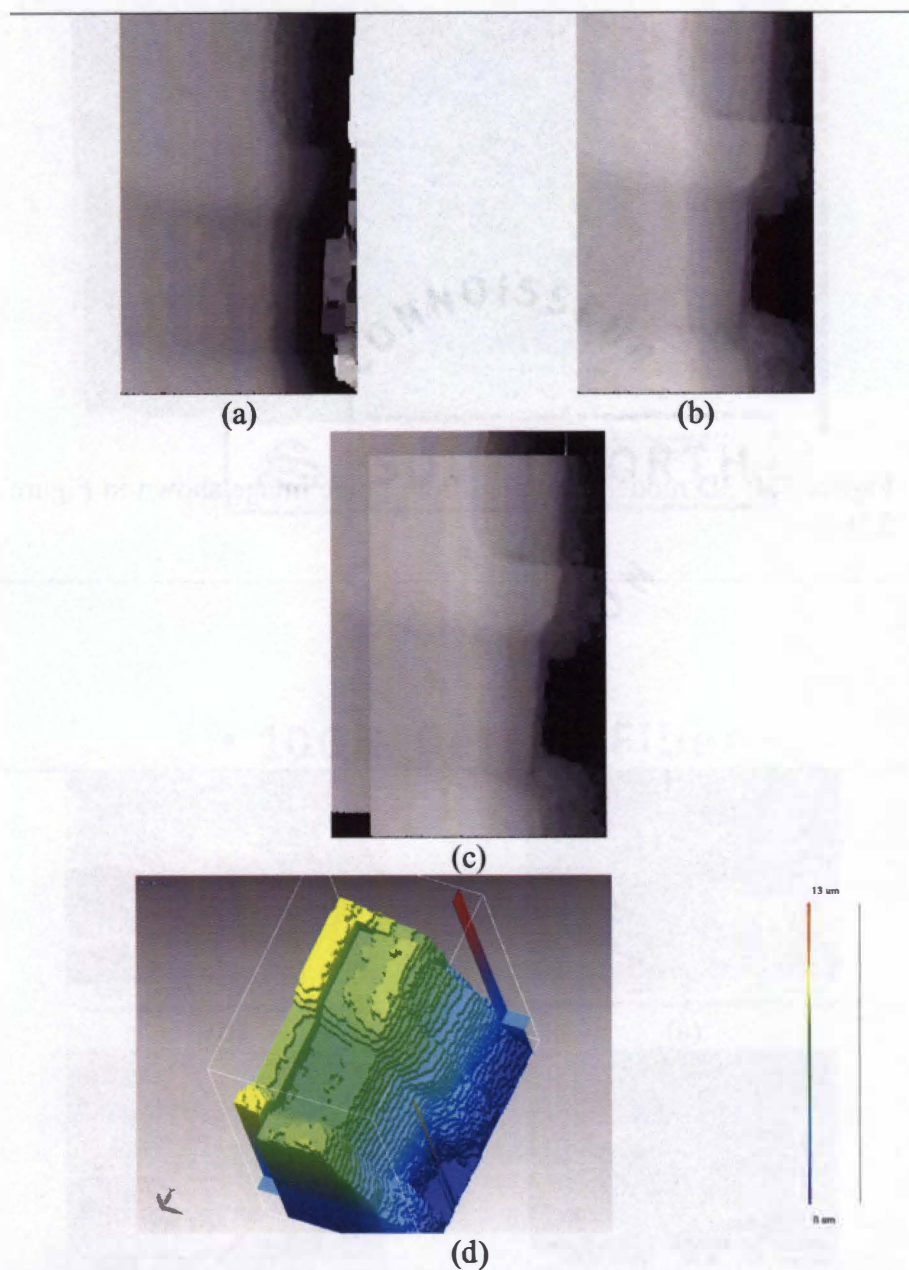
---



**Figure 5.4:** 3D model generated from range image shown in Figure 5.3(i).



**Figure 5.5:** Stereo pairs from overlapping areas. (a) and (b) are one stereo pair tilted at  $4^\circ$  and  $6.5^\circ$  respectively. (c) and (d) are the second stereo pair tilted at  $3^\circ$  and  $5.5^\circ$  respectively.



**Figure 5.6:** Registration results for stereo pairs shown in Figure 5.5. (a) Range map from stereo reconstruction of Figure 5.5(a) and (b), (b) Range map from stereo reconstruction of Figure 5.5(c) and (d), (c) Registration of (a) and (b), (d) 3D model visualization of (c) in Rapidform ®.



## 6 Comparison of Results

In this section 3D reconstructions from three microscopes: the SEM, LCSM, and AFM, are compared in terms of their field of view and accurate representation of surface topology. Images of a MEMS device, along with several calibration gratings, were used to determine strengths and weaknesses of each microscope and reconstruction algorithm.

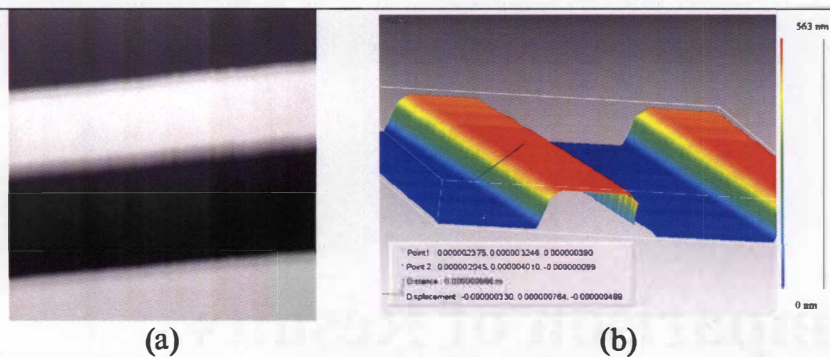
### 6.1 Ground Truth

Several calibration gratings, with certified heights of 500 nm, 100nm , and 18 nm, were reconstructed to verify the accuracy of the 3D microscopy methods discussed in the previous section. Section 3.1 gives details on the calibration gratings.

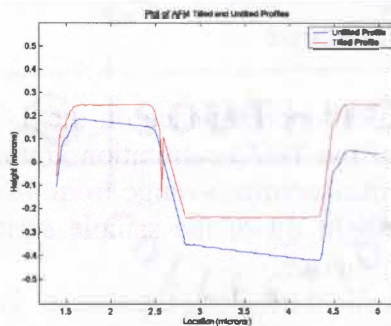
#### 6.1.1 Atomic Force Microscope

First, we will examine the AFM's performance on the TGZ height step series. Figure 6.1a shows the range image of the TGZ3 calibration grating; Figure 6.1b shows the 3D reconstructed model. Height measurements range from 488 to 595 nm. The variation in measurements is due to the slight tilt of the sample surface, and to the AFM tip not making direct contact with the surface.

The AFM data exhibited a slight tilt along the x-axis. This was corrected by calculating the slope between two points that were known to lie on a flat plane, for example the center point of the two raised steps. A rotation angle was calculated from this slope and the range data was corrected to 'flatten' the AFM data. Figure 6.2 shows a comparison of two height profiles, one from the original untilted AFM data, and one after the tilt was corrected.



**Figure 6.1:** Collected AFM data for TGZ3. (a) Range image, (b) 3D reconstruction showing a step height of 488 nm.



**Figure 6.2:** Graph showing original untilted AFM height profile for TGZ3 compared with tilted profile.

It would not be possible to assume this exact tilt correction should be done on all specimens, because the error is not simply due to the AFM probe mechanism, but also due to the manner of specimen placement (glue, or tape) and for each specimen a different tilt angle away from a plane will be noted. The tilt can be corrected on these calibration gratings because a reasonable assumption can be made considering the planarity between two points.

Figure 6.3 shows the AFM data collected from the TGZ02 step series. Step heights here are certified to be  $100.9 \text{ nm} \pm 1.2 \text{ nm}$ . Figure 6.4 shows height profiles taken across the untilted and tilted AFM data respectively.

Figure 6.5 shows the AFM data collected from the TGZ01 step series. Step heights here are certified to be  $18.8 \text{ nm} \pm 0.6 \text{ nm}$ . Figure 6.6 shows height profiles taken across the untilted and tilted AFM data respectively.

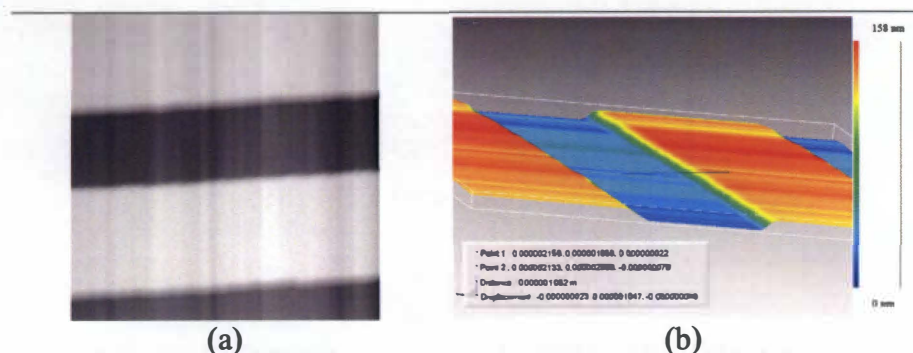
## 6.1.2 Laser Scanning Confocal Microscope

In this section, we examine the results from the LCSM. As mentioned in Section 3.3, the confocal microscope can resolve vertical features down to approximately  $0.75 \text{ } \mu\text{m}$  along the z-axis. Therefore, attempting to reconstruct these calibration gratings is truly pushing the LCSM's theoretical limits. The results would be expected to be noisy and less accurate, and that is what we saw. Figure 6.7 shows the range image and VRML reconstruction of TGZ03 from the LCSM at 10x magnification.

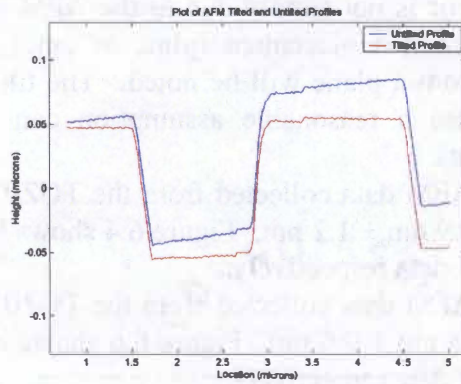
Figure 6.8 shows a comparison of height profiles from the AFM data and the LCSM data at 10x magnification.

## 6.1.3 Scanning Electron Microscope

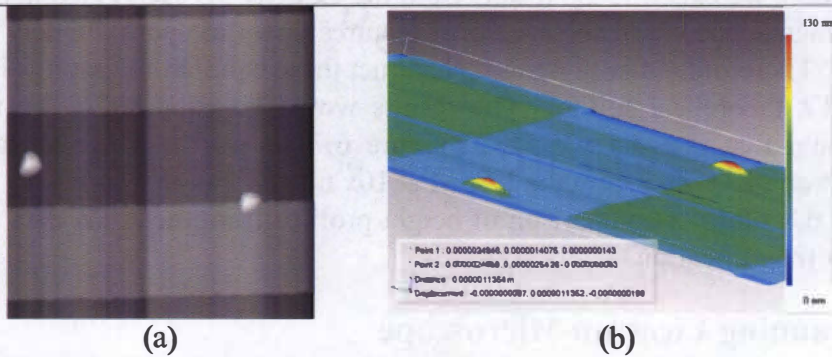
In this section, we examine the results from the SEM. Figure 6.9 shows an SEM stereo pair of the TGZ02 step height. The step heights lack distinguishable texture and the only visible features are the somewhat blurry edges. Sparse matching, using the area-based method described in section 4.3.2, allowed us to examine the accuracy of the algorithm,



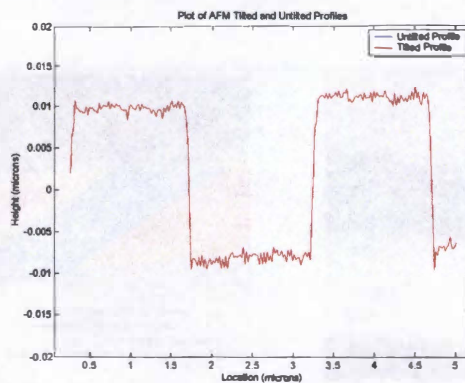
**Figure 6.3:** Collected AFM data for TGZ02. (a) Range image, (b) 3D reconstruction showing a step height of 99 nm.



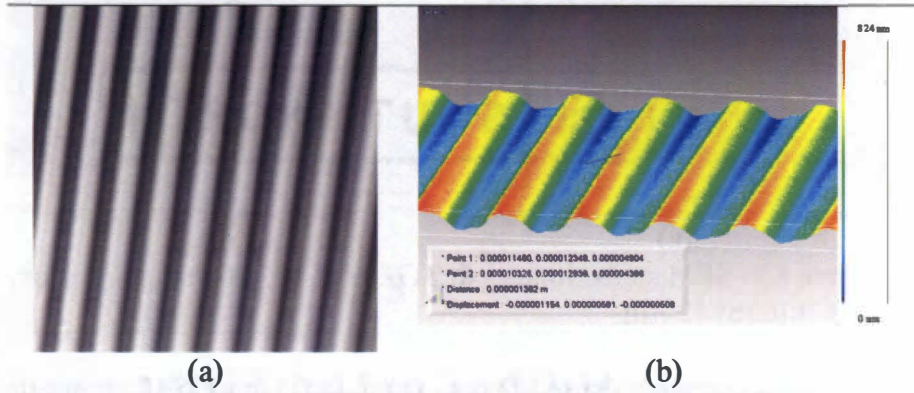
**Figure 6.4:** Graph showing original untilted AFM height profile for TGZ02 compared with tilted profile.



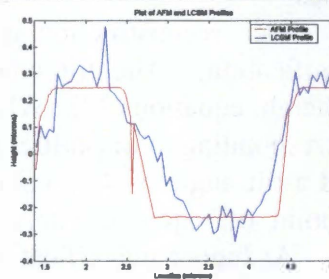
**Figure 6.5:** Collected AFM data for TGZ01. (a) Range image, (b) 3D reconstruction showing a step height of 19.6 nm.



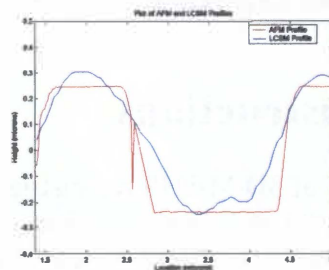
**Figure 6.6:** Graph showing original untilted AFM height profile for TGZ01 compared with tilted profile.



**Figure 6.7:** Collected LCSM data for TGZ03 at 10x. (a) Range image, (b) 3D reconstruction showing a step height of 508 nm.

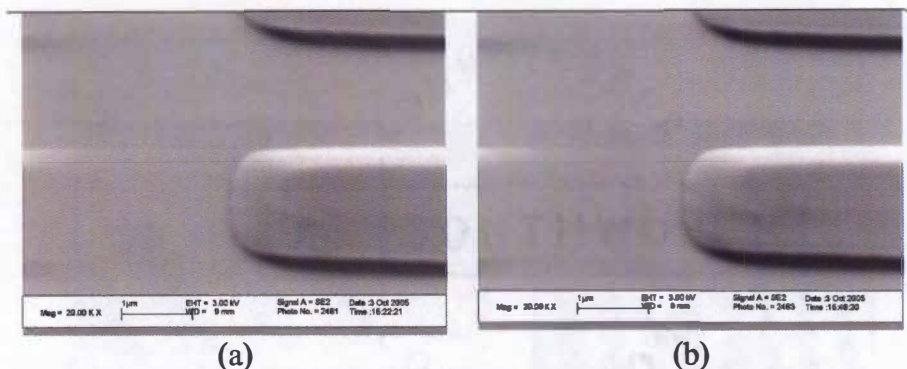


(a)



(b)

**Figure 6.8:** Comparison of AFM and LCSM height profiles for TGZ03. (a) LCSM data is unfiltered, (b) LCSM data has been filtered with 7x7 median filter.



**Figure 6.9:** SEM stereo images of TGZ02 at 20,000x magnification. (a) 8° tilt, (b) 12° tilt.

despite an inability to create a dense 3D reconstruction. Figure 6.10 shows the matching results and disparity map.

To assess the reconstruction accuracy, we looked at height profiles across the disparity map, noting the height changes. Matching was done on the edges, and so we would expect an accurate reconstruction to show a height discrepancy of 100 nm between the two edges that correspond to the bottom and top of the step height. Figure 6.11 shows two of these height profiles.

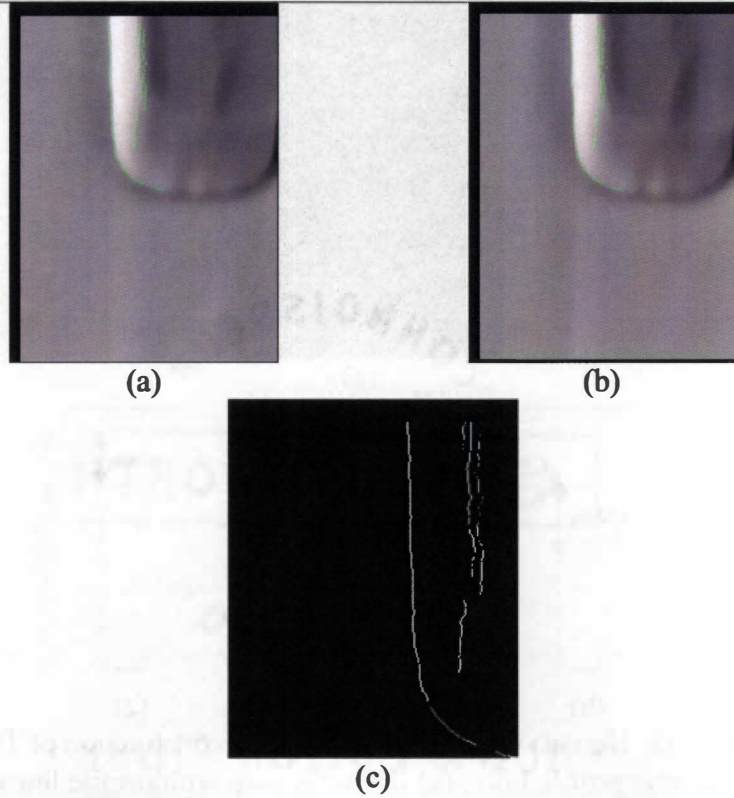
The accuracy of the SEM stereo reconstruction is based on three factors: match accuracy, tilt angle, and magnification. The tilt angle and magnification limit the accuracy based on Hemmleb's height equation (27). What we see in Figure 6.11, are two different height calculations corresponding to disparities that differ by only one pixel. At a magnification of 20,000x and a tilt angle of 4°, a shift of one pixel corresponds to a height relative to the center point of approximately 80~100 nm, depending on the distance from the center point. At higher magnifications, with samples showing good texture, much better accuracy could be approved. At 50,000x, and a tilt angle of 8°, the SEM stereo method could discriminate heights of around 15 nm.

## 6.2 MEMS Reconstructions

This section will include results of 3D MEMS reconstructions from the SEM and LCSM. AFM images are not shown for the MEMS device due to the large spread of range of height values, up to 8 μm, that made it difficult to apply enough pressure to the tip so that it touched the top and bottom, but did not break or become dull.

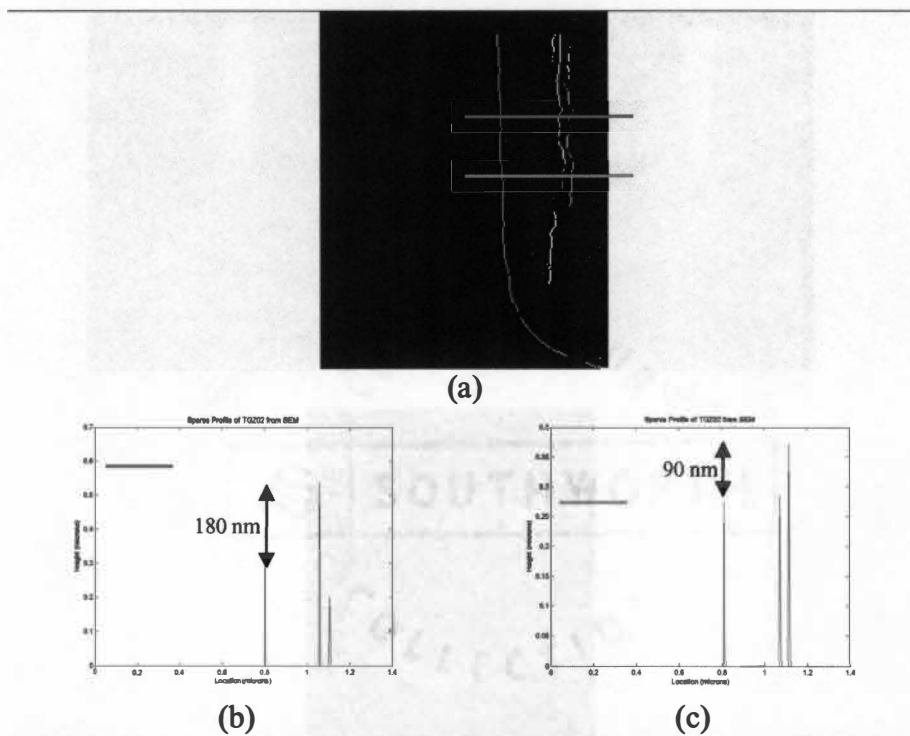
Figure 6.12 shows reconstructions of the center area of a harmonic motor. Using Rapidform®, a vertical measurement along the z-axis was taken from approximately the same areas in each the SEM and LCSM reconstructions. The measurements differ by 400 μm, a reasonable amount considering the accuracy of the LCSM versus the SEM.

Figure 6.13 shows reconstructions of a wire's connection to a contact point. Again measurements were taken, here differing on the order of 150 nm.



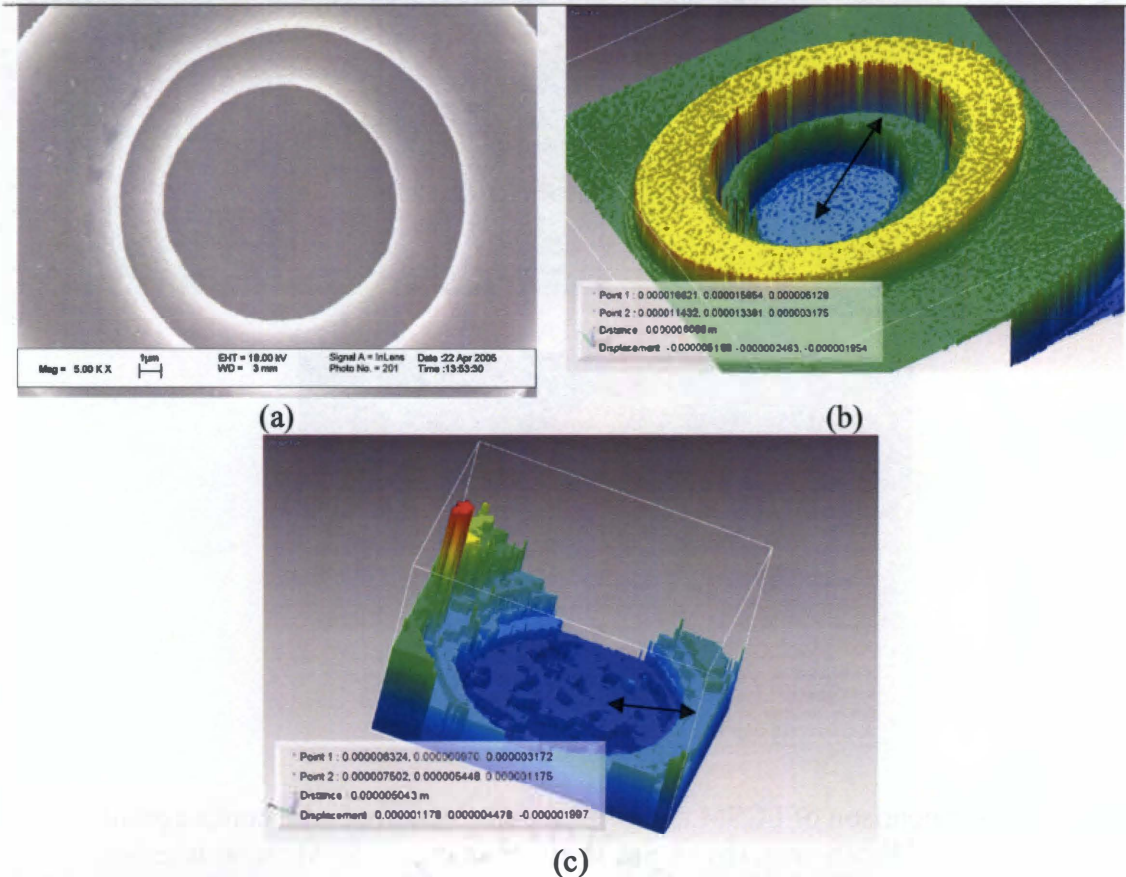
**Figure 6.10:** Matching and disparity map created for TGZ02. (a) points to match on left image, (b) matched points on right image, (c) resulting disparity map.

---

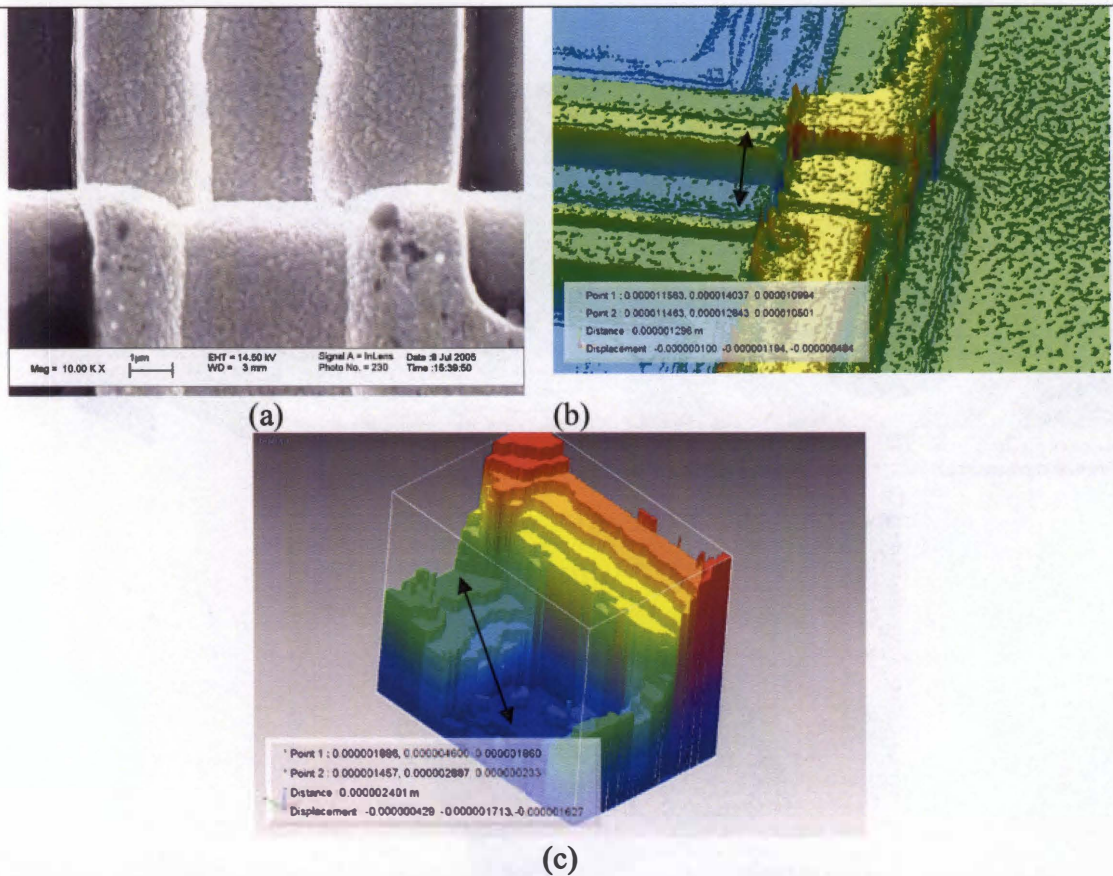


**Figure 6.11:** Heights recorded in SEM 3D reconstruction of TGZ02 along sample profile lines. (a) Disparity map with profile lines marked in red and orange, (b) Heights recorded along from red profile line, (c) Heights recorded along orange line.





**Figure 6.12:** Comparison of LCSM and SEM reconstruction of harmonic motor area. (a) SEM image of MEMS area, (b) LCSM reconstruction, (c) SEM reconstruction. Vertical distance along black line in LCSM reconstruction is 1.95 μm; vertical distance along black line in SEM reconstruction is 1.99 μm.



**Figure 6.13:** Comparison of LCSM and SEM reconstruction of wire contact point. (a) SEM image of MEMS area, (b) LCSM reconstruction, (c) SEM reconstruction. Vertical distance along black line in LCSM reconstruction is 1.75  $\mu\text{m}$ ; vertical distance along black line in SEM reconstruction is 1.6  $\mu\text{m}$ .

## 7 Conclusions

As nanotechnology progresses to smaller scales, the need increases for novel inspection schemes that can characterize nanodevices. In our work we have implemented, refined, and compared algorithms that reconstruct 3D models of nanodevices from 2D microscopy data. Microscope data collection from the AFM, LSCM, and SEM was mastered, including pre-processing the data to remove noise and aid the 3D reconstruction process. Techniques for the pre-processing included, de-noising using median filters on AFM data, contrast stretching for SEM, and curve-fitting on LCSM scans. For each microscope, a specific algorithm was implemented to generate the 3D models. Code was written to convert the median-filtered AFM data to a VRML file that could be visualized in Rapidform®. The LCSM was used to optically slice specimens along their z-axis. From these optical slices a 3D model was successfully reconstructed. Further, a contribution was made by refining this 3D model so that it was accurate beyond the optical stack resolution. For the SEM, an algorithm was implemented for rectifying stereo pairs, and two algorithms were implemented for the matching, energy minimization grid matching and mutual cross-correlation based template matching. A dense elevation map and 3D reconstruction were generated by interpolating between the matches given by the two methods. Compared to shape from shading methods, such as in Seeger (2004), stereo methods allow actual heights to be calculated across the surface, and reconstruction time is usually 5-10 minutes, compared to hours.

After 3D reconstruction, contributions were made in registering 3D models of nanodevices, and in comparing the different microscope reconstruction results. A novel registration method was applied to each microscope to register 3D data. Orientation correlation, a 2D registration algorithm, was used to mosaic 2D range maps generated by the reconstruction methods. These mosaiced range images were then visualized in 3D. By mosaicing surrounding neighborhoods, a large field of view can be examined without sacrificing high magnification. The accuracy of each microscope and accompanying reconstruction algorithms were examined using a series of calibration gratings with step heights of 500 nm, 100 nm, and 18 nm. A comparison was made between the different microscopes' accuracies, and between the microscopes' MEMS 3D reconstructions of identical areas.

Several areas for future work with the SEM include: improved matching algorithms that are robust to specimens with limited texture, experiments at higher magnifications and tilt angles to push the SEM's vertical resolution closer to the AFM, and multi-sensor fusion with the multiple modalities available on most SEM's, such as the large chamber SEM microscope at Oak Ridge Nation Labs, which is equipped with the following capabilities :

- : Backscatter detector (BSE)
- : Energy Dispersive X-ray Spectrometry (EDS)
- : Electron Backscatter Diffraction (EBSD)
- : Fourier Transform Infrared Spectrometer (FT-IR)
- : Focused Ion Beam (FIB)

The Backscatter electrons detected by the BSE are high energy electrons emitted from the specimen as a result of the electron beam. Backscatter electron emission is greatly influenced by the specimen's atomic number, and a higher atomic number relates to higher emission. Topography also influences the intensity of backscatter electron emission, and so when using the method for elemental information it is best if there is little to no surface variation.

Elemental analysis is better done with the EDS sensor or FT-IR. When the high energy electron beam moves over a surface x-rays are given off than can be detected and processed to give information concerning the elemental composition of the sample being scanned. After scanning at several different voltages, a spectrum is created with x-ray peaks representing elements present. With knowledge of the elements present a second line scan can be done with the detector looking for where specific peaks occur on the sample's surface, thereby creating an elemental map of the surface. These scans have lower resolutions than typical secondary electron images, one micron as compared to 1 nanometer.

The FT-IR sensor reads the infrared absorption characteristics of the sample, and identifies characteristics of most organic liquids, solids, and gases. The FT-IR sensor is often used in the analysis of failures in plastics, rubbers, and other materials with organic properties.

The EBSD method is used to investigate the crystallographic properties of samples. They are mostly used to detect the orientation and damage or defects present in crystalline samples.

The FIB scans sample surfaces with finely focused ion beams, and the secondary ions generated can be viewed as a microscopic image, such as secondary electrons are read in standard SEM operation. The FIB can also be used at high intensities as an etching beam. This allows etching of patterns at very high resolution. The FIB can also cut into specimens, allowing cross-sectional analysis and 3D reconstruction by cutting a sample into layers and stacking them up using image processing algorithms.




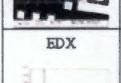


Novel and interesting uses for multi-modality work on an SEM itself, should be looked at. BSE low-voltage images show promise for stereo acquisition (Richards, Wieland, &

Textor, 2000). Elemental imaging with EDX could be used as texture on a 3D model. Figure 7.1 shows a chart of possible sensor combinations.

With the LSCM, further experiments can be done at higher magnifications that use oil or water immersion. These immersion methods present the possibility of damaging the specimen, but research into the accuracy improvements offered could decide for certain whether it was worth damaging the nanodevice by imaging in such a way. We have shown its accuracy to be in the range of 200 nm when using the refined reconstruction technique. It is beyond the LSCM's limits to approach the vertical or lateral resolution of either the SEM or AFM, but useful MEMS applications still exist for the LSCM. Future work could include an automated system that moves the stage laterally and vertically, capturing z-stacks at overlapping locations for large mosaics. This automated process could lead to large 3D reconstructions of full design layouts of MEMS devices.

Seeger's work with the fusion of SEM and AFM information is a good indicator of promising research in fusing microscopic modalities (Seeger, 2004). Future work should include further research into the use of stereo reconstruction, rather than shape from shading when fusing with the AFM.

Our work should push forward in using multi-modal registration algorithms to apply the SEM's rich textures onto the LSCM and AFM 3D models. Finally we should continue our pushing of the SEM's non-contact stereo methods to their limits in order to approach the AFM's vertical resolution of nanometers.

SENSOR	SE	BSE	EDX	FT-IR	FIB	EBSD
	Mosaic Stereo	Effective atomic number of surface elements if specimen has flat topography	Elemental Mapping	Organic compound mapping similar to EDX	Cross-section imaging 3D from slices	Automated mapping of surface phase
	Effective atomic number of surface elements if specimen has flat topography	Mosaic Stereo	Label images	Label images, map as with EDX	Cross-section imaging	Mapping of phases onto BSE
	Elemental Mapping	Label images	Possibly could do stereo, but would be lower resolution than SE stereo	Verify complementary results	Cross-section imaging of elemental composition within specimen	Elemental mapping of phase, etc.
	Organic compound mapping	Label images, map as with EDX	Verify results of FT-IR	Stereo possibility, and mosaicing from pseudo-color images	Cross-section imaging of organic compounds within specimen	Elemental mapping of phase, etc.
	Cross-section imaging 3D from slices	Cross-section imaging 3D from slices	Elemental mapping of cross-section, 3D from slices	Organic compound mapping of cross-section, 3D from slices	Mosaic, Stereo, 3D from slices	Cross-section imaging, 3D from slices
	Automated mapping of surface phase	Mapping of phases onto BSE	Elemental mapping of phases, etc.	Organic compound mapping aligned with phase, etc.	Cross-section imaging	Mosaic Stereo

**Figure 7.1:** Chart of possible sensor fusion combinations using the LCSEM at ORNL. (Van der Weerd, Brammer, Boon, & Heeren 2002; Krueger, 1999; Klimek & Pietrzyk, 2004; HKL technology, 2005).

# LIST OF REFERENCES

1. [Faint, illegible text]

2. [Faint, illegible text]

3. [Faint, illegible text]

4. [Faint, illegible text]

5. [Faint, illegible text]

6. [Faint, illegible text]

7. [Faint, illegible text]

8. [Faint, illegible text]

9. [Faint, illegible text]

10. [Faint, illegible text]

Figure 7.4. [Faint, illegible text]

- Asylum. (2004). Asylum Research. Retrieved on November 17th from <http://www.asylumresearch.com/>.
- Bonnet, N. (2004, December). Some trends in microscope image processing. *Micron*, Vol. 35, Iss. 8, pp. 635-653.
- Butters N., Leendertz J.A. (1971). A Double Exposure Technique for Speckle Pattern Interferometry. *J. Phys. E: Sci. Instrum.*, No. 4, p. 277-279.
- Carazo J.M. (1992). The fidelity of 3D reconstructions from incomplete data and the use of restoration methods. *Electron Tomography*, Editor J. Frank, New York: Plenum Press, p. 117.
- Castle, J.E., Zhdan, P.A., Singjai, P. (1998, December). Enhanced morphological reconstruction of SPM images. *J. Phys. D: Appl. Phys.*, Vol. 31, p 3437-3445.
- Chen, Z., Chengke, W., Tat Tsui, H. (2003). A new image rectification algorithm. *Pattern Recognition Letters*, Vol. 24, pp. 251-260.
- Chicon, R., M. Ortuno, and J. Abellan. (1987). An algorithm for surface reconstruction in scanning tunneling microscopy. *Surf. Sci.*, Vol. 181, p 107-111.
- Crowther R.A., DeRosier D.J., Klug A. (1970). The Reconstruction of a Three-Dimensional Structure from Projections and its Application to Electron Microscopy. *Proceedings of the Royal Society of London, Series A, Mathematical and Physical Sciences*, Vol. 317, n.1530, p319-340.
- Dongmo S., Troyon M., Vautrot P., Delain E., Bonnet N. (1996, March). Blind restoration method of scanning tunneling and atomic force microscopy images. *J. Vac. Sci. Technology*, Vol. 14, p1552-1556.
- El Ghazali, M. (1984). System Calibration of Scanning Electron Microscopes. *International Archives of Photogrammetry and Remote Sensing*, Rio de Janeiro Vol. 25, pp. 258-266.
- El Rifai O.M., Aumond B.D., & Youcef-Toumi K. (2003, January). Imaging at the Nano-scale: State of the Art and Advanced Techniques. *Proceedings 2003 IEEE/ASME International Conference on Advanced Intelligent Mechatronics*, pt. 2, vol. 2, p 715-722.
- Fomitchov P.A., Krishnaswamy S. (1997). A Compact Dual-purpose Shearography and Electronic Speckle-Pattern Interferometry. *Meas. Sci. Technology*, No. 8, pp. 581-583, 1997.

- Frankot R.T., Hensley S., Shafer S. (1994). Noise resistant estimation techniques for SAR image registration and stereo matching. *Proc. Int. Geosc. Remote Sensing Symposium*, Vol. 2, pp.1151-1153.
- Gainutdinov, R.V., Arutyunov, P.A. (2001, July-August). Artifacts in Atomic Force Microscopy. *Russian Microelectronics*, 30, p 219-224.
- Gleichmann A., Koehler J., Hemmleb M., Albertz J. (1994, April). Photogrammetric Determination of Topography of Microstructures by Scanning Electron Microscope. *Proc. SPIE*, Vol. 2184, pp. 254-263.
- Groen, E., Young, L.T., Ligthart, G. (1985). A comparison of different focus functions for use in autofocus algorithms. *Cytometry*, Vol. 12, pp 81-91.
- Hein L.R., Silva F., Nazar A.M.M., Ammann J.J. (1999). Three-Dimensional Reconstruction of Fracture Surfaces: Area Matching Algorithms for Automatic Parallax Measurements. *Scanning*, Vol. 21, No. 4, pp. 253-263.
- Hemmleb M., Schubert M. (1997, May). Digital Microphotogrammetry— Determination of the Topography of Microstructures by Scanning Electron Microscope. *Second Turkish- German Joint Geodetic Days*, Berlin, Germany, May, pp. 745–752.
- Hill M., O'Mahony C., Berney H., Hughes P. J., Hynes E., Lane W. A. (2001, August). Verification of 2-D MEMS model using optical profiling Techniques. *Optics and Lasers in Engineering*, Vol. 36, Iss. 2, pp. 169-183.
- HKL technology. (2005). *A look to the future: investigating the potential of the EBSD technique with combined focused ion beam (FIB)*. Retrieved November 17, 2005 from <http://www.hkltechnology.com/data/0-FIB+EBSD.pdf>
- Jianwei M., Ishikawa T., Johnson B., Anderson E.H., Lai B., Hodgson K.O. (2002, August). High Resolution 3D X-ray Diffraction Microscopy. *Physical Review Letters*.
- Jutamulia, S., Asakura, T., Bahuguna, R.D., De Guzman, P.C. (1994). Autofocusing based on Power-spectra analysis. *Appl. Opt.*, Vol. 33, pp. 6210-6220.
- Kak A.C., Slaney M. (1988). *Principles of Computerized Tomography Imaging*. New York: IEEE.
- Keller, D.J., Franke, F.S. (1993.). Envelope reconstruction of probe microscopy Image. *Surface Science*, Vol. 294, p 409-419.
- Kempen, G.M.P. van, Voort, H.T.M. van der, & Vliet, L.J. van (1996, June). A



- Quantative Comparison of Two Restoration Methods as Applied to Confocal Microscopy. *ASCI, Proc 2<sup>nd</sup> Annual Conference of the Advanced School for Computing and Imaging*, Belgium, pp.196-201.
- Klimek, L., Pietrzyk, B. (2004). Electron backscatter diffraction as a useful method for alloys microstructure characterization. *Journal of Alloy sand Compounds*, Vol. 382, Iss. 1-2, pp. 17-23.
- Kristan, M., Pernus, F. (2004, September). Entropy Based Measure of Camera Focus. *Proceedings Of the thirteenth Eletrotechnical and Computer Science Conference ERK*, pp. 179-182.
- Krotkov, E. (1987). Focusing. *International Journal of Computer Vision*, Vol. 1, pp 223-237.
- Krueger, R. (1999). Dual-column (FIB-SEM) wafer applications. *Micron*. Vol. 30, pp. 221-226.
- Lacey A.J., Thacker N.A., Crossley S., Yates R.B. (1998, April). A multi-stage approach to the dense estimation of disparity from stereo SEM images. *Image and Vision Computing*, Vol. 16, Iss. 5, pp. 373-383.
- Lanzavecchia S., Bellon P.L., Radermacher M. (1999). Fast and Accurate Three-Dimensional Reconstruction from Projections with Random Orientations via Radon Transforms. *Journal of Structural biology*, Vol. 128, pp.152-164.
- Lodi V.A., Merlo S., Norgia M., Spinola G., Vigna B., Zerbini S. (2002, May). Characterization of MEMS by Feedback Interferometry. *Proc. Design, Test, Integration and Packaging of MEMS/MOEMS, Cannes, SPIE*, Vol. 4755, pp. 420-429.
- Lopez-Cepero, J.M., de Arellano-Lopez, A.R., Quispe-Cancapa, J.J. & Martinez-Fernandez, J. (2005, September). Confocal Microscopy for Fractographical Surface Characterization of Ceramics. *Microscopy and Analysis*, Vol. 19, pp. 9-11.
- O'Mahnoy C., Hill M., Brunet M., Duane R., Mathewson A. (2003). Characterization of Micromechnical Structures Using White-light Interferometry. *Meas. Si. Technology*, No. 14, pp. 1807-1814.
- Marabini R., Herman G. T., Carazo J. M. (1998, April). 3D reconstruction in electron microscopy using ART with smooth spherically symmetric volume elements (blobs). *Ultramicroscopy*, Vol. 72, Iss. 1-2, pp. 53-65
- Marabini R., Rietzel E., Schroeder R., Herman G. T., Carazo J. M. (1997, December).

Three-Dimensional Reconstruction from Reduced Sets of Very Noisy Images Acquired Following a Single-Axis Tilt Schema: Application of a New Three-Dimensional Reconstruction Algorithm and Objective Comparison with Weighted Backprojection. *Journal of Structural Biology*, Vol. 120, Iss. 3, pp 363-371.

McNally J.G., Karpova T., Cooper J., Conchello J.A. (1999). Three-Dimensional Imaging by Deconvolution Microscopy. *Methods*, Vol. 19, pp. 373-385.

MikroMasch (2005). *TGZ series for vertical SPM calibration*. Retrieved November 17, 2005 from <http://www.spmtips.com/tgz/>

Midgley P.A., Weyland M. (2003, September). 3D Electron Microscopy in the Physical Sciences: The Development of Z-contrast and EFTEM Tomography. *Ultramicroscopy*, Vol. 96, nn. 3-4, pp. 413-431.

Minoshima K., Suezaki T., Komai K. (2002). Genetic Algorithms for High-Precision Reconstructions of Three-Dimensional Topographys Using Stereo Fractographs. *Fatigue and Fracture of Engineering Materials and Structures*, Vol. 23, No. 5, pp. 435-443.

Morgan, M., Kim, K., Jeong, S., Habib, A. (2004, July). Indirect Epipolar Resampling of Scenes Using Parallel Projection Modeling of Linear Array Scanners. *XX<sup>th</sup> Congress of ISPRS*.

Nayar, S.K., Nakagawa, Y. (1994, August). Shape from Focus. *IEEE Transactions on Pattern Analysis and Machine Intelligence*. Vol. 16, No. 8, pp. 824-831.

Niederost M., Niederost J., Scucky J. (2002). Automatic 3D Reconstruction and Visualization of Microscopic Objects from a Monoscopic Multifocus Image Sequence. *International Archives of Photogrammetry, Remote Sensing and Spatial Information Sciences*, Vol. XXXIV-5/W/10. International Workshop on Visualization and Animation of Reality based 3D Models.

Pech-Pacheco, J.L., Cristobal, G., Chamorro-Martinez, J., Fdez-Valdivia, J. (2000). Diatom Autofocusing in brightfield microscopy: a comparative study. *International Conference Pattern Recognition*. Barcelona.

Petitgrand S., Yahiaoui R., Danaie K., Bosseboeuf A., Giles J.P. (2001). 3D Measurement of Micromechanical Devices Vibration Mode Shapes with a Stroboscopic Interferometric Microscope. *Optics and Lasers in Engineering*, No. 36, pp. 77-101.

Piazzesi G. (1973). Photogrammetry with the Scanning Electron Microscope. *J. Phys. E. Sci. Instrum*, Vol. 6, pp. 392-96.

- Pudney C.J., Kovesi P.D., Stretch, D. (1994, September). Surface Detection Using Local Energy for 3D Confocal Microscope Images. *Image Analysis*, p. 68-73.
- Radermacher M. (1992). Weighted backprojection methods. *Electron Tomography*, J. Frank, Editor, New York: Plenum Press, pp. 91–116.
- Radon, J. (1917). Über die bestimmung von funktionen durch ihre integralwerte längs gewisser mannigfaltigkeiten. *Math-Phys. Kl*, Vol. 69, pp 262-267.
- Raspanti, M., Binaghi, E., Gallo, I., & Manelli, A. (2005). A Vision-Based, 3D Reconstruction Technique for Scanning Electron Microscopy: Direct Comparison With Atomic Force Microscopy. *Microscopy Research and Technique*, Vol. 67, pp. 1-7.
- Richards, R.G., Wieland, M., & Textor, M. (2000, August). Advantages of stereo imaging of metallic surfaces with low voltage backscattered electrons in a field emission scanning electron microscope. *Journal of Microscopy*, Vol. 199, 115-123.
- Roderdink J.B. (1994, May). FFT-based Methods for Nonlinear Image Restoration in Confocal Microscopy. *Journal of Mathematical Imaging and Vision*, Vol. 4, pp. 199-207.
- Santos A., Ortiz de Solorzano, C., Vaquero, J.J., Pena, J.M., Malpica, N., & Del Pozo, F. (1997, June). Evaluation of autofocus functions in molecular cytogenetic analysis. *Journal of Microscopy*, Vol. 88, Pt. 3, pp 264-272.
- Seeger, A. (2004). *Surface Reconstruction From AFM and SEM Images*. Dissertation at the University of North Carolina, Chapel Hill, North Carolina.
- Shaw P.J. (1995). Handbook of Biological Confocal Microscopy. Ed. J. B. Pawley, New York: Plenum Press, pp. 373-387.
- Schroer C.G., Meyer J., Kuhlmann M., Benner B., Gunzler T.F., Lengeler B., Rau C., Weitkamp T., Snigirev A., Snigireva I. (2003, March). Nano-Tomography Based on Hard X-Ray Microscopy with Refractive Lenses. *Journal De Physique IV*, Vol. 104, p. 271.
- Schultz, M. (2004). *Multiple View 3D Reconstruction of Micro- to Nano-scopic Specimens*. Master's thesis at the University of Tennessee, Knoxville, TN.
- Skoglund U., Ofverstedt L. (1996, November-December). Maximum-entropy three-dimensional reconstruction with deconvolution of the contrast transfer function: a test

- application with adenovirus. *J Struct Biol.*, Vol. 117, n. 3, pp. 173-88.
- Stampfl J., Scherer S., Gruber M., Kolednik O. (1996, September). Reconstruction of Surface Topographies by Scanning Electron Microscopy for Applications in Fracture Research. *Applied Physics A: Materials Science & Processing*, Vol. 63, pp. 341-46.
- Stefanou S.S., Hansen E. W. (1994). Maximum-likelihood reconstruction of 3D Confocal Data Sets. *Proceedings SPIE*, Vol. 2184, pp.182-187.
- Velazquez Muriel, J.A., Sorzano, C.O.S. & Carazo, J.M. (2001). Method development of combination of atomic force and electron microscopy to obtain better 3D reconstructions. *Proceedings of the Spanish, Portuguese, and French Microscopy Societies meeting at Barcelona*.
- Villarrubia, J. S. (1994, December). Morphological estimation of tip geometry for scanned probe microscopy. *Surface Science*, vol. 321, n. 3, p. 287-300.
- Villarrubia, J.S. (1997). Algorithms for Scanned Probe Microscope Image Simulation, Surface Reconstruction, and Tip Estimation. *Journal of Research of the National Institute of Standards and Technology*, 102, p 425.
- Wang S.H., Reading I. (2003). Study of Surface Deformation of MEMS Components using the FFT and Phase-Shifting. *SimTech Technical Report*, <http://www.simtech.a-star.edu.sg/research/tech-report2003.html>, 2003.
- Weerd, J. van der, Brammer, H., Boon, J.J., & Heeren, R.M.A. (2002). Fourier Transform Infrared Microscopic Imaging of an Embedded Paint Cross-Section. *Applied Spectroscopy*, Vol. 56, no. 3, pp. 275-283.
- Widjaja, J. (2000). Wavelet Transform for Autofocusing Detection Systems. *ScienceAsia*, Vol. 26, pp. 111-114.
- Williams, P.M, Shakesheff, K.M., Davies, M.C., Jackson, D.E., Roberts, C.J., Tendler, S.J.B. (1996). Blind reconstruction of scanning probe image data. *J. Vac. Sci. Technology B14*, p 1557.
- Wolfling S., Banitt D., Ben-Yosef N., Arieli Y. (2004). Innovative Metrology Method for the 3-Dimensional Measurements of MEMS. *Proceedings of SPIE The International Society for Optical Engineering*, Vol. 5343, pp. 255-263.
- Wyant, J. (2002, April). White Light Interferometry. *AeroSense*, Orlando, Florida.
- Yatchmenoff B., Compton R. (1990). Ceramic Surface Analysis Using Optical Sections. *Ceramic Bulletin*, Vol. 69, No. 8.

## VITA

Christopher Robert Kammerud was born in Nashville, TN, on February 9<sup>th</sup>, 1981. He was raised in Mt. Juliet, and graduated from Mt. Juliet High School in 1999. From here, he took part in a sort of family tradition and attended the University of Tennessee, Knoxville, where he received his B.S. in computer engineering in 2003. Dr. Abidi offered him a chance to pursue a Master's degree at the IRIS Lab and this thesis is the result of that work.

Chris is currently pursuing a job in the field of image processing, with an emphasis on microscopic imaging.

Zamofing T., Hugli H. (2004). Applied multifocus 3D microscopy. *Proceedings of SPIE The International Society for Optical Engineering*. Vol. 5265, pp. 134-144.